ON-CHIP SUPERCONDUCTING LC MATCHING NETWORKS AND

COPLANAR WAVEGUIDES FOR RADIO-FREQUENCY SINGLE ELECTRON

TRANSISTORS

A Thesis

Submitted to the Faculty

in partial fulfillment of the requirements for the

degree of

Doctor of Philosophy

by

WEIWEI XUE

in

Physics

Dartmouth College

Hanover, New Hampshire

SEPTEMBER 2010

Examining Committee:

Chairman _____
Alexander J.Rimberg

Member _____
Miles P.Blencowe

Member _____
Lorenza Viola

Member _____
Britton Plourde

_____
Brian W. Pogue
Dean of Graduate Studies

ABSTRACT

The radio-frequency single-electron transistor (RF-SET) [1–3] has attracted significant interest as one of the fastest charge detectors known today. In this thesis, we show that by designing an on-chip superconducting LC matching network for the RF-SET, we can minimize unwanted dissipation and optimize impedance matching. Using such a network, we fabricated one of world's fastest RF-SETs and measured the quantum noise of an S-SET near the quantum limit [4].

In the later part, we develop a design consisting of an SET embedded in a circuit quantum electrodynamics (QED) architecture, where the SET is coupled to a coplanar waveguide (CPW) resonator. The resonator is carefully designed to allow introduction of a DC voltage or current bias to the microwave cavity without significantly disturbing the cavity modes or degrading the quality factor [5]. Our proposed experiments will be focused on the zero bias region of the SET where it is strongly nonlinear.

PREFACE OR ACKNOWLEDGMENTS

This Ph.D. could not have been completed without support of innumerable colleagues, professors, and friends. I can not, in this space, give them each the thanks that they deserve, but nevertheless, I will try.

To Mom and Dad: I could not expect better parents in the world. I treasure all the love and support we share. Thank you so much for the long-distance love and support over the past six years I have been away in the U.S.

I will give my special thanks to Alex for being a fantastic mentor, teacher, advisor, colleague, and friend over these past six years. From my first day in the group, Alex guided me towards the world of mesoscopic physics and helped me out with experimental and theoretical challenges. I would also like to extend my gratitude to the members of my committee. Many thanks to Prof. Blencowe for your theoretical guide. Thanks to Prof. Viola for showing great interest in my work. Thanks to Prof. Lawrence for your insightful questions and support.

Thanks to everyone from the Rimberg Lab. Many thanks to Zhongqing Ji, Feng Pan, Madhu Thalakulam, Joel Stettenheim, Tim Gilheart. They taught me to make the first sample and carry out the measurements. It is my great pleasure to work with them for these years. Thanks to Fei Chen for helping me with the sample fabrication. Thanks to Mustafa Bal for showing me various lab techniques.

I would also like to thank Dr.Charles P. Daghlian, who is the supervisor in the Micro-electronic Lab at Dartmouth College. He was always very helpful with any technical problems I had with the SEM and AFM.

TABLE OF CONTENTS

LIST OF FIGURES

CHAPTER 1

INTRODUCTION

1.1 Motivation

The SET is widely regarded as the ultimate read-out device for a quantum computer. Analogous to the way a classical computer is built from an electric circuit with wires and logic gates, a quantum computer is built from a quantum circuit containing wires and elementary quantum gates to carry and manipulate the quantum information. Unlike classical computers which use bits to store information either as a "0" or a "1", quantum computers use quantum bits (qubits) [6] as the basic memory unit to store quantum information. An example of an implementation of qubits for a quantum computer begins with the particles with two spin states: "down" and "up" or $|0\rangle$ and $|1\rangle$. A qubit can be in a superposition state of $|0\rangle$ and $|1\rangle$, for example, $|\phi\rangle = \alpha|0\rangle + \beta|1\rangle$, where α and β are complex numbers. A general n qubits system then have 2^n superposition states. For example, if $n = 50$, the number required to describe all the states exceeds the capacity of the largest conventional computer. Thus, a quantum computer can naturally perform operations in parallel, using only a single processing unit.

The main idea of a quantum measurement is to build an interface between the microscopic quantum system and the macroscopic world with a mesoscopic amplifier such as an SET. Unlike a classical measurement, a quantum measurement destroys the quantum states of the measured system due to the backaction of the detector. For a system such as an SET coupled to a quantum dot (QD), the backaction introduced from the charge fluctuations on SET's island will dephase the spin states of the QD. Besides the minimal backaction, a "good" quantum measurement also requires an ultra-sensitive SET, for the purpose of fast extraction of quantum information which will also dephase intrinsically. For the fixed noise floor set by a secondary amplifier such as a High Electron Mobility Transistors (HEMT), an SET with a better charge sensitivity allows a shorter measurement time. Better charge

sensitivity provides a larger signal to noise ratio (SNR) for a more reliable quantum measurement. However, the improved sensitivity of SET requires increased backaction that itself contribute noise. The result is a strict limit on added amplifier noise [7–12]. To approach this limit, a quantum-limited amplifier must posses an ideal balance between sensitivity and backaction [13]. Although the best charge sensitivity is found for above-gap operation of the superconducting SET (S-SET), the backaction is also largest there. Instead, we bias the S-SET near a double Cooper-pair resonance. In this thesis, we describe on-chip superconducting LC matching network that significantly improve S-SET performance. We also report the first complete and quantitative measurements of the quantum noise of a S-SET near a double Cooper-pair resonance. A simultaneous measurement of our S-SET's charge sensitivity indicates that it operates within a factor of 3.6 of the quantum limit. Operating at radio frequencies, a quantum limited S-SET has many potential applications in the measurements of spin- and charge-based quantum system. For instance, coherent oscillations between the two states of a quantum two-state system represent one of the most fundamental manifestations of quantum mechanics and are encountered in almost all area of physics. Given its ideal balance of charge sensitivity and back-action, a quantum-limited S-SET could make an excellent choice for weak continuous measurement of coherent oscillations. Quantum oscillations of an electron between the QDs would create an oscillating component of the current I through the S-SET. The phase of the oscillation diffuses under the backaction due to the shot noise of S-SET and this backaction imposes the fundamental limit on the measurement's SNR. In addition, the ultra fast S-SET can be used as a sensor for real-time electron counting experiments by operating it in the vicinity of the quantum limit.

The second part of the thesis will discuss a high-Q on-chip microwave cavity with a DC current or voltage bias used to drive an embedded S-SET. We develop a technique for doing so that does not disturb the cavity modes or degrade the Q at high frequencies. One goal for this design is to study the laser-like effects with the S-SET in the supercurrent regime.

A very brief overview of the structure of this thesis is as follows:

In chapter 2, we will discuss the theory background of SET and its variant the radio frequency SET (RF-SET). For an SET in the normal state, the so-called orthodox model

will be introduced. For an S-SET we will discuss the double Josephson quasiparticle (DJQP) and Josephson quasiparticle (JQP) tunneling process and the Josephson effect. A very brief introduction of RF-SET will also be included in this chapter.

In chapter 3, we will begin with S-matrix analysis of a lossy matching network. Design and simulation of an on-chip superconducting LC resonator is then introduced. A comparison between lossy and lossless matching networks is illustrated. Theory of the quantum noise measurement of RF-SET is introduced, assuming use of a superconducting resonator.

In chapter 4, we will discuss the design and mechanism of embedding the S-SET in a high-Q on-chip microwave cavity. We propose a novel technique to apply a DC current or voltage bias to SET without significantly disturbing the cavity modes or degrading the Q at very high frequencies.

In chapter 5, we will briefly review technical details such as fabrication techniques, fridge setup, sample wiring, CPW sample box design and RF-SET measurement techniques.

In chapter 6, we will present experimental results including RF-SSET characterization, on-chip matching network calibration, intrinsic quantum noise measurement and CPW characterization.

In chapter 7, we will discuss possible future work based on our current LC network and circuit QED design.

CHAPTER 2

THEORY OF THE SET

In this chapter, the theoretical background of the SET and its variant the RF-SET are discussed. For the normal state SET, the orthodox model is explained; for the S-SET, the Josephson effect is included. The RF-SET is introduced briefly at the end.

2.1 Introduction to the SET

The SET was invented by Fulton and Dolan in the 1980's [14]. It consists of a nanoscale island contacted through two ultra small tunnel junctions to two leads. The leads are
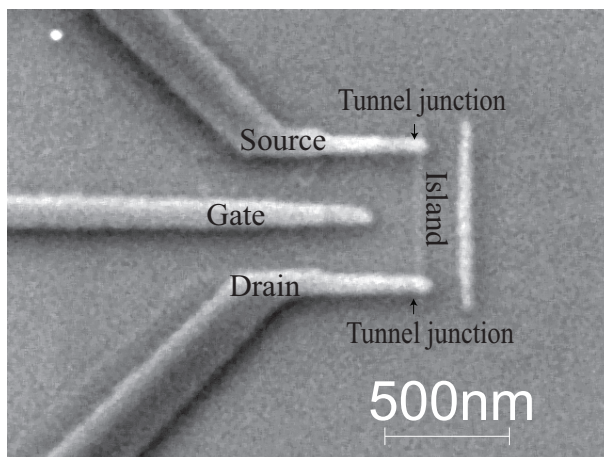
Figure 2.1. Scanning electron micrograph of the SET.

generally called the source and drain. Usually, we have a gate electrode capacitively coupled to the island. Experimentally, tunnel junctions of an SET are made by two ultra-thin aluminum films sandwiched with an aluminum oxide layer. Fig. 2.1 shows a scanning electron micrograph of a typical SET. A voltage between the source and drain will drive tunneling events and change the number of electrons on the island, which will cause a measurable current through the SET.

2.2 Coulomb blockade of the SET in the normal state

Mesoscopically, the charge tunneling through an ultra small junction in the normal state is discrete in units of the electronic charge e. In Coulomb blockade regions [15], the electrostatic energy increases with the addition of a single electron creating an energy barrier forbidding the addition of further charges to the island. The energy is parameterized by the charging energy, $E_C = e^2/2C_\Sigma$, where C_Σ is the total capacitance of the SET island to all the source-drain leads and gates. When E_C is larger than the electrical energy generated by the source drain bias of SET, the sequential tunneling will be blocked.

Two conditions must be satisfied for such Coulomb blockade behavior. First, the island must be small enough and the temperature low enough that E_C is large compared to the ambient thermal energy $k_B T$, $E_C \gg k_B T$. Second, in order to localize the wave function of an excess electron on the island, we will assume the average tunneling time $t = \frac{e}{I} = \frac{eR_T}{V_{\rm sd}}$ is much larger than the uncertainty time $\tau = \frac{h}{\delta E}$ determined by Heisenberg energy-time relation, where $V_{\rm sd}$ is the source drain bias through the SET, R_T is the total resistance of SET and $\delta E = eV_{\rm sd}$ is the change of electrostatic energy due to a single-electron tunneling. This condition gives

$$R_T \gg h/e^2 = R_K \approx 25.8 {\rm k\Omega} \tag{2.1}$$

where R_K is defined as the resistance quantum.
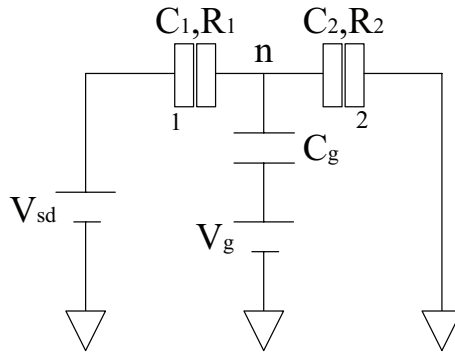
Figure 2.2. Circuit diagram of an asymmetrically biased SET. Here, n is the electron number on the center island.

Now we can estimate the energy required for the electron to tunnel through an SET. Fig. 2.2 shows a schematic diagram for an asymmetrically biased SET. The charges on the

capacitors satisfy the following relationships:

$$Q_1 = C_1 V_1, \tag{2.2}$$

$$Q_2 = C_2 V_2, \tag{2.3}$$

$$Q_g = C_g(V_g - V_2), \tag{2.4}$$

and

$$Q_i = Q_2 - Q_1 - Q_g = -ne \tag{2.5}$$

where Q_1, Q_2, Q_g, Q_i are the total charges on junction 1, junction 2, the gate and the center island. We also have $V_{\mathrm{sd}} = V_1 + V_2$. Solving for V_1 and V_2 yields

$$V_1 = (C_g V_{\mathrm{sd}} + C_2 V_{\mathrm{sd}} - C_g V_g + ne)/C_\Sigma \tag{2.6}$$

and

$$V_2 = (C_1 V_{\mathrm{sd}} + C_g V_g - ne)/C_\Sigma \tag{2.7}$$

where $C_\Sigma = C_1 + C_2 + C_g$. The electrostatic energy stored in all the capacitors is given by

$$E_T = \frac{Q_1^2}{2C_1} + \frac{Q_2^2}{2C_2} + \frac{Q_g^2}{2C_g} \tag{2.8}$$

The work when an electron tunnels through either junction includes a contribution from both source-drain voltage and gate voltage. From Eq. 2.6 and Eq. 2.7 we can find the total work required for $n_{1(2)}$ electrons to pass through junction 1(2). It is given by

$$W(n_1) = -n_1 e\left[\frac{C_2}{C_\Sigma} V_{\mathrm{sd}} + \frac{C_g}{C_\Sigma}(V_{\mathrm{sd}} - V_g)\right] \tag{2.9}$$

and

$$W(n_2) = -n_2 e\left(\frac{C_1}{C_\Sigma} V_{\mathrm{sd}} + \frac{C_g}{C_\Sigma} V_g\right). \tag{2.10}$$

The energy for a charge state with n_1 and n_2 electrons on junction 1 and 2 is

$$E(n_1, n_2) = E_T - W(n_1) - W(n_2) \tag{2.11}$$

For an electron to tunnel through junction 1, the change in energy of the system is given by

$$\Delta E_1^\pm = E(n_1, n_2) - E(n_1 \pm 1, n_2) = \frac{e}{C_\Sigma}[-e/2 \mp (en + C_g V_{\text{sd}} + C_2 V_{\text{sd}} - C_g V_g)] \quad (2.12)$$

Similarly, for junction 2, we have

$$\Delta E_2^\pm = E(n_1, n_2) - E(n_1, n_2 \pm 1) = \frac{e}{C_\Sigma}[-e/2 \pm (en - C_1 V_{\text{sd}} - C_g V_g)] \quad (2.13)$$
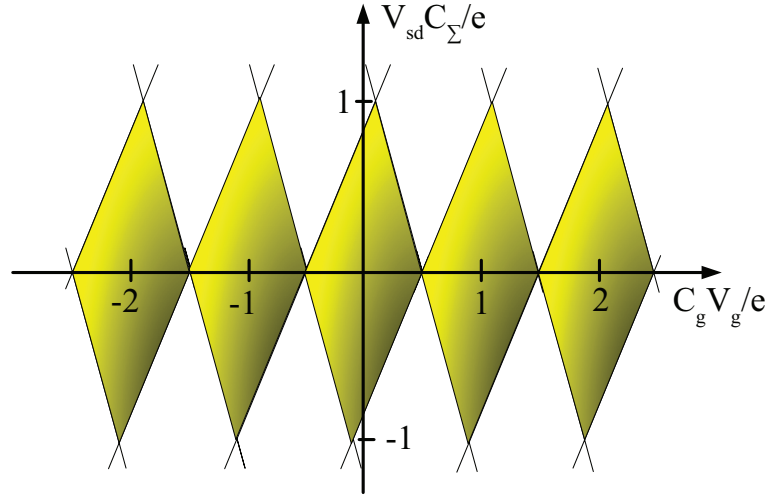
Figure 2.3. Stability diagram of a normal SET. No current flows in the diamond-shaped region where the SET island has a fixed number of electrons.

As $T \to 0$, the condition for electron tunneling is $\Delta E_{1,2}^\pm > 0$, which is

$$-e/2 \mp (en + C_g V_{\text{sd}} + C_2 V_{\text{sd}} - C_g V_g) > 0 \quad (2.14)$$

and

$$-e/2 \pm (en - C_1 V_{\text{sd}} - C_g V_g) > 0. \quad (2.15)$$

Eq. 2.14 and Eq. 2.15 generate a stability diagram shown in Fig. 2.3 for different n. The diamond shaped areas correspond to the Coulomb blockade. In these regions, the

number of electrons on the island is well defined. Between these diamonds, a current can flow. For a given V_{sd}, the size of the Coulomb blockade is determined by the vertical size of the shaded region; the maximum blockade width is e/C_Σ. In addition, the SET current varies periodically with V_g, showing so-called Coulomb oscillations. As $C_g V_g$ approaches half-integer values of e, the Coulomb blockade disappears and tunneling occurs. Thus, the current versus V_g will exhibit a sharp peak for a narrow range of gate bias around half-integer values of e. The separation in voltage between these peaks is given by e/C_g.

2.3   Orthodox theory for the SET

The total tunneling rates across a junction will be calculated using the "orthodox theory" [16], which has been widely used to calculate the $I - V_{\mathrm{sd}}$ characteristics of tunnel junctions at finite temperature and predict the back-action of the single electron transistor onto a single electron box. Several assumptions are required for the validity of the model: 1 dimension, junction size and the effect of the electromagnetic environment are negligible; 2 tunneling occurs only through sequential tunneling events, i.e., co-tunneling and multiple tunneling events are ignored; [17] 3 the tunneling is an uncorrelated stochastic process and the tunneling rates depends only on the energy difference between the initial and final states; 4 the electron number is well defined, which requires $R_T \gg R_K$; and 5 the frequency dependence of transition rates in the high frequency regime is ignored.

The rate for an electron to tunnel across a junction is derived from Fermi's golden rule. The transition rate from state i to f is given by

$$\Gamma_{i \to f} = \frac{2\pi}{\hbar} \sum_f |T_{if}|^2 \delta(\epsilon_f - \epsilon_i) \tag{2.16}$$

where $|T_{if}|$ is the transition matrix element, ϵ_i and ϵ_f are the energies of the electrons in the initial and final states. To obtain the total tunneling rate across the junction, we assume the density of the states is constant for a specific energy and integrate over all energies. The probability of a filled state on the left side of the junction is derived from the Fermi function,

$$f(\epsilon) = \frac{1}{1 + \exp(-\epsilon/k_B T)} \tag{2.17}$$

The probability of an empty state on the right hand side of the junction is $1 - f(\epsilon)$, the total tunneling rate across the junction is then given by

$$\Gamma_{L \to R} = \frac{1}{e^2 R_t} \int_{-\infty}^{+\infty} f(\epsilon)[1 - f(\epsilon')] d\epsilon d\epsilon' \tag{2.18}$$

where R_t is the resistance of the tunnel junction. Analytically integrating the function yields

$$\Gamma_{L \to R} = \frac{1}{e^2 R_t} \frac{\Delta E}{1 - \exp(-\Delta E/k_B T)} \tag{2.19}$$

where ΔE is the total energy difference between the initial and final states. Based on the SET circuit diagram shown in Fig 2.2, we can derive the tunneling current of SET. We define $\Gamma_{L(R) \to R(L)}^{1(2)}(n)$ as the tunneling rate from left (right) to right (left) of junction 1(2) with total number of n electrons on the island. Assuming sequential tunneling through SET, only two most probable electron numbers on the island n, and $n + 1$ need to be considered. Four different tunneling rates are then involved: $\Gamma_{L \to R}^1(n)$, $\Gamma_{L \to R}^2(n+1)$, $\Gamma_{R \to L}^1(n+1)$, and $\Gamma_{R \to L}^2(n)$. Assuming we have a symmetric SET, we have:

$$\Gamma_{L \to R}^1(n) = \frac{1}{e^2 R_t} \frac{\Delta E_1^-}{1 - \exp[-\Delta E_1^-/k_B T]}, \tag{2.20}$$

$$\Gamma_{L \to R}^2(n+1) = \frac{1}{e^2 R_t} \frac{\Delta E_2^+}{1 - \exp[-\Delta E_2^+/k_B T]}, \tag{2.21}$$

$$\Gamma_{R \to L}^1(n+1) = \frac{1}{e^2 R_t} \frac{\Delta E_1^+}{1 - \exp[-\Delta E_1^+/k_B T]}, \tag{2.22}$$

and

$$\Gamma_{R \to L}^2(n) = \frac{1}{e^2 R_t} \frac{\Delta E_2^-}{1 - \exp[-\Delta E_2^-/k_B T]}. \tag{2.23}$$

The tunneling current is approximately given by [18,19]

$$I = e[\Gamma_{L \to R}^1(n)P(n) - \Gamma_{R \to L}^1(n+1)P(n+1)] \tag{2.24}$$

$$= e[\Gamma_{L \to R}^2(n+1)P(n+1) - \Gamma_{R \to L}^2(n)P(n)] \tag{2.25}$$

9
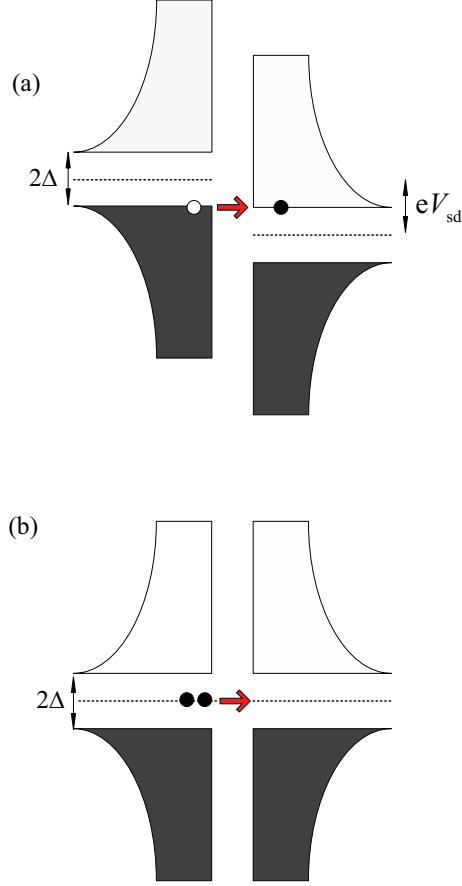
Figure 2.4. Two tunneling process through an SIS junction: (a) dissipative quasi-particle tunneling, (b) coherent Cooper-pair tunneling.

where $P(n)$ and $P(n+1)$ are the probabilities of the island having n or $n+1$ electrons. They are given by

$$P(n) = 1 - P(n+1) = \frac{\Gamma^2_{L\to R}(n+1) + \Gamma^1_{R\to L}(n+1)}{\Gamma^2_{L\to R}(n+1) + \Gamma^1_{R\to L}(n+1) + \Gamma^1_{L\to R}(n) + \Gamma^2_{R\to L}(n)} \qquad (2.26)$$

2.4 Superconducting single electron transistors (S-SET)

One main variant of the SET is its superconducting counterpart. For $Al/AlO_x/Al$ junctions, the aluminum layer becomes superconducting for ambient temperature below $T_c = 2.1K$. Such a junction then becomes a single superconducting-insulator-superconducting (SIS) junction. In a superconductor, free electrons join together to form Cooper pairs. Because of this new charge carrier, tunneling between superconductors is more complex than in the normal state. When eV_{sd} is higher than the superconducting gap 2Δ, the Cooper

pair breaks into two quasiparticles and the tunneling is then dominated by the dissipative quasiparticles. Occupied quasiparticle states in a superconductor are similar to the single electron states in a normal metal as shown in Fig. 2.4(a). If the Fermi energies of two superconducting leads are aligned, the tunneling is caused by coherent Cooper pairs, which is shown in Fig. 2.4(b).

The current through an SIS junction due to quasiparticle tunneling is derived from the current through a normal metal/insulater/metal (NIN) due to electrons [20,21]. For a single tunnel junction, the tunneling rate from left to right is given as

$$\Gamma_{L \to R} = \frac{\pi}{\hbar} |T|^2 \int_{-\infty}^{\infty} N_L(E) f(E) N_R(E + eV_{\text{sd}})[1 - f(E + eV_{\text{sd}})]dE \qquad (2.27)$$

where $|T|$ is the amplitude of the tunneling matrix element, and $N_{L(R)}(E)$ is the density of states of the left (right) electrode. A similar expression can be written for $\Gamma_{R \to L}$.

The total current through NIN junction is given by

$$I_N(V_{\text{sd}}) = e(\Gamma_{L \to R} - \Gamma_{R \to L}) = \frac{e\pi}{\hbar} |T|^2 \int_{-\infty}^{\infty} N_L(E) N_R(E + eV_{\text{sd}})[f(E) - f(E + eV_{\text{sd}})]dE \tag{2.28}$$

For an SIS junction, the occupation numbers are given by the Fermi distribution and the density of the states is given by

$$\frac{N_s(E)}{N(0)} = \frac{|E|}{\sqrt{E^2 - \Delta^2}} \qquad (2.29)$$

for $|E| > \Delta$ and 0 otherwise. The current through an SIS junction is then given by

$$I_s(V_{\text{sd}}) = \frac{1}{R_N e} \int_{-\infty}^{\infty} \frac{|E|}{\sqrt{E^2 - \Delta^2}} \frac{|E + eV_{\text{sd}}|}{\sqrt{(E + eV_{\text{sd}})^2 - \Delta^2}} [f(E) - f(E + eV_{\text{sd}})]dE \qquad (2.30)$$

where R_N is the resistance of the SIS junction.

The resistance requirement for the Coulomb blockade of quasiparticles can be derived similarly to that for the normal SET. The energy uncertainty relation is given by

$$\Delta E \Delta \tau > \hbar. \qquad (2.31)$$

11

where for ΔE we substitute E_c of the SET. $\Delta\tau$ is the time for a quasiparticle to tunnel through a junction, which is

$$\Delta\tau = \frac{1}{\Gamma} = \frac{e}{I_s} \tag{2.32}$$

where I_s is the current through the junction. For an SIS junction, quasiparticle current will only flow when $eV_{\mathrm{sd}} \geq 2\Delta$, so the current can be approximated by

$$I_s = \frac{2\Delta}{eR_N} \tag{2.33}$$

where R_N is the resistance of the SIS junction. Combining Eq. 2.31, Eq. 2.32 and Eq. 2.33 gives

$$R_N > \frac{2\hbar\Delta}{e^2 E_c} = \frac{\Delta}{\pi E_c}R_K. \tag{2.34}$$

A more precise result was derived by Averin et al [22], which is

$$\frac{\Delta}{E_c}\frac{\pi\hbar}{e^2}(\frac{1}{R_1} + \frac{1}{R_2}) < 1 \tag{2.35}$$

where R_1,R_2 are the resistances of junction 1 and 2 at normal state. For a symmetric S-SET, $R_1 = R_2 = \frac{R_T}{2}$, yielding

$$R_T > \frac{2\Delta}{E_c}R_K. \tag{2.36}$$

Comparing Eq. 2.36 with Eq. 2.1, the resistance of an S-SET must be a ratio of $\frac{2\Delta}{E_c}$ times the normal state resistance of a SET to exhibit charging effects.

Transport through an S-SET is quite complex. Depending on the ratio $\frac{V_{\mathrm{sd}}}{\Delta}$, the transport can be divided into several sub-regimes.

When $eV_{\mathrm{sd}} > 4\Delta$, the bias voltage has sufficient energy to break Cooper pairs at both junctions. In this case, transport is dominated by sequential quasiparticle tunneling, which is very similar to electron tunneling in a normal state SET. [23,24] When $eV_{\mathrm{sd}} < 4\Delta$, the major tunneling processes are well represented in the S-SET curve shown in the Fig. 2.5. At zero bias ($V_{\mathrm{sd}} \approx 0$), we have a suppercurrent feature which is due to resonant Cooper pair tunneling through both junctions. The other two dominant current features are the double Josephson-quasiparticle (DJQP) [25,26] and Josephson-quasiparticle (JQP) [27]
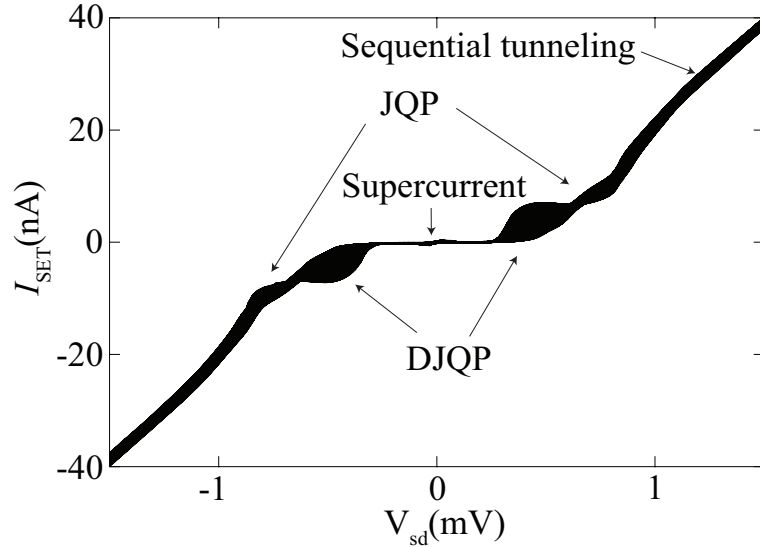
Figure 2.5. $I - V$ characteristic for a superconducting SET.

tunneling cycles. From the $I - V$ curve, the DJQP cycle is more energetically favorable than the JQP cycle since it occurs at a lower bias. The tunneling events for these two cycles are illustrated schematically in Fig. 2.6. The JQP cycle involves a Cooper pair tunneling onto the island through one SIS junction. Two quasiparticles then tunnel sequentially out through the other SIS junction. The number of electrons on the island for JQP cycle follows the pattern $|n\rangle \to |n + 2\rangle \to |n + 1\rangle \to |n\rangle$.

For quasiparticles to tunnel through one single SIS junction, the bias voltage must satisfy $eV_{\text{sd}} \geq 2\Delta$. For an S-SET with two SIS junctions, the requirement is modified for each junction by capacitance division of V_{sd}. For an asymmetrically biased S-SET, the voltage across junction 1(2) will be $\kappa_1 V_{\text{sd}}$ ($\kappa_2 V_{\text{sd}}$), where

$$\kappa_1 = \frac{C_2 + C_g}{C_\Sigma}, \tag{2.37}$$

and

$$\kappa_2 = \frac{C_1}{C_\Sigma}. \tag{2.38}$$

Meanwhile, the bias voltage must provide enough energy to overcome the change in the charging energy $E(n)$, which is

$$E(n) = \frac{(Q_0 - ne)^2}{2C_\Sigma} \tag{2.39}$$

13
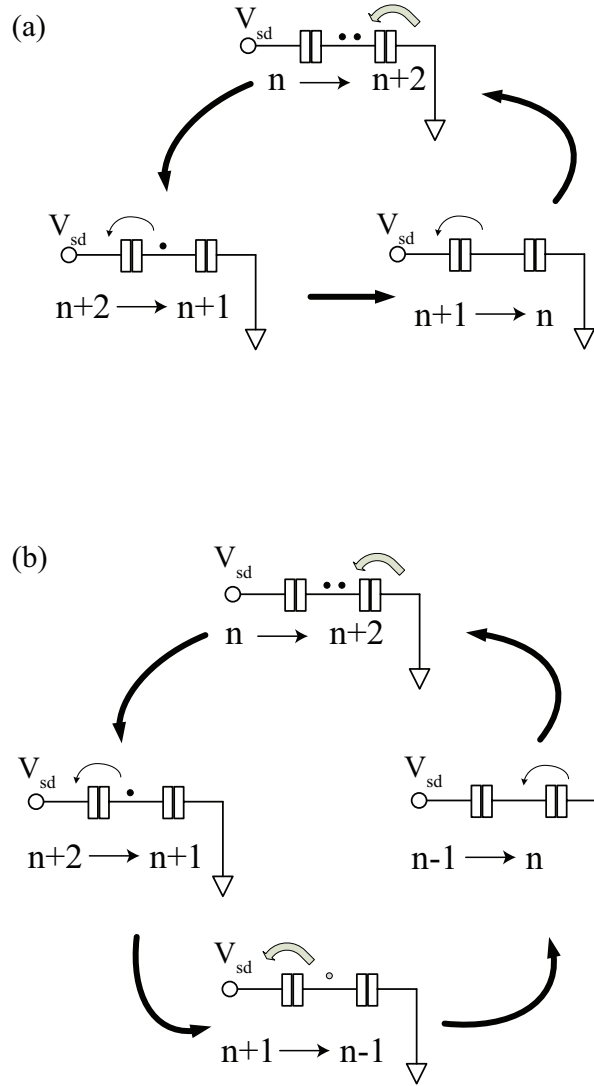
Figure 2.6. Quasiparticle tunneling cycles in the S-SET: (a) JQP cycle and (b) DJQP cycle.

where Q_0 is the offset charge and n is the number of electrons on the island.

Now the energy requirement for the JQP cycle can be given as follows: for Cooper pair tunneling in through junction 2 we have

$$2\kappa_2 eV_{\mathrm{sd}} = E(n+2) - E(n). \tag{2.40}$$

Now we have $n+2$ electrons on the island. For the first quasiparticle tunneling through junction 1, we have

$$\kappa_1 e V_{\text{sd}} \geq E(n+1) - E(n+2) + 2\Delta \tag{2.41}$$

and for the second quasiparticle through junction 1, we have

$$\kappa_1 e V_{\text{sd}} \geq E(n) - E(n+1) + 2\Delta. \tag{2.42}$$

Eq. 2.42 is a stronger constraint than Eq. 2.41, which indicates the tunneling of a second quasiparticle requires a larger V_{sd}. From the $I - V$ curve, we find at a lower bias, where the JQP cycle is energetically unfavorable, the DJQP cycle is allowed, for which the tunneling of the second quasiparticle is replaced by that of another Cooper pair. Combining Eq. 2.40 and Eq. 2.42, the energy required for JQP cycle can be expressed as

$$e V_{\text{sd}} \geq E_c + 2\Delta. \tag{2.43}$$

As illustrated in Fig. 2.6(b), the DJQP tunneling cycle involves a Cooper pair tunneling at one junction followed by a quasiparticle tunneling and a Cooper pair tunneling at the second junction, and finally a quasiparticle tunneling at the first junction and returning the island to its initial state. The DJQP cycle is also called the $3e$ cycle since it involves a total of three electrons tunneling at each junction. The tunneling process can be written as $|n\rangle \to |n+2\rangle \to |n+1\rangle \to |n-1\rangle \to |n\rangle$.

Similarly, the energy requirement for the DJQP cycle can be derived. The resonance conditions for both Cooper pairs tunneling are

$$2\kappa_2 e V_{\text{sd}} = E(n+2) - E(n) \tag{2.44}$$

$$2\kappa_1 e V_{\text{sd}} = E(n-1) - E(n+1) \tag{2.45}$$

Combining these two equations, we have

$$e V_{\text{sd}} = 2E_c \tag{2.46}$$

For the quasiparticles, we have

15

$$\kappa_1 eV_{\text{sd}} \geq E(n+1) - E(n+2) + 2\Delta, \tag{2.47}$$

and

$$\kappa_2 eV_{\text{sd}} \geq E(n) - E(n-1) + 2\Delta \tag{2.48}$$

which yield

$$eV_{\text{sd}} \geq 4\Delta - 4E_c. \tag{2.49}$$

In order to satisfy Eq. 2.46 and Eq. 2.49 simultaneously, we require $E_c \geq \frac{2}{3}\Delta$ for a DJQP feature to exist.

2.5   Josephson effects for the S-SET

The SIS junction is an example of a Josephson junction (JJ) [28]. It has a supercurrent that flows at zero voltage bias given by

$$I_s = I_c \sin \varphi. \tag{2.50}$$

Here φ is the phase difference of the Ginzburg-Landau wavefunction of the two electrodes, and the critical current I_c is the maximum supercurrent that can flow through the junction. If we apply a bias voltage across the junction, the phase difference will evolve, as given by

$$\dot{\varphi} = \frac{2eV_{\text{sd}}}{\hbar}. \tag{2.51}$$

This equation is a direct consequence of the coherent Cooper pair tunneling. φ is derived from integration of Eq. 2.51. Usually, φ is also defined as

$$\varphi = \frac{2\pi}{\Phi_0}\Phi, \tag{2.52}$$

where Φ is the magnetic flux through the JJ and $\Phi_0 = h/2e$ is the flux quantum.

The coupling free energy can be derived by integrating the electrical work, which is

$$E = \int I_s V_{\text{sd}} dt = \int \frac{\hbar I_c}{2e} \sin \varphi d\varphi = -E_J \cos \varphi + \text{const.} \tag{2.53}$$

where

$$E_J = \frac{\hbar I_c}{2e} \tag{2.54}$$

is the Josephson energy. Clearly, the total work is a minimum for $\varphi = 0$. In this case, the two superconducting electrode are weakly coupled.

By applying the microscopic theory to a tunnel junction, Ambegaokar and Baratoff [29] worked out the temperature dependance of I_c for the Josephson junction, which is given by

$$I_c R_N = (\frac{\pi \Delta}{2e}) \tan \frac{\Delta}{2k_B T}. \tag{2.55}$$

From Eq. 2.54 and Eq. 2.55 with $T \to 0$, we have the Josephson energy

$$E_J = \frac{h\Delta}{8e^2 R_N}. \tag{2.56}$$

Up to now, we have treated φ as a purely classical variable, which requires $E_J \gg E_c$, so that the phase is well defined. When $E_c \gg E_J$ the number of Cooper pairs on the island is well defined and dominated by the charging energy. When $E_J < E_c < \Delta$, the classical theory of the Josephson effects is modified by the quantum effects.

2.6 The radio frequency single electron transistor as a fast electrometer

Since the invention of the SET, there has been interest in using it as a fast electrometer. However, measurements of the current through SET are not very helpful due to its bandwidth limitations. Experimentally, the bias line connecting the sample to the room temperature circuit has a shunt capacitance on the order of a few nF. A SET with 100kΩ resistance will then have a bandwidth $1/RC \approx$ 5kHz. Another disadvantage of operating SET at DC is $1/f$ noise, which degrades the sensitivity of the SET. On the other hand, if we can operate the SET at radio frequency, not only can we eliminate $1/f$ noise, but can
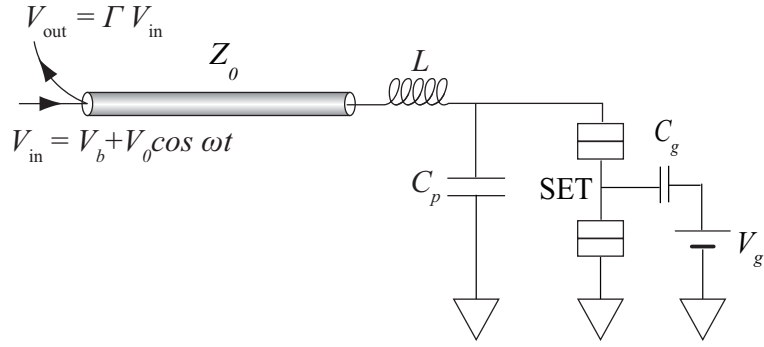
Figure 2.7. Idealized model of an LC matching network for the S-SET.

also operate it with a much larger bandwidth. This suggests such applications as counting electron tunneling in real time, which has more information about electron-electron correlations.

In 1998, Schoelkopf invented the radio frequency SET (RF-SET) [30], which is widely used for studying quantum computation, [31,32] spin based qubits, [33,34] the quantum properties of nanomechanical resonators, [35,36] and quantum measurement. [37] As illustrated in Fig. 2.7, the RF-SET has a lumped element impedance transforming resonator coupled to the SET. The circuit is also called a tank circuit. Fig. 2.7 shows the simplest case, in which the resonator is composed of an inductor, and a parasitic capacitor C_p, with a resonance frequency $f_0 = 1/\sqrt{C_p L}$. A more general resonator will be discussed later. The tank circuit transforms the impedance of SET at radio frequency to an impedance that is matched to the 50Ω RF transmission line. A carrier wave at f_0 is applied to the tank circuit and the reflected signal is measured. When we change the SET offset charge (V_g), the differential conductance (G_d) of SET and the damping of the resonator will change. The bandwidth of the RF-SET measurement is limited by the bandwidth of the resonance, given by f_0/Q, where Q is the quality of the tank circuit. For our tank circuit design, we can easily achieve a bandwidth of more than 50MHz.

CHAPTER 3

ON-CHIP SUPERCONDUCTING MATCHING NETWORK DESIGN AND QUANTITATIVE NOISE ANALYSIS FOR THE RF-SET

This chapter is devoted to discussing the superconducting matching network design for our S-SET. We compare lossy and lossless networks using S-matrix analysis, and then carry out a quantitative noise analysis.

3.1 Lossy matching networks
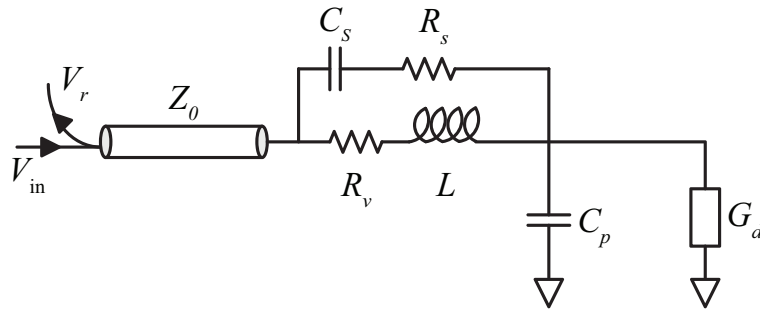
Figure 3.1. Schematic diagram of a lumped element RF-SET showing several possible sources of dissipation in the LC matching network. Such additional dissipation limits system performance.

As previously mentioned, the matching network converts the SET's high output impedance to the 50Ω standard impedance of RF transmission line and amplifiers. There are many different ways to achieve this, such as lumped element matching networks, quarter-wave transformers, multi-section matching transformer, etc. The first two methods have been tested in our laboratory. It turns out to be very difficult to fit a quarter-wave transformer into the sample holder. Embedding an SET in a lumped element network is significantly simpler.

S-matrix representation
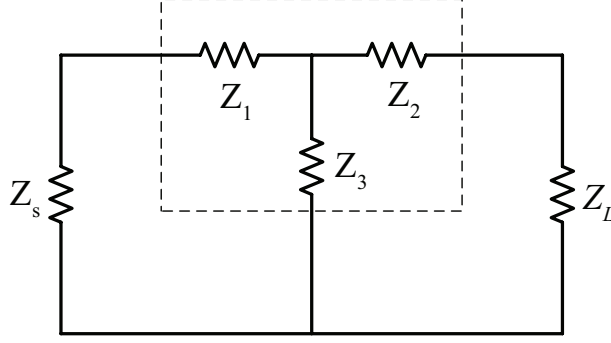
Figure 3.2. Equivalent two port S-matrix representation.

Fig. 3.1 demonstrates the schematic diagram of one of the most widely used lumped element tank circuit models for S-SET. In this model, C_s and R_s are shunt capacitance and resistance, L and R_v are the inductor and its wiring resistance, C_p is the parasitic capacitance and G_d is the S-SET's differential conductance. We can treat this network as a two-port network using S-matrix analysis [38]. Consider the generalized model for a matching network shown in Fig. 3.2. To derive the two port S-matrix for the matching network, we use the fact that the S-matrix can be represented in terms of the ABCD parameters, using

$$S_{11} = \frac{A + B/Z_0 - CZ_0 - D}{A + B/Z_0 + CZ_0 + D} \tag{3.1}$$

$$S_{12} = \frac{2(AD - BC)}{A + B/Z_0 + CZ_0 + D} \tag{3.2}$$

$$S_{21} = \frac{2}{A + B/Z_0 + CZ_0 + D} \tag{3.3}$$

and

$$S_{22} = \frac{-A + B/Z_0 - CZ_0 + D}{A + B/Z_0 + CZ_0 + D}. \tag{3.4}$$

For the network above, we have

$$A = 1 + \frac{Z_1}{Z_3}, \tag{3.5}$$

$$B = Z_1 + Z_2 + \frac{Z_1 Z_2}{Z_3}, \tag{3.6}$$

$$C = \frac{1}{Z_3}, \tag{3.7}$$

20

and

$$D = 1 + \frac{Z_2}{Z_3}.$$ (3.8)

These results assume a reference impedance of Z_0 for the S-matrix and assume that Z_0 represents the source impedance and R_d the load impedance. We can apply these results to derive the input S-matrix of the matching network S_{in} when we are treating S-SET as the load of the circuit. This is useful in calculating power delivered to the SET. In this case, as comparing Figs 3.1 and 3.2, we have

$$Z_1 = ((j\omega L + R_v)^{-1} + (\frac{1}{j\omega C_s} + R_s)^{-1})^{-1}$$ (3.9)

$Z_2 = 0$, and $Z_3 = 1/i\omega C_p$, and take the reference impedance of S_{in} to be Z_0. The components of the S-matrix are given by

$$S_{\text{in}}^{11} = \frac{Z_1 Z_0 - Z_0^2 + Z_1 Z_3}{Z_0(Z_1 + Z_0 + 2Z_3) + Z_1 Z_3}$$ (3.10)

$$S_{\text{in}}^{12} = S_{\text{in}}^{21} = \frac{2Z_0 Z_3}{Z_0(Z_1 + Z_0 + 2Z_3) + Z_1 Z_3}$$ (3.11)

$$S_{\text{in}}^{22} = \frac{-Z_0^2 - Z_0 Z_1 + Z_1 Z_3}{Z_0(Z_1 + Z_0 + 2Z_3) + Z_1 Z_3}.$$ (3.12)

It is also very useful to consider the S-SET to be the source and Z_0 the load. This point of view is useful for calculating the signal transferred from the SET to subsequent amplifiers. Here, we take R_d as the reference impedance and Z_0 as the load, so that $Z_0 \rightarrow R_d$ in Eq. 3.1-Eq. 3.4. In addition, we take $Z_1 = 0$, $Z_3 = 1/i\omega C_p$, and

$$Z_2 = ((j\omega L + R_v)^{-1} + (\frac{1}{j\omega C_s} + R_s)^{-1})^{-1}.$$ (3.13)

The S-matrix S_{out} describing power transfer from the SET is then given by

$$S_{\text{out}}^{11} = \frac{-R_d^2 - R_d Z_2 + Z_2 Z_3}{R_d^2 + R_d Z_2 + 2R_d Z_3 + Z_2 Z_3}$$ (3.14)

$$S_{\text{out}}^{12} = S_{\text{out}}^{21} = \frac{2R_d Z_3}{R_d^2 + R_d Z_2 + 2R_d Z_3 + Z_2 Z_3} \tag{3.15}$$

$$S_{\text{out}}^{22} = \frac{-R_d^2 + R_d Z_2 + Z_2 Z_3}{R_d^2 + R_d Z_2 + 2R_d Z_3 + Z_2 Z_3} \tag{3.16}$$
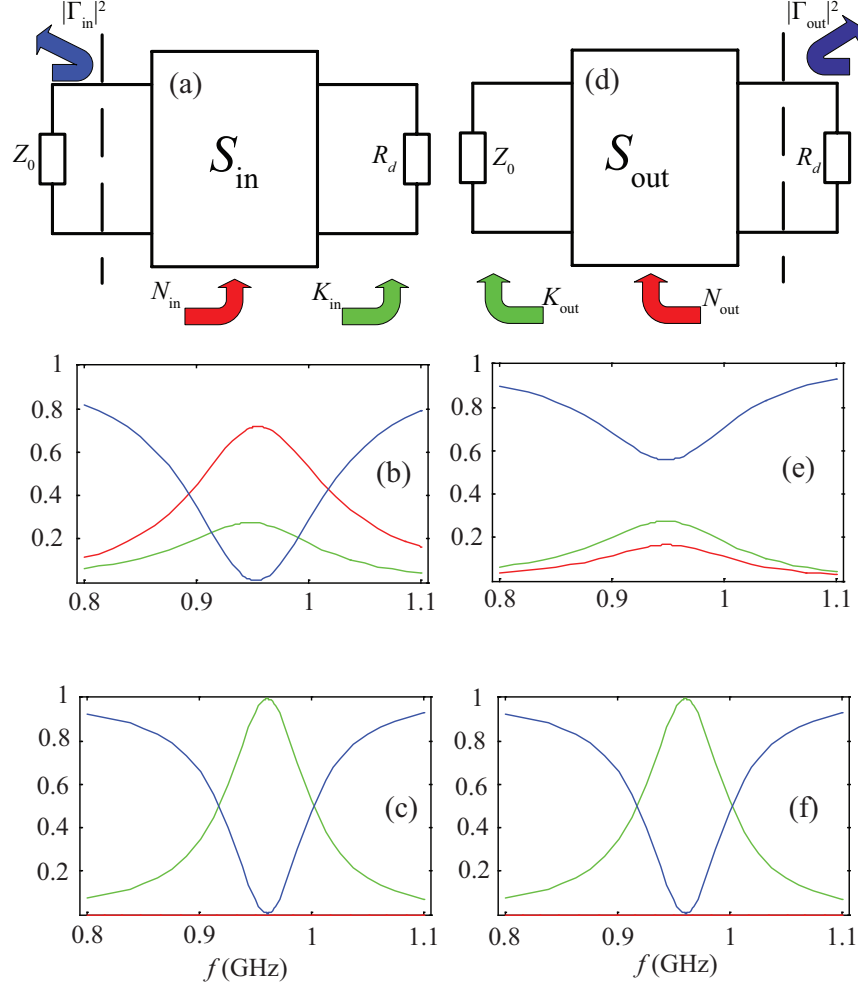
Figure 3.3. Effects of matching network losses on power transfer in the RF-SETs. (a) and (d): Schematic illustration of the S-matrix approach to power transfer. (b) and (c): Calculated values for $|\Gamma_{\text{in}}|^2$ (blue), K_{in} (green), and N_{in} (red) for lossy and lossless networks respectively. (e) and (f): Calculated values for $|\Gamma_{\text{out}}|^2$ (blue), K_{out} (green), and N_{out} (red) for lossy and lossless networks respectively.

The total incoming (outgoing) power is split into three portions, as illustrated in Fig. 3.3(a) and (d). $|\Gamma_{\text{in(out)}}|^2$ is the fraction that is reflected, $N_{\text{in(out)}}$ is the fraction dissipated in

the tank circuit, and $K_{\text{in(out)}}$ is the fraction transmitted to the SET or amplifier chain. $|\Gamma_{\text{in(out)}}|^2$, $K_{\text{in(out)}}$ and $N_{\text{in(out)}}$ are related by conservation of energy:

$$|\Gamma_{\text{in(out)}}|^2 + K_{\text{in(out)}} + N_{\text{in(out)}} = 1. \tag{3.17}$$

All these parameters can be derived from S_{in} and S_{out}, and are given by

$$\Gamma_{\text{in(out)}} = S^{11}_{\text{in(out)}} + \frac{S^{12}_{\text{in(out)}} S^{21}_{\text{in(out)}} \Gamma^l_{\text{in(out)}}}{1 - S^{22}_{\text{in(out)}} \Gamma^l_{\text{in(out)}}}, \tag{3.18}$$

in which,

$$\Gamma^l_{\text{in}} = -\Gamma^l_{\text{out}} = \frac{R_d - Z_0}{R_d + Z_0} \tag{3.19}$$

$$K_{\text{in(out)}} = \frac{|S^{21}_{\text{in(out)}} \times S^{21}_{\text{in(out)}} \times (1 - |\Gamma^l_{\text{in(out)}}|^2)|}{|1 - S^{22}_{\text{in(out)}} \Gamma^l_{\text{in(out)}}|^2} \tag{3.20}$$

In Fig. 3.3(b) and (c), we plot $|\Gamma_{\text{in}}|^2$, K_{in} and N_{in} for a lossy network as well as for an ideal one. For an ideal matching network, we have $R_s \approx R_v \approx 0$, and assume $C_s \approx 0$. For a
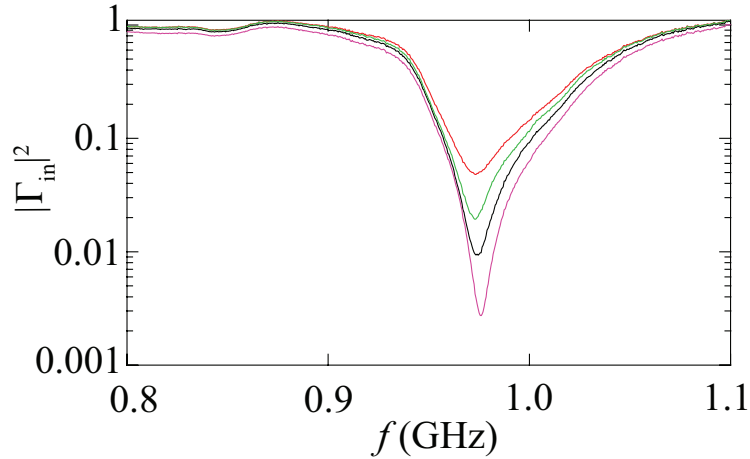
Figure 3.4. $|\Gamma_{\text{in}}|^2$ versus frequency for a 82nH Panasonic chip inductor. From top to bottom, center of the gap (red), $R_d = 37\text{k}\Omega$ (green), $R_d = 21\text{k}\Omega$ (black), $R_d = 17.8\text{k}\Omega$ (purple).

lossy network, as shown in the figure, since energy is lost in the tank circuit ($N_{\text{in}} > 0$), we always have $K_{\text{in}} < 1$ even we have perfect matching $\Gamma_{\text{in}} = 0$. Only for a lossless network, as shown in Fig. 3.3(c), is all the incoming power transmitted to the S-SET ($K_{\text{in}} = 1, \Gamma_{\text{in}} = 0$) when we have perfect matching.

More importantly, we must take a similar view when considering signal arising from the S-SET that to be transmitted to the measurement electronics. Here, a nonzero value of N_{out} has more severe consequences, as some of the signal from the S-SET, which contains some information regarding the quantum states of the measured system, will be lost, as indicated in Fig. 3.3(e). Only if the matching network provides perfect matching ($\Gamma_{\mathrm{out}} = 0$) and is lossless ($N_{\mathrm{out}} = 0$) will all the information from the S-SET be transmitted to the measurement electronics.

Panasonic ELJ 82nH resonator

To demonstrate the importance of an on-chip superconducting matching network, we embedded the S-SET in a tank circuit consisting of an RF chip inductor (Panasonic ELJ 82nH) and its parasitic capacitance. Due to its physical size (usually 1.5mm × 1mm), the Panasonic chip had negligible C_s while R_v was the dominate lossy element. Experimentally, we find the use of an industry fabricated inductor has minimum C_p on the order of 0.3-0.4pF, about twice as large as that of our superconducting resonator. In order to keep the resonance frequency fixed, a lower L must be used. This then lowers the ratio L/C_p, which transforms shot noise S_I to a voltage noise $S_V = (L/C_p)S_I$ at the input of the HEMT, the secondary amplifier connecting to S-SET.

Fig. 3.4 shows the measured $|\Gamma_{\mathrm{in}}|^2$ for different G_d of the S-SET [39] using a resonator with a Panasonic ELJ 82nH rf chip inductor. As shown in the figure, even we bias the S-SET near the center of the superconducting gap where it has a differential resistance several MΩ, only about 5 percent of the total power is reflected rather than the near 100 percent reflection expected for a lossless network. The other 95 percent of the power has been lost to the tank circuit. Therefore, if the intrinsic signal from the S-SET is not significantly larger than the HEMT input noise, it will likely to be overwhelmed by the HEMT noise due to the huge losses in tank circuit. A simulation based on the S-matrix calculation neglecting the contribution from C_s yields $R_v \approx 30\Omega$, which is a reasonable value when operating at $f_0 \approx 1\mathrm{GHz}$ and 290mK.

In general, the lossy resonator shown in Fig. 3.1 poses a problem for several reasons. First, it is very difficult to characterize. There are five unknowns (L, C_p, C_s, R_v and R_s),

some of which only appear in specific combinations in S-matrix calculation, which makes the modeling extremely difficult. Second, since our detection technique depends on measuring variations in the dissipation in the tank circuit, the presence of dissipation that is not sensitive to the signal (the charge coupled to the SET island, for example) reduces the sensitivity of the detector. Finally, by the fluctuation-dissipation theorem, dissipation in the matching network introduces an additional source of noise that both acts back on the object being measured, and adds additional noise at the detector output, [40] inevitably pushing it further from the quantum limit.

3.2   On-chip superconducting matching network analysis

Our initial superconducting matching network consisted of an LC resonator on a separate GaAs chip fabricated with photolithography connected to an SET on another chip by wire bonds. Such structures suffered from more complex fabrication procedures and long wires that increase the stray capacitance C_s. On-chip networks, in contrast, can be fabricated together with the SET on the same small chip using electron-beam lithography. The wire bond connecting the device to the coaxial feedline is kept as short as possible to minimize any extra capacitance.

We investigated matching network designs using a spiral inductor and an interdigitated capacitors to provide engineered L and C_p values. However, for a desired impedance matching, the designed C_p will pull the resonance of the tank circuit outside of the HEMT's bandwidth. Also, as we will discuss in this chapter, a lower resonant frequency will lead to a narrower bandwidth and offer a lower gain for the tank circuit. Even without a designed interdigitated capacitor, C_p was still relatively large.

Our improved design only involves designing a spiral inductor. Analytic design of a spiral inductor is not simple. Many different models have been used to provide estimated inductance values. We will show one of the most popular models. As shown in Fig. 3.5, the spiral has rectangular bonding pads for the rf line on two of its sides. The inductance of this geometry is given by [41]
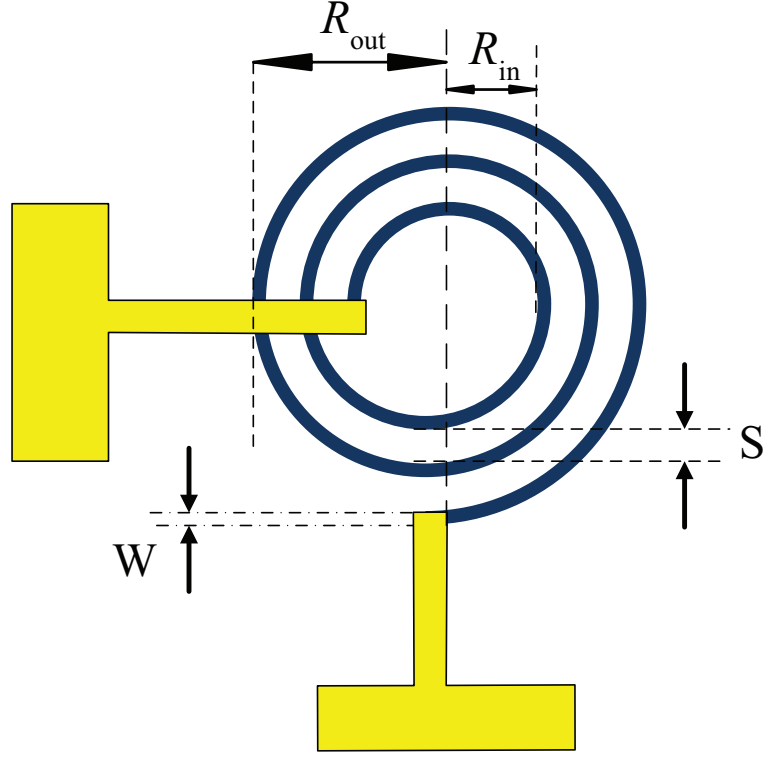
Figure 3.5. Planar circular spiral model.

$$L = 2.0 \sum_{k=1}^{n-1} \sum_{j=k+1}^{n} \mu\sqrt{ab}[(\frac{2.0}{k_1} - 1.0)K(k_1) - \frac{2.0}{k_1}E(k_1)] \tag{3.21}$$

$$+ \sum_{k=1}^{n} \mu(2.0c - w_1)[(1.0 - \frac{k_2^2}{2.0})K(k_2) - E(k_2)] \tag{3.22}$$

where

$$k_1 = \sqrt{\frac{4ab}{(a+b)^2}} \tag{3.23}$$

and

$$k_2 = \sqrt{\frac{4c(c-w_1)^2}{(2c-w_1)}} \tag{3.24}$$

a is the mean radius, b is the thickness of the inductor, $c = R_{out} - R_{in}$, n is the number of turns of spiral, and w_1 is the half width of one turn. The functions $K(k)$ and $E(k)$ are the complete elliptic integrals of the first and second kind. Substituting the parameters of our spiral inductor, this model estimates $L \approx 450$nH. Like most of the other theoretical predictions, this model fails to give a good estimate for a superconducting inductor.

26

We determine L and C_p experimentally. Since the measurement is carried out at 290mK, losses in on-chip superconducting matching network are negligible at the operating frequency $f_0 \approx 1\text{GHz}$. We assume that C_s is negligible and $R_v \approx 0$. We make use of two fundamental characteristics of a resonator: the resonance frequency f_0 and the quality factor Q. The resonant frequency f_0 is given by

$$f_0 = \frac{1}{2\pi\sqrt{LC_p}}. \tag{3.25}$$

Generally, Q is defined in terms of the ratio of the peak energy stored in the resonator to that of the energy being lost in one cycle. For our LC resonator, the external quality factor of the resonator Q_0 due to loading by the coaxial feedline, is given by:

$$Q_0 = \sqrt{L/C_p}/Z_0 \tag{3.26}$$

Q_{SET} describes the damping effect from the SET, and is given by

$$Q_{\text{SET}} = \sqrt{C_p/L}/G_d. \tag{3.27}$$

Q_{SET} will change dynamically with different G_d. The total quality factor Q_T of the S-SET matching network system is then given by:

$$Q_T^{-1} = Q_0^{-1} + Q_{\text{SET}}^{-1}. \tag{3.28}$$

The bandwidth of the resonator is defined as the ratio of $\frac{f_0}{2\pi Q_T}$. When treating the SET as the load, at f_0, the reflection coefficient is given by

$$\Gamma_{\text{in}} = \frac{Z - Z_0}{Z + Z_0} = \frac{G_d L/C_p - Z_0}{G_d L/C_p + Z_0}. \tag{3.29}$$

For perfect matching ($\Gamma_{\text{in}} = 0$), $Q_0 = Q_{\text{SET}} = 2Q_T$.

As illustrated in Fig. 3.6(a), we measured the reflected power from the on-chip superconducting matching network consisting of a 14 turn spiral inductor for different G_d. The
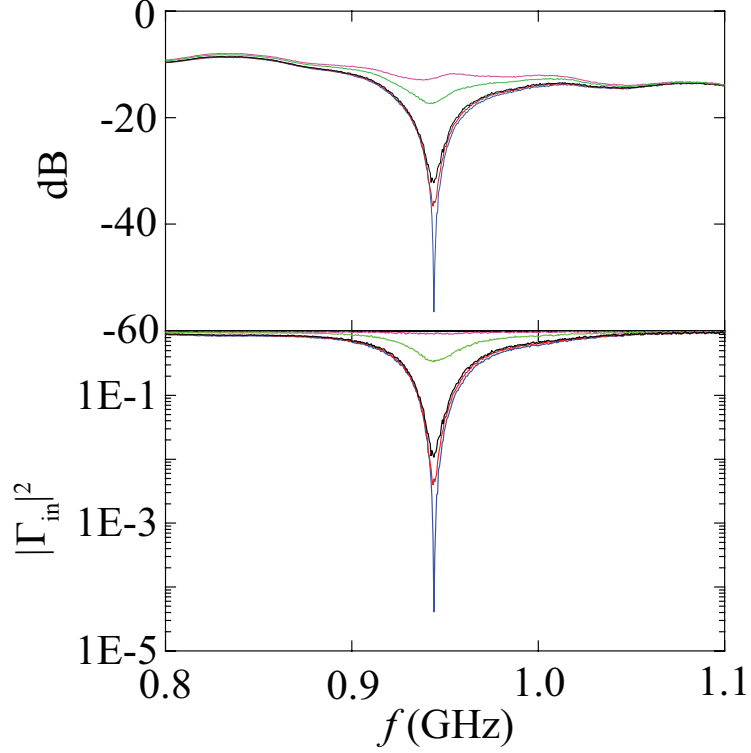
Figure 3.6. (a) Reflected power versus frequency for an LC superconducting matching network. Top to bottom, center of the gap (purple), $R_d = 40\text{k}\Omega$ (green), $R_d = 28.2\text{k}\Omega$ (black), $R_d = 22.2\text{k}\Omega$ (red), $R_d = 19.2\text{k}\Omega$ (blue) (b) $|\Gamma_{\text{in}}|^2$ versus frequency derived from (a).

reflected power can be converted to the reflection coefficient shown in Fig. 3.6(b). The sharp dip for $R_d \approx 19.2\text{k}\Omega$ around 940MHz indicates near perfect matching. Combining Eq. 3.25 and Eq. 3.29, and using the measured value of f_0 and Γ_{in}, we solve for $L \approx 167\text{nH}$ and $C_p \approx 0.17\text{pF}$. We can also check the values of L and C_p by substituting other values of R_d in Fig. 3.6 to Eq. 3.29 and the corresponding measured values of Γ_{in}. The resulting values of L and C_p are independent of the values of R_d chosen.

Using the values of L and C_p, we find $Q_0 = 20$. The bandwidth of the resonance is around 10MHz. Our earlier L and C_p values gave a perfect matching to $R_d \approx 20\text{k}\Omega$ [39] while our samples have R_d around 35kΩ in the subgap region. Eq. 3.29 indicates that we have to make C_p as small as possible while increasing L to keep the $f_0 \approx 1\text{GHz}$ while obtaining better matching for higher R_d. Unfortunately, increasing the turns of the inductor will increase the size of the matching network and therefore increase C_p. We made the geometry of

LC resonator more compact to give a slightly smaller $C_p = 0.14\text{pF}$ which gave perfect impedance matching to $R_d = 25\text{k}\Omega$. [4]

Although we have not achieved perfect matching for DJQP region where the S-SET is predicted to have the ideal balance of sensitivity and backaction needed to approach the quantum limit, the on-chip superconducting matching network is still a tremendous improvement, since losses in the tank circuit itself are negligible. Also, the resonator can be extended to multipole matching networks [42] that can further increase the bandwidth, possibly allowing measurements on nanosecond time scales.
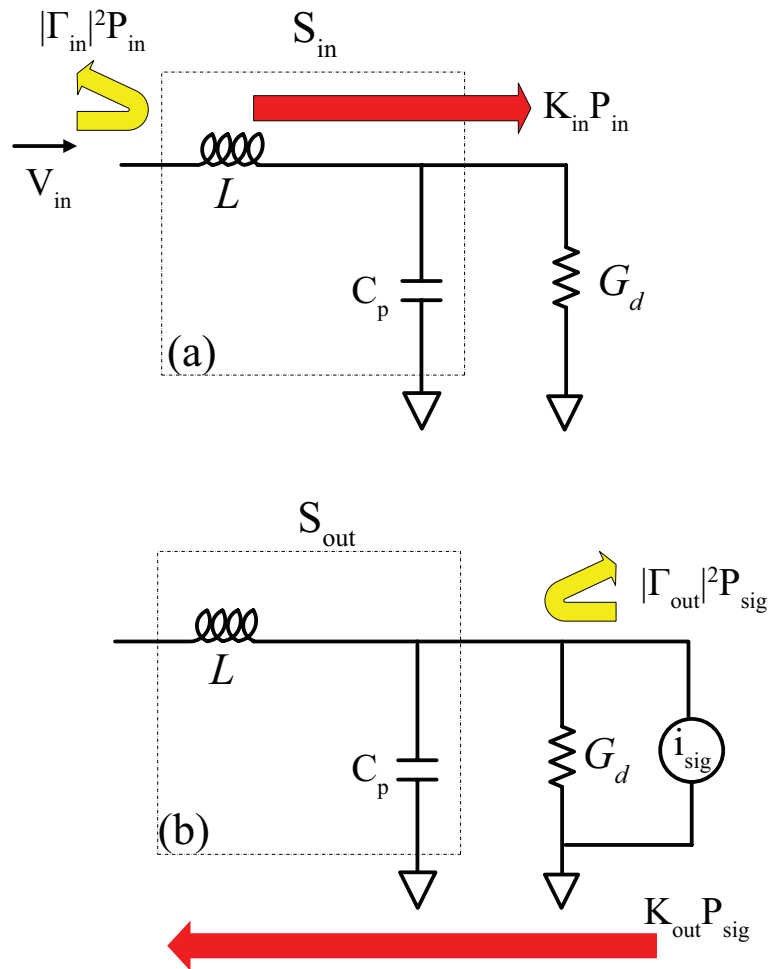
Figure 3.7. (a) S_{in} and (b) S_{out} representation of the on-chip superconducting matching network.

3.3 Analyzing the modulation signal from an RF-SSET

Based on S-matrix analysis, we have two ways to analyze the modulation signal from an RF-SSET. The traditional way is to treat SET as the load and consider the variation in reflection power with R_d. Assume the RF-SSET offset charge is varied sinusoidally as $q_0 \cos \omega_m t$. This will give rise to an amplitude modulated reflected wave given by

$$V_r = \frac{\partial \Gamma_{\text{in}}}{\partial G_d} \frac{\partial G_d}{\partial n_g} q_0 \cos (\omega_m t) V_{\text{in}}, \tag{3.30}$$

where $e n_g$ is the offset charge, q_0 is the rms amplitude of the charge modulation, ω_m is the modulation frequency and V_{in} is the rms amplitude of the carrier wave. The power in the reflected wave is given by

$$|\Gamma_{\text{in}}|^2 P_{\text{in}} = \frac{V_{\text{in}}^2}{Z_0} |\frac{\partial \Gamma_{\text{in}}}{\partial G_d}|^2 (\frac{\partial G_d}{\partial n_g})^2 q_0^2 \cos^2(\omega_m t) \cos^2(\omega_0 t). \tag{3.31}$$

Using Eq. 3.29, we have

$$|\frac{\partial \Gamma_{\text{in}}}{\partial G_d}| = \frac{2 L C_p Z_0}{(L G_d + C_p Z_0)^2}. \tag{3.32}$$

Another way to view this problem is to consider the power transfer first from the rf source to the S-SET and then from the S-SET to the amplifier chain. Power from the input wave is delivered to the S-SET, providing an ac bias voltage. This voltage causes an ac current that is modulated by changes in the SET conductance G_d. The modulated current gives rise to a wave that propagates out through the matching network, then giving rise to an outgoing amplitude modulated wave. As shown schematically in Fig. 3.7(a), the fraction of power reflected by the matching network is $|\Gamma_{\text{in}}|^2 P_{\text{in}}$, while the fraction delivered to the S-SET is $K_{\text{in}} P_{\text{in}}$ where P_{in} is the incoming power. For a lossless network, $N_{\text{in}} = 0$, giving $K_{\text{in}} + |\Gamma_{\text{in}}|^2 = 1$. We treat the S-SET as an amplitude modulated current source as shown in Fig. 3.7(b). In linear response,

$$I_{\text{sig}} = \frac{\partial G_d}{\partial n_g} q_0 V_{\text{SET}} \cos (\omega_m t) \cos (\omega_0 t) \tag{3.33}$$

where V_{SET} is the rf voltage across the SET. From the diagram, the power dissipated in the SET is the power delivered by the incoming wave:

$$G_d V_{\text{SET}}^2 = K_{\text{in}} \frac{V_{\text{in}}^2}{Z_0}. \tag{3.34}$$

The corresponding signal voltage is given by

$$V_{\text{sig}} = \frac{I_{\text{sig}}}{G_d}. \tag{3.35}$$

In this case, we treat the network as having a characteristic impedance R_d. Therefore, the source (S-SET) and the network have equal impedances, and only $1/4$ of the total power from the S-SET is available to the network. The available signal power is

$$P_{\text{sig}} = \frac{1}{4} G_d V_{\text{sig}}^2. \tag{3.36}$$

The actual power transfer from the S-SET to HEMT is given by $K_{\text{out}} P_{\text{sig}}$. Combining Eq. 3.33-Eq. 3.36, we have

$$K_{\text{out}} P_{\text{sig}} = \frac{K_{\text{in}} K_{\text{out}}}{4 G_d^2} \frac{V_{\text{in}}^2}{Z_0} \left(\frac{\partial G_d}{\partial n_g}\right)^2 q_0^2 \cos^2(\omega_m t) \cos^2(\omega_0 t). \tag{3.37}$$

The signal we can measure experimentally is the average of Eq. 3.37.

Comparing Eq. 3.31 and Eq. 3.37, we find the two methods are equivalent if

$$\frac{K_{\text{in}} K_{\text{out}}}{4 G_d^2} = \left|\frac{\partial \Gamma_{\text{in}}}{\partial G_d}\right|^2. \tag{3.38}$$

We begin with the lossless resonator. From S matrix calculation and Eq. 3.20, at resonance f_0, K_{in} and K_{out} are given by

$$K_{\text{in}} \approx K_{\text{out}} = \frac{4 G_d L C_p Z_0}{(L G_d + C_p Z_0)^2}. \tag{3.39}$$

The approximation is due to the difference in resonant frequency when evaluating S_{in} ($f_1 = 2\pi \sqrt{\frac{1}{LC_p} - \frac{1}{C_p^2 R_d^2}}$) and S_{out} ($f_2 = 2\pi \sqrt{\frac{1}{LC_p} - (\frac{Z_0}{L})^2}$). From the measured C_p , L

and typical R_d values, these two resonant frequencies are very close to f_0 with error less than 1%. Given Eq. 3.39, it is clear Eq. 3.70 is satisfied. We also did a complete S matrix calculation for the lossy network at different frequencies shown in Fig. 3.3(b), (e) and find that Eq. 3.70 is still valid.

Derivation of charge sensitivity and effective temperature of S-SET

Although the S-SET is a non-equilibrium and non-Gaussian device, it can be shown that for a weakly coupled system and at the resonant frequency of the LC resonator, an S-SET can still be treated as an effective thermal bath described by an effective temperature T_{SET} and damping rate γ_{SET}. Since the back-action of the RF-SSET mimics the effects of a thermal bath, we can convert the back-action to an effective bath if we know the noise properties of an RF-SSET.

In general, the resonator responds to a variety of frequencies and we can not characterize the backaction of the S-SET by one single temperature. However, if the resonator has a sufficiently high quality factor (narrow bandwidth), the effective temperature can be treated as constant over its bandwidth. Additionally, we also have a large separation in timescale between the S-SET tunneling rates (tens of GHz) and the inverse response time of the LC resonator ($f_0/Q_{tank} \approx 20\text{MHz}$).

In our S-SET/LC resonator system, the thermal bath model is essentially a characterization of the energy transfer between the RF-SSET and the tank circuit. The thermal bath can be a source of white Johnson noise, with the power spectral density nearly equal throughout the frequency domain. Within the thermal bath description, we assume that the orthodox model still applies, that is, tunneling events are stochastic. The effective temperature for a normal metal SET is roughly proportional to the source drain voltage in the conductor. However, if we consider an S-SET coupled to a LC resonator and focus on the sub-gap regimes where transport in the S-SET is via the incoherent tunneling of Cooper pairs (DJQP and JQP), the effective temperature is not related to the ambient temperature or source drain bias. It describes the ratio of symmetric and asymmetric quantum noise and can be smaller than either the S-SET's ambient temperature or its source drain bias eV_{sd}, meaning that considerable cooling can be accomplished.

The rf circuit used for fast charge detection is shown in Fig. 3.8. We have installed a circulator, HEMT and GaAs FET amplifier between the tank circuit and the macroscopic world. The total measured noise in a bandwidth of Δf including the S-SET, amplifiers,
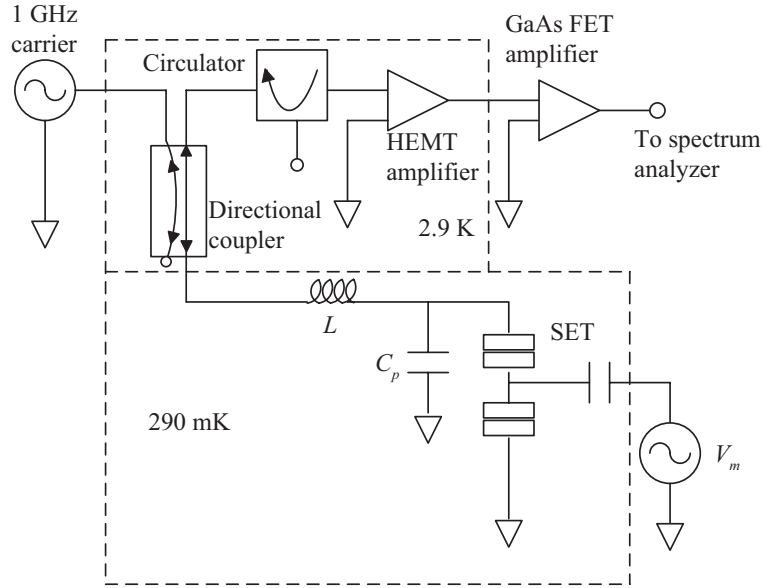
Figure 3.8. Schematic layout of the rf circuitry used for fast charge detection. The directional coupler is used to direct the incoming and outgoing waves, while the circulator prevents noise from a subsequent cryogenic HEMT amplifier from reaching the detector.

circulators, and matching network is then given by

$$P_{\text{tot}} = K_{\text{out}}k_B T_{\text{SET}} + k_B T_{\text{HEMT}} + k_B |\Gamma_{\text{in}}|^2 T_{\text{circ}} + N_{\text{out}} k_B T_{\text{tank}}, \tag{3.40}$$

where P_{tot} is the total power referred to the input of the amplifier, T_{HEMT} is the noise temperature of HEMT, T_{circ} is the circulator's noise temperature, and T_{tank} is the ambient temperature of the matching network. Note that $N_{\text{out}} \approx 0$ for a superconducting matching network.

The signal to noise ratio for a charge modulation signal is defined as

$$\text{SNR} = \frac{K_{\text{out}}\bar{P}_{\text{sig}}}{P_{\text{tot}}} \tag{3.41}$$

where $\bar{P}_{\text{sig}}$ is the average of Eq. 3.37.

The charge sensitivity δq is given by

$$(\delta q)^2 = \frac{(q_0/e)^2}{2}(\frac{e}{\sqrt{\text{Hz}}}) \tag{3.42}$$

for a charge modulation q_0 such that SNR = 1, giving

$$\delta q = \frac{G_d}{|\frac{\partial G_d}{\partial n_g}|V_{\text{in}}e}\sqrt{\frac{2Z_0k_B}{K_{\text{in}}}(T_{\text{SET}} + \frac{T_{\text{HEMT}}}{K_{\text{out}}} + \frac{|\Gamma_{\text{in}}|^2T_{\text{circ}}}{K_{\text{out}}} + \frac{N_{\text{out}}}{K_{\text{out}}}T_{\text{tank}})}. \tag{3.43}$$

Eq. 3.43 indicates that both the intrinsic properties of S-SET and the performance of the matching network affect δq. For a perfectly matched superconducting network, we can neglect the noise contributions of the circulator and resonator since $|\Gamma_{\text{in}}|^2 \approx 0$, and $N_{\text{out}} = 0$. In contrast, a lossy, poorly matched resonator will magnify the noise contribution from the HEMT, since in this case $K_{\text{in}}, K_{\text{out}} < 1$, which can easily overwhelm the intrinsic quantum noise from the S-SET. Therefore, in order to fabricate a near-quantum limited RF-SET, a nearly perfect matching network and a good sample are both required.

Eq. 3.40 helps us determine T_{SET} from the total measured power $\mathcal{P}_{\text{meas}}$ in a bandwidth Δf. For a lossless tank circuit, the total integrated power we measure referred to the input of the HEMT amplifier is

$$\mathcal{P}_{\text{meas}} = (K_{\text{out}}k_BT_{\text{SET}} + k_BT_{\text{HEMT}} + |\Gamma_{\text{in}}|^2k_BT_{\text{circ}})\Delta f \tag{3.44}$$

where Δf is the bandwidth of the noise power measurement. Since K_{out} is frequency dependent, the total intrinsic noise contribution from the S-SET is given by $k_BT_{\text{SET}}\int_{f_0}^{f_0+\Delta f} K_{\text{out}}df \approx 4(k_BT_{\text{SET}})Q_T^2G_dZ_0\Delta f$.

We replace Q_T with ω_0/γ_T where γ_T describes the total damping rate of the resonator due to both the SET and coupling to a feedline of impedance Z_0, and is given by

$$\gamma_T = \gamma_0 + \gamma_{\text{SET}} = Z_0/L + G_d/C_p. \tag{3.45}$$

Defining $\mathcal{P}_{\text{SET}} = \mathcal{P}_{\text{meas}} - k_BT_{\text{HEMT}}\Delta f$, we then have

$$\mathcal{P}_{\text{SET}} = 4k_B(\omega_0/\gamma_T)^2Z_0G_dT_{\text{SET}}\Delta f. \tag{3.46}$$
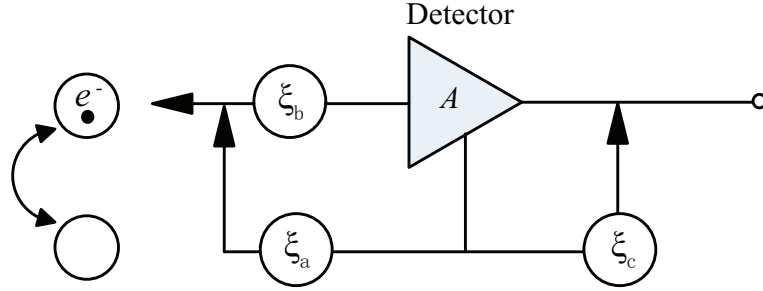
Figure 3.9. Model circuit illustrating different possible noise sources during a quantum measurement process. Here a detector with noise sources ξ_a, ξ_b and ξ_c is used to detect the position of a single excess electron on a double quantum dot (DQD).

3.4   Analysis of quantum noise measurement of an RF-SSET

Quantum noise measurement has challenged physicists for almost a century. Classically, there is no lower bound on the noise a measurement may add. Quantum mechanically, measuring a system necessarily perturbs it. For electrical amplifiers such as RF-SSET, this means that improved sensitivity requires increased backaction that itself contributes noise.

This interest in studying the connections between noise and quantum measurement has blossomed within the condensed matter community due to development of electrical devices that are good physical representations of quantum two-level systems. [43–46] Furthermore, due to development of fast readout techniques [33,47] such as the RF-SSET, there has been significant theoretical effort to better understand the quantum measurement process for an individual system as opposed to an ensemble [48–51] and also to better understand the relationship between intrinsic noise of a detector and its efficiency as a measuring device. [52–56]

To illustrate the physics involved, it is useful to look at a simple model as illustrated in Fig. 3.9. It shows the different possible noise sources during a quantum measurement process experimentally. [57] For illustration purpose, the quantum system to be measured is a double quantum dot (DQD) containing a single excess electron. Here, we model the quantum amplifier (RF-SSET) as consisting of an ideal noiseless amplifier with gain A, with three noise sources ξ_b, ξ_a and ξ_c. Among these sources, ξ_b and ξ_a are intrinsic to the amplifier

itself, with ξ_b representing the backaction noise essential for the measurement process and ξ_a representing additional classical noise that dephases the measurement. ξ_c is the classical noise source associated with additional amplifiers that connected to the quantum amplifier and are required to produce a measurable signal. The noise contribution from ξ_c must be kept as small as possible in order to approach the quantum limit. The intrinsic noise sources ξ_b and ξ_a indicates that not all the quantum amplifiers are equally efficient. For example, a normal state SET is a very inefficient quantum detector for which the extra dephasing noise ξ_a is significant [58]. In contrast, a S-SET is expected to have a relatively small ξ_a when biased near the DJQP cycle.
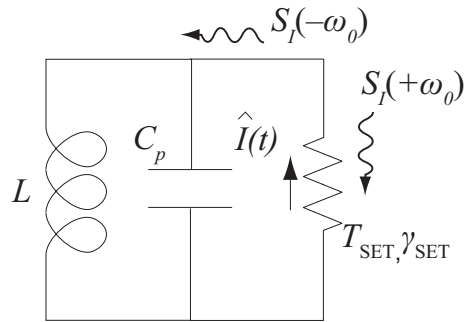
Figure 3.10. Model for an S-SET/resonator, showing the S-SET as an effective bath with temperature T_{SET} and damping rate γ_{SET}. The asymmetric current noise $S_I(+\omega_0)$ and $S_I(-\omega_0)$ is related to the probability of the S-SET absorbing or emitting a photon.

As we mentioned earlier, to detect charge we bias the SET with V_{sd} and measure the current through it. Motion of charges near the SET causes changes in G_d, resulting in changes in I. The ultimate sensitivity of the SET operated in this way is set by the non-equilibrium current noise (shot noise) present in $I(t)$. The same current fluctuations also determines its backaction and its proximity to the quantum limit.

Classically, current noise is described by a spectral density $S_I^{\mathrm{sym}}(\omega)$, which is symmetric in the frequency domain. However, quantum mechanically, we have to distinguish between positive frequency noise and negative frequency noise. Positive frequency noise transfers energy from a measured system to the electrometer (RF-SSET) and negative frequency noise transfers energy from the electrometer to the measured system. An electrometer coupled to a ground state qubit illustrates the idea. [59] From a Fermi's golden rule calculation,

the transition rate for the qubit from ground state to the excited state is proportional to $S_I(-\omega_0)$, where

$$S_I(-\omega_0) = \int_{-\infty}^{+\infty} \mathrm{d}t\, e^{-i\omega t} \langle I(t)I(0)\rangle \tag{3.47}$$

is the unsymmetrized quantum noise spectrum of the electrometer current and $\hbar\omega_0$ is the separation in energy between the ground states and excited states. Similarly, the rate at which a system in the excited state decays to the ground state given by $S_I(+\omega_0)$. To make a complete measurement of quantum noise, we must obtain information about $S_I(+\omega_0)$ and $S_I(-\omega_0)$.

Symmetric and asymmetric quantum noise for the S-SET/resonator

Instead of coupling our S-SET to a two-level system to carry out our quantum noise measurement, we couple it to a harmonic oscillator consisting of an on-chip superconducting LC matching network as shown in Fig. 3.8. In our SSET/resonator system, the symmetrized and asymmetrized shot noise of the S-SET at f_0 is related to either emission or absorption of energy from the resonator.

We proceed by making an analog to a nanomechanical oscillator capacitively coupled to an S-SET, for which the Hamiltonian is given by

$$\mathcal{H} = \frac{1}{2m}\hat{p}^2 + \frac{1}{2}m\omega^2\hat{x}^2 - \hat{F}(t)\hat{x}. \tag{3.48}$$

Here $\hat{x}$ and $\hat{p}$ are the position and momentum operators for the oscillator, m is its mass and $\hat{F}(t)$ is the force the S-SET exerts on the oscillator. When accounting for the damping of the charge detector, we have

$$S_F(\omega_0) + S_F(-\omega_0) = 2\hbar\omega_0\gamma m \coth\frac{\hbar\omega_0}{2k_B T_{\mathrm{eff}}}, \tag{3.49}$$

$$S_F(\omega_0) - S_F(-\omega_0) = 2\hbar\omega_0\gamma m, \tag{3.50}$$

where $S_F(\pm\omega_0)$ is the quantum noise spectrum of the back-action force, T_{eff} is the effective temperature and γ is the damping rate of the harmonic oscillator.

We can make a similar argument for the S-SET/resonator. The Hamiltonian can be expressed by substituting $\hat{x} \to \hat{\Phi}$, $\hat{p} \to \hat{Q}$, $\hat{F}(t) \to \hat{I}(t)$, $m\omega_0^2 \to 1/L$, and $C \to m$. It is given by

$$\mathcal{H} = \frac{1}{2L}\hat{\Phi}^2 + \frac{1}{2C}\hat{Q}^2 - \hat{I}(t)\hat{\Phi}, \qquad (3.51)$$

where $\hat{\Phi}$ is the flux in L, $\hat{Q}$ is the charge on the capacitor and $\hat{I}(t)$ is the operator describing the noisy current flowing through the S-SET. As was illustrated in Fig. 3.10, SSET/resonator is characterized by an effective temperature T_{SET} and a damping rate γ_{SET}, [40,60,61] assuming that the intrinsic damping of the resonator can be neglected, which is valid for our superconducting on-chip networks. In most cases, $\hbar\omega_0 \ll k_B T_{\text{eff}}$, and substituting $S_F(\omega_0) \to S_I(\omega_0)$, $T_{\text{eff}} \to T_{\text{SET}}$, $\gamma \to \gamma_{\text{SET}}$, we have

$$S_I(\omega_0) + S_I(-\omega_0) = 4k_B T_{\text{SET}} C_p \gamma_{\text{SET}}, \qquad (3.52)$$

and

$$S_I(\omega_0) - S_I(-\omega_0) = 2\hbar\omega_0 C_p \gamma_{\text{SET}}. \qquad (3.53)$$

In order to make a complete noise measurement, it is not necessary to measure $S_I(+\omega_0)$ or $S_I(-\omega_0)$ separately, as has been done in other systems. [62–64] As long as two linearly independent combinations can be measured, complete noise information is obtained.

The effective temperature T_{SET} can be either positive or negative, as can γ_{SET}, depending on whether absorption or emission of a photon, respectively, dominates the quantum noise. Because the S-SET's electromagnetic environment is dominated by the LC resonator, most absorption (emission) will take the form of photon exchange with the tank circuit as shown in Fig. 3.10. [65]

In our LC model, there are two different methods to derive γ_{SET}. One is from

$$\gamma_{\text{SET}} = G_d/C_p, \qquad (3.54)$$

where both G_d and C_p are determined from the measurement. The other method is from the definition

$$\Gamma_{\text{in}} = \frac{\gamma_{\text{SET}} - Z_0/L}{\gamma_{\text{SET}} + Z_0/L}, \qquad (3.55)$$

rewrite this, $\gamma_{\text{SET}} = \frac{Z_0(1+\Gamma_{\text{in}})}{L(1-\Gamma_{\text{in}})}$. L and Γ_{in} can also be obtained experimentally. Both methods give about the same results.

Proximity to the quantum limit

It is useful to have some methods of characterizing how closely SET approaches the quantum limit. There are a variety of ways of doing so. One way is to use the uncoupled energy sensitivity, which is given by $\delta\epsilon = (\delta q)^2/(2C_\Sigma)$. In this case, the quantum limit is defined by the intrinsic property of the S-SET and it is not coupled to any device under test.

The other method is to consider a coupled system, such as an SSET/resonator coupling to a QD. We begin with the relationship [10]

$$\chi = \sqrt{\frac{\tau_{\text{meas}}}{\tau_\varphi}} \geq 1 \tag{3.56}$$

where τ_{meas} is the minimum time required to distinguish between two charge states and is associated with the intrinsic noise of the SET, and τ_φ is the time required for charge fluctuations on the S-SET island to dephase the object it is measuring. From the basic principle of quantum mechanics, one has the relationship $\tau_{\text{meas}} \geq \tau_\varphi$, since the original quantum states have collapsed by the time the measurement has been performed. For an efficient quantum measurement, approaching the quantum limit also means to read the quantum information as fast as possible to make χ close to 1. τ_{meas} and τ_φ are given by [9]

$$\tau_{\text{meas}}^{-1} = \frac{(\Delta I)^2}{4S_I^{\text{sym}}} \tag{3.57}$$

and

$$\tau_\varphi^{-1} = (\frac{E_{\text{int}}}{e})^2 \frac{S_Q^{\text{sym}}}{\hbar^2}, \tag{3.58}$$

where S_I^{sym} is the total symmetrized current noise of the S-SET and S_Q^{sym} is the symmetrized spectrum of charge fluctuations on the SET center island. From Eq. 3.52, we have

$$S_I^{\text{sym}} = 4k_B T_{\text{SET}} G_d. \tag{3.59}$$

39

E_{int} describes the interaction between the SET and a coupled device such as QD, and ΔI is the change in the SET current due to the charge motion on the QD. The interaction energy is given by

$$E_{\text{int}} = \frac{e^2 C_c}{C_{\Sigma s} C_{\Sigma d} - C_c^2} \approx \frac{e^2 C_c}{C_{\Sigma s} C_{\Sigma d}}, \quad (3.60)$$

with $C_c \ll C_{\Sigma s}, C_{\Sigma d}$, where $C_{\Sigma s}$ and $C_{\Sigma d}$ are the total capacitance of the S-SET and QD, and C_c is the coupling capacitance. The change in S-SET current due to the motion of a single electron on the dot is given by

$$\Delta I = \frac{\partial I}{\partial n_g} \frac{C_c}{C_{\Sigma d}}. \quad (3.61)$$

Neglecting the noise of the HEMT amplify noise , the intrinsic rms charge sensitivity of the SET is given by [66]

$$(\delta q_i)^2 = \frac{S_I^{\text{sym}}}{(\partial I/\partial n_g)^2}, \quad (3.62)$$

Combing Eq. 3.57, Eq. 3.61, and Eq. 3.62, the measurement time τ_{meas} is given by

$$\tau_{\text{meas}} = 4(\delta q_i)^2 (\frac{C_{\Sigma d}}{C_c})^2 \quad (3.63)$$

A more conservative estimate will be replacing δq_i with δq by accounting for the HEMT amplifier noise.

The analysis for the quantum limit parameter (χ) is different for the SET and the S-SET due to the discrepancy in the evaluation of the charge fluctuation noise.

For an S-SET, in the limit of $E_J \ll \Gamma$, where E_J is the Josephson energy which sets the strength of coherent Cooper-pair tunneling, Γ is the tunneling rate for the quasiparticles, we follow Clark and Bennett's approach [40] and apply the extension of the orthodox theory to the DJQP feature of the S-SET. In general,

$$S_Q^{\text{sym}} = \frac{4e^2 m \gamma_d k_B T_{\text{SET}}}{A^2}, \quad (3.64)$$

where γ_d is the rate at which the SET damps the state of the QD, m is the mass of the resonator and A describes the strength of SSET-QD coupling. Near the DJQP feature of the S-SET, the effective temperature can be represented as

$$k_B T_{\text{SET}} = \frac{(\hbar\Gamma)^2 + 4\delta^2}{32\delta}, \tag{3.65}$$

where δ describes the distance of the S-SET from the DJQP resonance peak. For an S-SET with symmetric tunnel junctions, we also have

$$\frac{m\gamma_d}{A^2} = \frac{2\delta}{E_J^2 \Gamma}. \tag{3.66}$$

Since the Cooper pair tunneling rate is the limiting process in the DJQP cycle, we substitute E_J and Γ with the tunneling rate for Cooper pairs Γ_{CPT} and combine Eq. 3.64, Eq. 3.65, and Eq. 3.66 to yield

$$S_Q^{\text{sym}} = \frac{e^2}{4\Gamma_{\text{CPT}}}. \tag{3.67}$$

The average current is set by 3e times the series addition of two incoherent Cooper-pairs tunneling in the DJQP cycle where 3e is the number of electrons tunneling through each junction. Near the center of the DJQP resonance and for symmetric junctions, the current is approximately given by

$$I \approx \frac{3}{2}e\Gamma_{\text{CPT}}. \tag{3.68}$$

Combining Eq. 3.67 and Eq. 3.68, we can rewrite S_Q^{sym} in the vicinity of the DJQP resonance by

$$S_Q^{\text{sym}} \approx \frac{3}{8}\frac{e^3}{I}. \tag{3.69}$$

In physical terms, the charge noise S_Q^{sym} near DJQP is due to effective telegraph noise between the $n+1$ and n charges states, with the S-SET spending nearly equal time in each for symmetric junctions. From Eq. 3.58, Eq. 3.60, and Eq. 3.69, it leads to our estimate of the dephasing rate for the S-SET,

$$\tau_\varphi^{-1} = \left(\frac{eC_c}{C_{\Sigma s}C_{\Sigma d}}\right)^2 \frac{3e^3}{8I\hbar^2} \tag{3.70}$$

Combining Eq. 3.56, Eq. 3.63 and Eq. 3.70, we get our final expression of χ for an S-SET near the DJQP resonance, which is

$$\chi = \sqrt{\frac{6eE_c^2(\delta q_i)^2}{I\hbar^2}}. \tag{3.71}$$

For a normal SET, there is only quasiparticle tunneling. In this case, we have

$$\frac{2m\gamma_d}{A^2} = \frac{2h}{g(eV_{\text{sd}})^2}, \tag{3.72}$$

where ge^2/h is the conductance of a single junction and $g = 1$ for a typical SET with 50kΩ resistance. On the other hand, for a fixed V_{sd}, the damping rate is constant, T_{SET} is maximum at the point of maximum current and it is given by

$$k_B T_{\text{SET}} = \frac{eV_{\text{sd}}}{4}. \tag{3.73}$$

Substituting Eq. 3.72 and Eq. 3.73 into Eq. 3.64, we then have S_Q^{sym} for a normal SET as

$$S_Q^{\text{sym}} \approx \frac{e^3 R_\Sigma}{2V_{\text{sd}}}. \tag{3.74}$$

Similarly, χ for a normal SET is then given approximately by

$$\chi = \sqrt{\frac{8eE_c^2(\delta q_i)^2 R_\Sigma}{V_{\text{sd}}\hbar^2}}. \tag{3.75}$$

The fact that χ is independent of the specifics of the measured system and its coupling to the S-SET (SET) is to be anticipated: an amplifier's proximity to the quantum limit should be an intrinsic property of the amplifier, and not depend on a particular object. For both S-SET and SET, we have that the charge fluctuations are inversely proportional to the current. At first glance, the formula of χ is similar for SET and S-SET. However, they are actually quite different: the S-SET current I in Eq. 3.71 is due to the resonant phenomenon of Cooper pair tunneling near the DJQP resonance in the subgap region, while

V_{sd}/R_Σ in Eq. 3.75, the current in the SET's high bias region, can be viewed as a rough approximation to the current of an SET just above the threshold. For comparison, the ratio of V_{sd} to R_Σ for an S-SET is less than half of the measured current since both the Cooper pair and quasiparticle contribute to the tunneling.

In conclusion, due to the significantly larger current for the S-SET in the subgap region, the charge fluctuation noise is much lower with the S-SET than SET. Meanwhile, although the evaluation for τ_{meas} is the same for both SET and S-SET, we get a better charge sensitivity and less τ_{meas} for an S-SET in the subgap region. It is clear that an optimized S-SET can operate closer to the quantum limit than an optimized SET.

CHAPTER 4

S-SET IN A HIGH Q ON CHIP MICROWAVE CAVITY

4.1 Circuit quantum electrodynamics

The interaction of matter and light is one of the fundamental processes of nature. The elementary form is realized when a single electron interacts with a single photon. The field of cavity quantum electrodynamics (CQED) explores this area. When one applies this idea to superconducting electrical circuits rather than natural atoms, circuit quantum electrodynamics is introduced (QED). [67,68]

Superconducting circuits consisting of capacitors, inductors and dissipationless Josephson junctions can be engineered to have discrete, non-linear spectra and long coherence time. In circuit QED, a microwave cavity is formed from a transmission line and a superconducting quantum two-level system (qubit) is embedded inside of it. In this architecture, the qubit can be strongly coupled to a single microwave photon.

Since most of the microwave applications fall in the range of 3 and 30GHz, it is unrealistic to design an ideally lumped element circuit such as an on-chip LC resonator. Instead, we use a transmission line resonator as a microwave cavity. The geometry of the transmission line is very simple and easy to simulate. In contrast to the lumped element resonator, the transmission line resonator's voltages and currents vary in phase and magnitude over its length.

4.2 Parallel LCR resonant circuit

Here, we model the one-dimensional transmission line resonator as a lumped element LCR circuit. [38] We begin with a parallel LCR circuit shown in Fig. 4.1(a). The input impedance for the circuit is given by
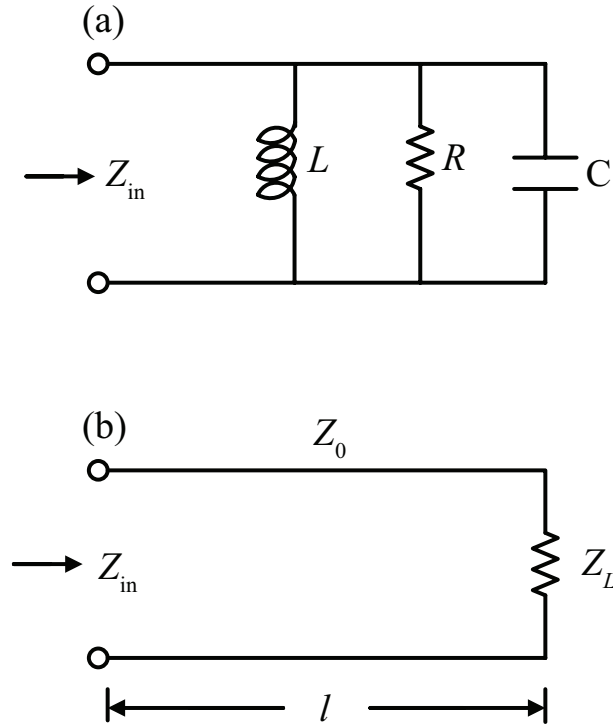
Figure 4.1. (a) Parallel resonant circuit. (b) Transmission line with impedance Z_0 and length l terminated by a load Z_l.

$$Z_{\text{in}} = \left(\frac{1}{R} + \frac{1}{i\omega L} + i\omega C\right)^{-1}. \tag{4.1}$$

At the resonant frequency, we have $\omega_0 = 1/\sqrt{LC}$, and the input impedance $Z_{\text{in}} = R$. Near resonance where $\omega = \omega_0 + \Delta\omega$ and $\Delta\omega/\omega_0 \ll 1$. Taylor expand in $\Delta\omega/\omega_0$ to first order and we have

$$Z_{\text{in}} \approx \frac{R}{1 + 2iQ\Delta\omega/\omega}, \tag{4.2}$$

where $Q = \omega_0 RC$ is the quality factor of the resonant circuit. It is obvious from Eq. 4.2, that the input impedance is peaked at resonance, and its maximum value is given by R.

A transmission line of impedance Z_0 and length l terminated by a load Z_L is shown in Fig. 4.1(b). The input impedance of such a transmission line is given by

$$Z_{\text{in}} = Z_0 \frac{Z_L + Z_0 \tanh \gamma l}{Z_0 + Z_L \tanh \gamma l}, \tag{4.3}$$

where $\gamma = \alpha + i\beta$. Here α characterizes the losses in the transmission line and $\beta = 2\pi/\lambda$ is the propagation constant.

In general, we are interested in resonators consisting of a section of transmission line of length l that is coupled by small capacitors to the macroscopic world. Usually, the capacitors are small and for a first treatment we can assume that the transmission line is terminated by an open circuit ($Z_L = \infty$). In this case, Z_{in} becomes

$$Z_{\text{in}} = Z_0 \coth \gamma l = Z_0 \frac{1 + i \tan \beta l \tanh \alpha l}{\tanh \alpha l + i \tan \beta l}. \tag{4.4}$$

Considering a transmission line with a full wavelength at ω_0, we have the length $l = \lambda = 2\pi v_{\text{ph}}/\omega_0$, where $v_{\text{ph}} = 1/\sqrt{L_l C_l}$ is the phase velocity, L_l and C_l are the inductance and capacitance per unit length of the transmission line.

Near resonance, we have

$$\beta l = \frac{\omega l}{v_{\text{ph}}} = \frac{\omega_0 l + \Delta \omega l}{v_{\text{ph}}} = 2\pi + \frac{2\pi \Delta \omega}{\omega_0} \tag{4.5}$$

and

$$\tan \beta l = \tan 2\pi \frac{\Delta \omega}{\omega_0} \approx 2\pi \frac{\Delta \omega}{\omega_0}. \tag{4.6}$$

For a low-loss line near resonance, $\alpha l \ll 1$, and we can rewrite Eq. 4.4 as

$$Z_{\text{in}} \approx \frac{Z_0}{\alpha l + i\beta l} = \frac{Z_0/\alpha l}{1 + 2i(\frac{\pi}{\omega_0 Z_0})(\frac{Z_0}{\alpha l})\Delta \omega}. \tag{4.7}$$

Comparing this equation with Eq. 4.2, we see that the open-circuited full-wave transmission line resonator can be treated as a parallel resonant circuit for which

$$C = \frac{\pi}{\omega_0 Z_0}, \tag{4.8}$$

$$R = \frac{Z_0}{\alpha l}, \tag{4.9}$$

and

$$Q = \frac{\pi}{\alpha l}. \tag{4.10}$$

Using the relationship $\omega_0 = \frac{2\pi}{l\sqrt{L_l C_l}}$, one can express L and C in terms of L_l and C_l as

$$C = \frac{C_l l}{2}, \tag{4.11}$$

and

$$L = \frac{L_l l}{2\pi^2}. \tag{4.12}$$

The LCR model of the transmission line resonator gives one a simple picture of the resonator properties. The input impedance should be strongly peaked near resonance, with a maximum value given by $Z_0/\alpha l$ and bandwidth $\omega_0 \alpha l/\pi$.

4.3   Capacitively coupled transmission line resonator

The advantage of the LCR model is that it simplifies the analysis of coupling the resonator to input and output lines. When the transmission line resonator is coupled to the macroscopic world with some coupling capacitance, we must consider its loaded Q_L. For quantum measurements, a high loaded quality factor Q_L is required. Here Q_L is controlled by capacitive coupling to the input and output lines and is given by [69,70]

$$\frac{1}{Q_L} = \frac{1}{Q_{\text{int}}} + \frac{1}{Q_{\text{ext}}}, \tag{4.13}$$

where the internal quality factor $Q_{\text{int}} = \omega_0 RC = \pi/\alpha l$, and the external quality factor is given by

$$Q_{\text{ext}} = \omega_0 R_{\text{ext}} C_{\text{ext}}, \tag{4.14}$$

with

$$R_{\text{ext}} = \frac{1 + Z_0^2 C_\kappa^2 \omega_0^2}{2 Z_0 C_\kappa^2 \omega_0^2} \quad \text{and} \quad C_{\text{ext}} = \frac{C_\kappa}{1 + Z_0^2 C_\kappa^2 \omega_0^2} \tag{4.15}$$

where C_κ is the coupling capacitance to the macroscopic world.

Depending on C_κ, there are two regimes for capacitive coupling of the resonator. When C_κ is small, $Q_L \approx Q_{\text{int}}$, and the resonator is undercoupled. In this regime, Q_L saturates at the internal quality factor, which is determined by the intrinsic losses of the resonator. The resonator can be used to store photons on a long time scale. When C_κ is relatively large,

$Q_L \approx Q_{\text{ext}}$, and the resonator is overcoupled. In this regime, it is possible to engineer the Q_L for fast measurements of a qubit state.

4.4   Coplanar waveguide resonator

Superconducting coplanar waveguide (CPW) resonators have a wide range of applications such as radiation detectors in the optical, UV and X-ray frequency ranges, and in quantum information and quantum optics experiments. It is an ideal candidate for a physical realization of the transmission line resonator. The CPW ground lies in the same plane as the center conductor, which is ideal for our wire bond and surface mount components. Also, as a standard technique in microwave engineering, one can adjust the lateral scale of the center conductors and gaps while keeping the impedance unchanged.
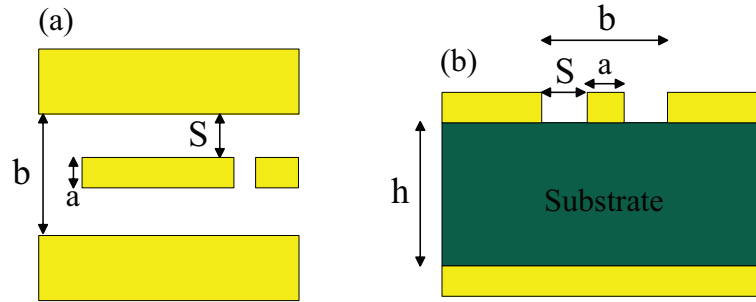
Figure 4.2. Sketch of a coplanar waveguide with a well defined ground.

As shown in the Fig. 4.2, the resonant frequency f_0 of a full-wave CPW is given by [41]

$$f_0 = \frac{c}{\lambda_0 \sqrt{\epsilon_{\text{eff}}}} = \frac{c}{l \sqrt{\epsilon_{\text{eff}}}}. \tag{4.16}$$

Here, the effective permittivity ϵ_{eff} and the impedance of the CPW depend on the geometry. They are given by:

$$\epsilon_{\text{eff}} = \frac{1 + \epsilon_r \tilde{K}}{1 + \tilde{K}} \tag{4.17}$$

and

$$Z_0 = \frac{60\pi}{\sqrt{\epsilon_{\text{eff}}}} \left(\frac{K(k)}{K(k')} + \frac{K(k_1)}{K(k_1')} \right)^{-1}, \tag{4.18}$$

where K is the complete elliptic integral of the first kind,

$$k = a/b, \tag{4.19}$$

$$k' = \sqrt{1 - k^2}, \tag{4.20}$$

$$k_1 = \frac{\tanh(\frac{\pi a}{4h})}{\tanh(\frac{\pi b}{4h})}, \tag{4.21}$$

$$k_1' = \sqrt{1 - k_1^2}, \tag{4.22}$$

$$\tilde{K} = \frac{K(k')K(k_1)}{K(k)K(k_1')}, \tag{4.23}$$

and ϵ_r is the relative dielectric constant of the substrate with height h. Here a is the width of the center conductor, s is the gap width, and $b = 2s + a$. The ground plane should extend more than $5b$ on each side of the gap for reasonable coplanar wave guide analysis. C_l and L_l are given by

$$L_l = \frac{\mu_0}{4} \frac{K(k')}{K(k)}, \tag{4.24}$$

and

$$C_l = 4\epsilon_0 \epsilon_{\text{eff}} \frac{K(k)}{K(k')}. \tag{4.25}$$

For our current CPW design, $a = 10\mu$m, $s = 4\mu$m, $b = 18\mu$m, and $\epsilon_{\text{eff}} = 5.05$, giving $C_l = 1.5 \times 10^{-10}$F/m, $C = 2$pF, $L_l = 3.76 \times 10^{-7}$H/m, $L = 0.5$nH and $\lambda = 26.7$mm.

4.5 Introduction of a DC bias into a high Q microwave cavity

This section introduces a new waveguide design in order to introduce a DC voltage or current bias into a transmission line without significantly disturbing the cavity modes or degrading its quality factor. [5] The DC biasing scheme is shown in Fig. 4.3. Two sections of $\lambda/2$-long transmission lines that form two bias "T" junctions are added to the original main full-wave resonator at points (red dots) a distance $\lambda/4$ away from either end. These points are located at the voltage nodes (current antinodes) and are the low impedance points on the line. The DC voltage or current source is then applied via spiral inductors attached to the $\lambda/2$ transmission line. An S-SET will be located at the high-impedance point (black dot) at the center of the resonator.
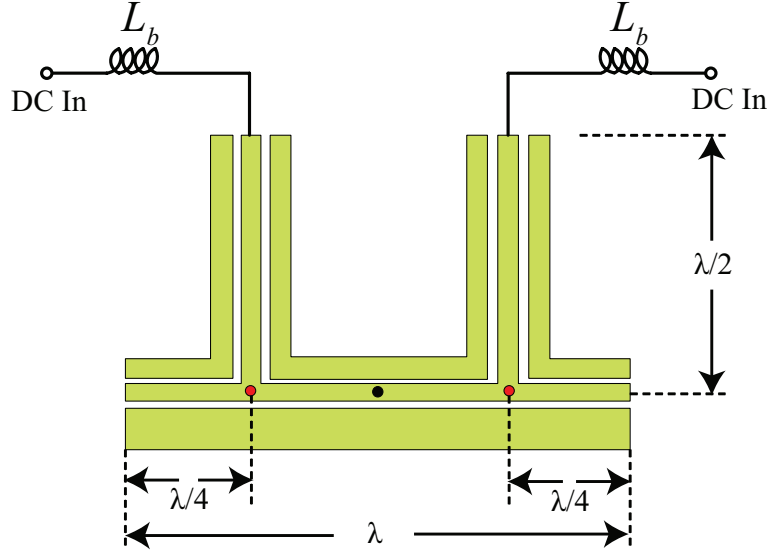
Figure 4.3. Scheme for introducing a dc bias into a high-Q microwave cavity of length λ. The bias is introduced via inductor L attached via $\lambda/2$ lengths of transmission to the two low-impedance points (red dots) on the main resonator. An S-SET would be located at the high impedance point (black dot) at the center of the resonator.

To simplify analysis, we first assume the transmission line is almost lossless. From Eq. 4.7 and for an attenuation constant $\alpha = 0$, the input impedance of a lossless transmission line terminated in an open circuit is given by

$$Z_{\text{in}} = Z_0 \coth i\beta l = -iZ_0 \coth \beta l. \tag{4.26}$$

If the length of the line is either $\lambda/4$ or $3\lambda/4$, $Z_{\text{in}} = 0$. At one of these low impedance points, looking at either end of the transmission line, it is a short. In order to maintain the conditions after adding the dc feedline, the impedance of the dc feedline at the low-impedance point should be as large as possible. To achieve this, we use a $\lambda/2$ length of transmission line terminated in a spiral inductor. The impedance of a lossless transmission line terminated in a load Z_L is given by

$$Z_{\text{in}} = Z_0 \frac{Z_L + iZ_0 \tan \beta l}{Z_0 + iZ_L \tan \beta l}. \tag{4.27}$$

When $l = \lambda/2$, $Z_{\text{in}} = Z_L$, indicating that a half-wave line does not change the load impedance. At one of the bias "T" junctions, neglecting the other section of half-wave

50

line and looking toward either end of the main line, one sees a short in parallel with the inductor impedance $Z_L = i\omega L$. Therefore, the total impedance is not changed by adding the DC feedline and the cavity should remain unchanged.

4.6 S-SET in circuit QED architecture
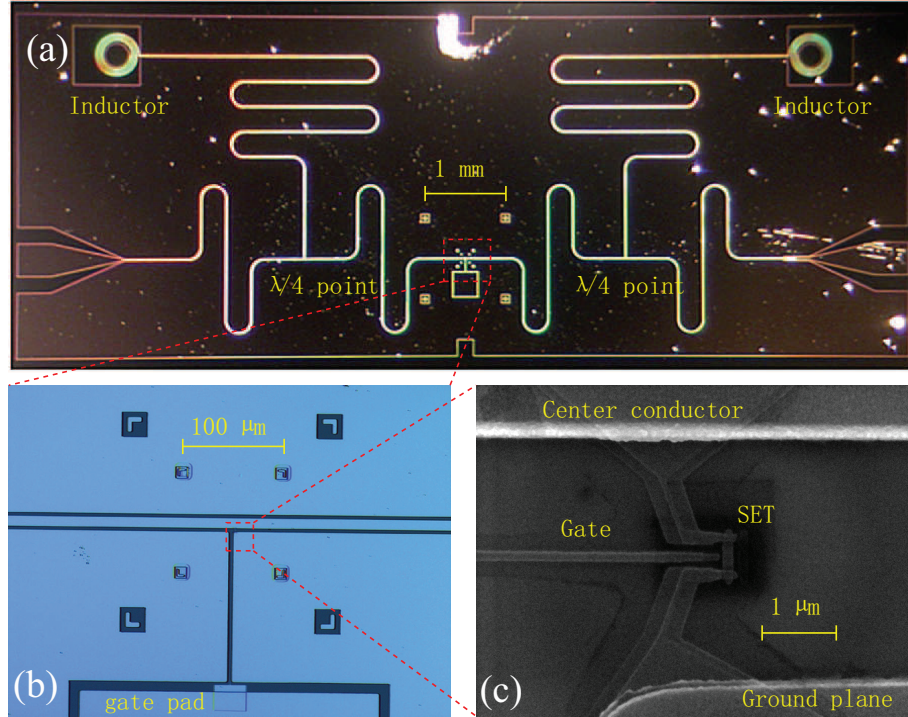
Figure 4.4. (a) Optical image of a 5GHz coplanar waveguide resonator with DC bias introduced. (b) The magnified region indicates the place S-SET is located. (c) Scanning electron micrograph of an S-SET.

We embed the S-SET in a full-wavelength coplanar wave guide cavity with the introduction of the DC bias as shown in Fig. 4.4. The S-SET is located at the center of the resonator with its source connecting to center conductor line and drain connecting to the ground plane of the CPW.

A simplified classical model of the cavity-SSET system is illustrated in Fig. 4.5 with the S-SET biased in the vicinity of zero bias. [71] We assume the S-SET only interacts with one mode of the cavity and that all other modes and their coupling to the environment can be modeled as a resistance. We still treat CPW as a parallel LCR, assuming the double
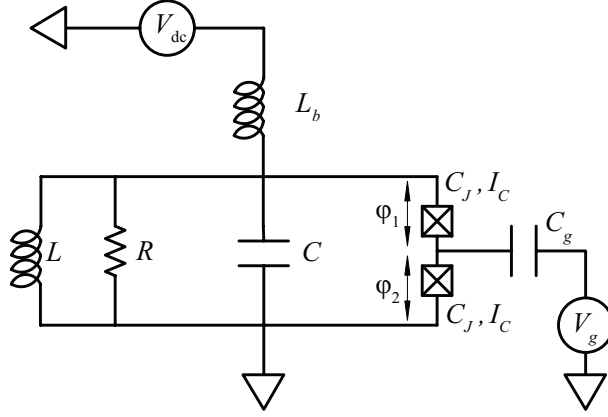
Figure 4.5. Model of cavity-SSET system.

junctions of the S-SET are symmetric and have the same critical current I_c and capacitance C_J. The model assumes that the spiral inductor L_b is a few tens of nH, the inductance of the main waveguide line L is a few nH, capacitance of CPW C is a few pF, the capacitance of Josephson junction C_J is a few hundred aF and the capacitance of gate coupling $C_g \sim$ 10 aF. These values satisfy the relations $L_b \gg L$ and $C \gg C_J \gg C_g$.

From Kirchoff's law, we have [71]

$$\ddot{\tilde{\gamma}}_+ + Q^{-1}\dot{\tilde{\gamma}}_+ + \tilde{\gamma}_+ = F_0 \sin(\omega_d\tilde{\tau} + \tilde{\gamma}_+) \cos\gamma_- \tag{4.28}$$

and

$$\eta_J\ddot{\tilde{\gamma}}_- = F_0 \sin\gamma_- \cos(\omega_d\tilde{\tau} + \tilde{\gamma}_+) - \eta_g\dot{\tilde{V}}_g. \tag{4.29}$$

Here $\gamma_\pm = (\varphi_1 \pm \varphi_2)/2$, φ_1 and φ_2 are the phases across Josephson junctions, Q is the quality factor, the dimensionless force amplitude is

$$F_0 = \pi\frac{2LI_c}{\Phi_0}, \tag{4.30}$$

and the dimensionless driving frequency is

$$\omega_d = \frac{L}{L_b}\frac{2eV_{\text{dc}}}{\hbar\omega_0}. \tag{4.31}$$

Also, $\eta_J = C_J/C, \eta_g = C_g/C$, and $\tilde{V}_g = eV_g/\hbar\omega_0$. For small force amplitude and driving frequency close to the LHS oscillator frequency, $\omega_d \sim 1$, Eq. 4.28 acts like a driven, damped

harmonic oscillator. Plugging in the parameters of our CPW design, for $V_{\text{dc}} = 50\mu$V, the spiral inductor should be around 3nH. Eq. 4.29 describes the internal phase fluctuation of the S-SET. For typical force amplitude $F_0 \sim 0.1$ and a high Q, we have $F_0 Q \gg 1$ and the system is strongly nonlinear.

CHAPTER 5

EXPERIMENTAL TECHNIQUES

This chapter briefly reviews some sample fabrication techniques, fridge setup, sample wiring, CPW sample box design and RF-SET measurement techniques.

5.1   Fabrication techniques

Two general methods of patterning mesoscopic devices are photolithography and electron beam (e-beam) lithography, with resolution of several μm and a few tens of nm, respectively. Due to their difference in resolution, we use e-beam lithography for the on-chip matching network and both methods for the SET-high Q cavity. For the first step, the CPW is fabricated by photolithography with minimum feature size of about 5μm. An SET is then fabricated in the center of the CPW by e-beam lithography.

Photolithography

The technique of photolithography remains critical in the semiconductor industry. It is a process of using UV light to transfer geometric shapes on a mask to the surface of a semiconductor wafer. In general, it involves five steps: (1) coat a sample with photoresist and bake it; (2) expose the resist to UV radiation; (3) develop the pattern; (4) remove the unexposed part; (5) lift off the resist; and (6) deposit metal. A typical sequence of steps for producing a 5GHz CPW is as follows:

1. Cleave a 1.5cm $\times$ 1cm piece of Si from the wafer.

2. Sonicate the samples in Acetone for 3min, Methanol for 1min and DI water for 1min.

3. Blow dry with N_2 gas and bake at 115^0C for 2 min.

4. Spin LOR5A at 4000 rpm for 1 min.

5. Bake at 195^0C for 10 min.

6. Spin S1813 at 4000 rpm for 1 min.

7. Bake at 115^0C for 2 min.

8. Expose in hard contact mode for 12s.

9. Develop in MF-319 for 120s.

10. Postbake at 115^0C for 2 min.

11. Reactive Ion Etching (RIE) descumming at 100mT, 25W for 1min. (O_2 flow rate ≈ 13 sccm).

12. E-beam evaporate 200nm Al with deposition rate ≈ 0.5nm/s.

13. Lift-off in N-Methyl-2-pyrrolidone (NMP) and followed by ultrasonic agitation.

The CPW structure is generated by exposing a bilayer positive photoresist (600nm LOR5A and 1.2μm S1813) through a mask with photolithography. The bonds of molecules for a positive resist are broken easily with UV light and then removed by the developer, MF-319. We put the lower sensitivity resist (S1813) as the upper layer and the higher sensitivity resist (LOR5A) as the lower layer. In this geometry, we can obtain an undercut with the shape of the pattern determined by the upper layer.

Fig. 5.1 illustrates the simplified schematic diagram of the photolithography steps with bi-layer photoresist. This method avoids the direct contact of metal and the photoresist and makes the liftoff process much easier.

Reactive ion etching (RIE)

Reactive ion etching (RIE) is an etching technology widely used in microfabrication. It involves the introduction of gas in an electric field to form a plasma whose constituent ions react with the material to be removed. Different gases and operating parameters are set for different materials. We use it to break down any resist residue left after development and leave the unexposed resist intact. When operating the RIE, we run it twice. The first run
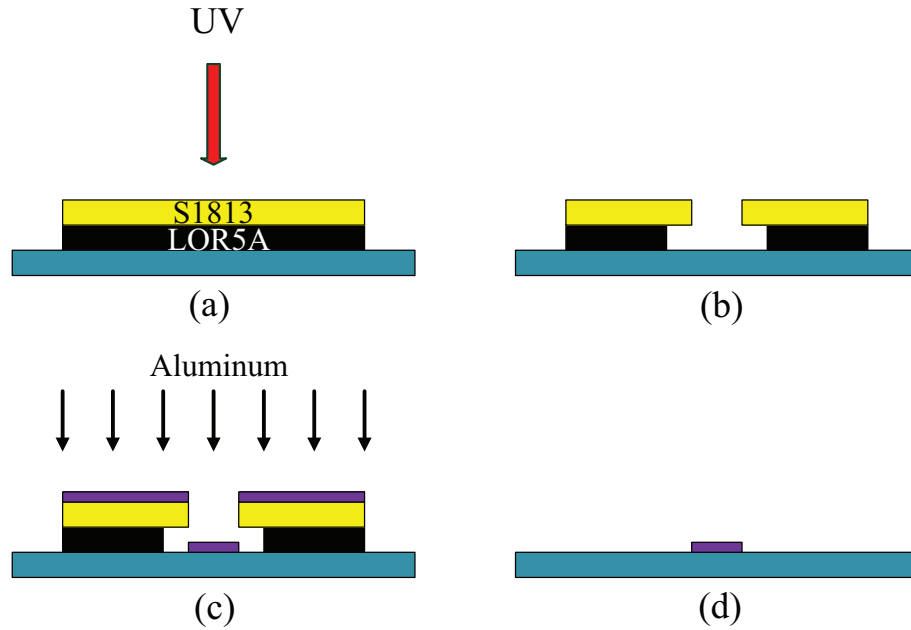
Figure 5.1. Schematic diagram of the bi-layer photolithography process.

is to calibrate the system for the resist descumming, the second run is for the real sample. Generally, each RIE procedure involves five steps: (1) put the sample in the chamber and evacuate the chamber; (2) turn on the gas flow; (3) wait for gas pressure to stabilize; (4) expose the sample; and (5) take out the sample after venting the chamber.

E-beam lithography

E-beam lithography is widely used as a standard technique for device fabrication in nanotechnology and integrated circuits. Different from photolithography, e-beam lithography involves scanning a beam of electrons in a predesigned pattern across the surface of the semiconductor wafer covered with e-beam resist. This technique beats the diffraction limit of light for photolithography and allows fabrication of structures on nanometer scales.

The e-beam lithography utilized in this research involves using special software (NPGS and Design CAD2000) and hardware attached to a commercial SEM. Fig. 5.2 shows a simplified schematic of a SEM/NPGS system. We draw the pattern in Design CAD2000 and generate the run file in NPGS. The commands are set in the run file for controlling the electron beam to write on a designed pattern.
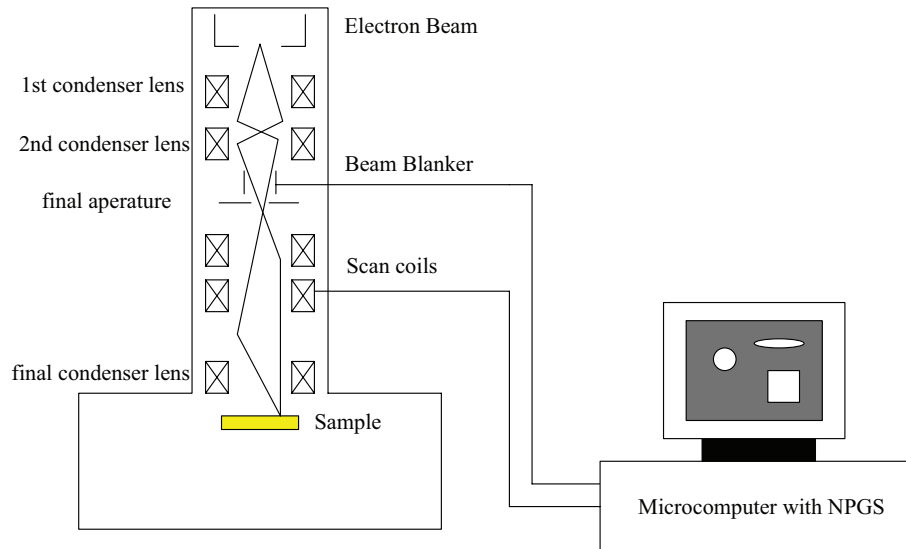
Figure 5.2. A schematic of electron-beam lithography system.

At Dartmouth College, we use a FEI XL-30 ESEM for e-beam lithography. The resolution of the system is around 20nm. For fabricating the SET, a positive resist is used. A large undercut generated by a bi-layer e-beam resist enables us to use shadow evaporation to fabricate the SET.

Alignment

As shown in Fig. 4.4, our design requires accurate positioning of the SET. Misplacement of 2μm will connect the SET and the gate to the ground plane of the CPW. When drawing the SET by e-beam lithography, it is not practical to scan at the center of the waveguide to determine the correct position since overexposure will damage the e-beam resist. An alternative method is to draw several alignment marks and use them to identify the center of the CPW. On the waveguide photomask, we added three pairs of alignment marks with different magnifications around the center. Each pair has four marks at four corners. We also constructed the same patterns in Design CAD2000 and generate the NPGS run file. After we have identified the center, we run the NPGS file for the largest pair of alignment marks first. This exposes the alignment marks region only. We then move the sample's stage to adjust the position of the real marks made by photolithography to overlap the alignment marks drawn with NPGS without exposing of the center region of the CPW, as
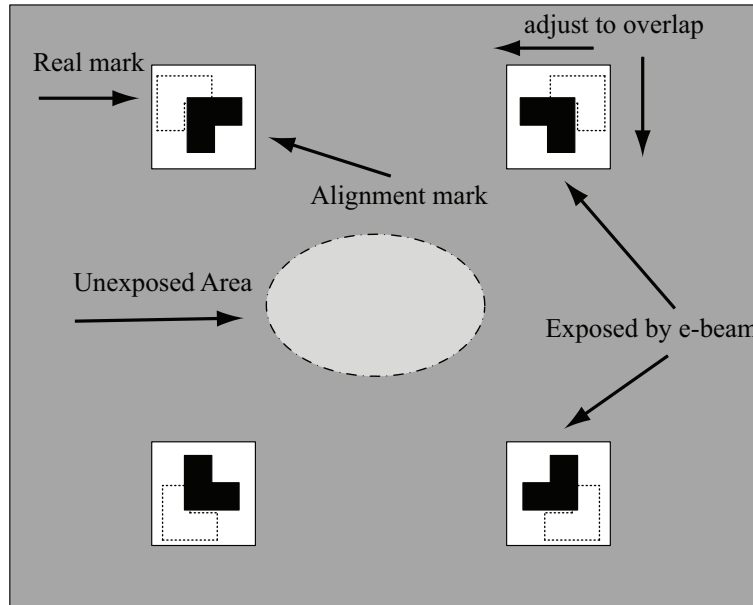
Figure 5.3. Schematic drawing of the alignment process. Only the white areas in the windows are exposed in this process.

illustrated in Fig. 5.3. After obtaining good overlap, we choose a smaller pair of alignment marks and follow the same procedure for a more accurate alignment.

Evaporation

Shadow evaporation is the most widely used technique for fabricating an SET out of Al/AlO$_x$/Al films. As illustrated in Fig. 5.4, the idea is to evaporate the same pattern twice with aluminum by tilting the sample mount at different angles and oxidizing the aluminum between these two evaporations. After the evaporation, part of the shadows will overlap, with an oxygen layer between the two to form the two ultra-small tunnel junctions of the SET. The oxide thickness is controlled by adjusting the oxygen pressure and oxidization time.

Experimentally, we evaporated twice with aluminum for the S-SET/LC resonator for the following reasons. For the resonator, shadow evaporation and oxidization should be avoided. Also, using an ultra thin aluminum film lead to issues with skin effect and kinetic inductance; the spiral inductor should be made thicker than the film of the SET. Empirically,
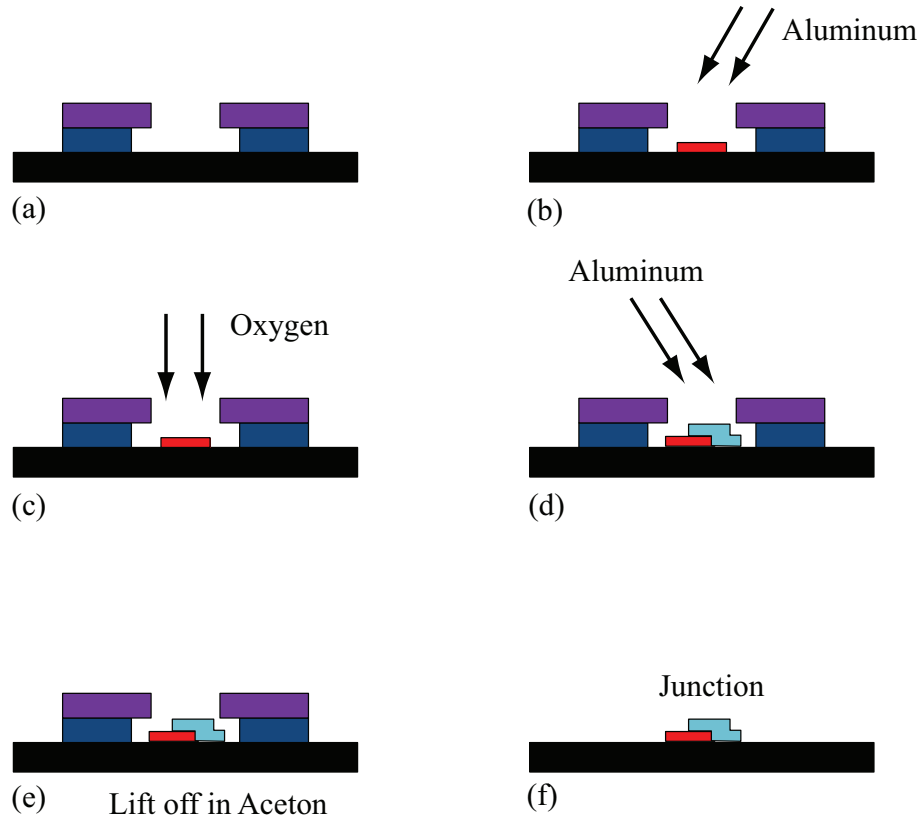
Figure 5.4. Schematic illustration of double angle shadow evaporation.

a 50nm film is required for the spiral inductor. Experimentally, we use the aluminum foil to cover the SET (spiral inductor) when evaporate the spiral inductor (SET).

The shadow evaporation is implemented in our thermal evaporator. The standard thermal evaporation technique consists of heating a tungsten boat or basket loaded with material to be deposited. The material vapor condenses in the form of ultra thin film on the cold substrate and the vacuum chamber. The evaporation is done at low pressure in the rage of 10^{-6} Torr or lower to avoid a reaction between vapor and atmosphere.

In order to deposit a thick film (120 nm) required for the CPW, we use an e-beam evaporator instead of the thermal one due to its efficiency and larger deposition capacity. Unlike the thermal evaporator in which the source is melted by conduction from a resistive heater, an e-beam evaporator exposes the source material to a beam of electrons that directly heat it by irradiation. An e-beam evaporator can generate a higher and more stable evaporation rate than can a thermal evaporator.

5.2 SET fabrication improvements

The physical size of the SET makes the fabrication a challenge, particularly for an SET with a good charge sensitivity.

Burn hole technique
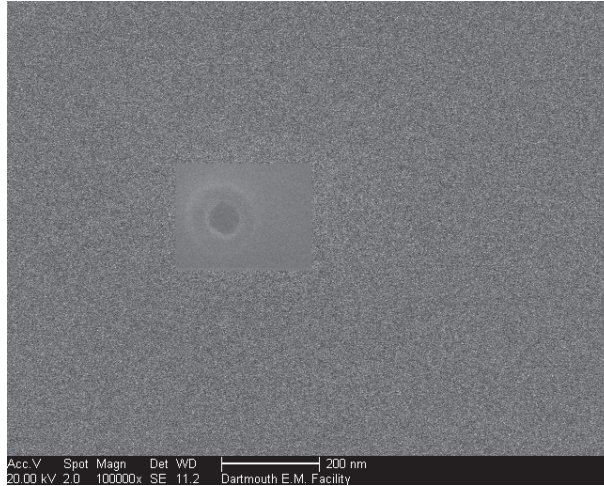
Figure 5.5. Scanning electron micrograph of a typical burning hole.

A typical junction size for the SETs we make is approximately $40 \times 60 \text{nm}^2$, which approaches the resolution of the FEI XL-30 and makes the yield a major concern. Empirically, we find a good e-beam focus on the substrate is critical. In order to improve it, we put silver paint at the edge of the wafer and focus on it first, then we move the e-beam very close (usually 100μm) to the place for drawing the SET. We turn on the beam, set a very large beam current (≈ 5nA) to the spot size mode and expose the resist for 15 seconds. The result is a visible hole in the remainder of the burned resist as shown in Fig. 5.5. We focus on the hole with a very large magnification to avoid overexposure a larger area. A clear image of the hole usually indicates a good focus on the region where the SET is located.

Evaporation and oxidation

In general, we can improve the S-SET's charge sensitivity by adjusting: (1) the S-SET junction resistance; (2) the charging energy of the S-SET; and (3) the superconducting gap of the S-SET. Usually, a lower junction resistance allows higher order tunneling events

and generates a larger gate modulation current in the sub-gap region. A larger current will produce a measurable intrinsic noise from the SET. Experimentally, the resistance is lowered by either reducing the oxidation pressure and time or by fabricating larger tunnel junctions. We can also increase the current in the sub-gap region by increasing the superconducting gap
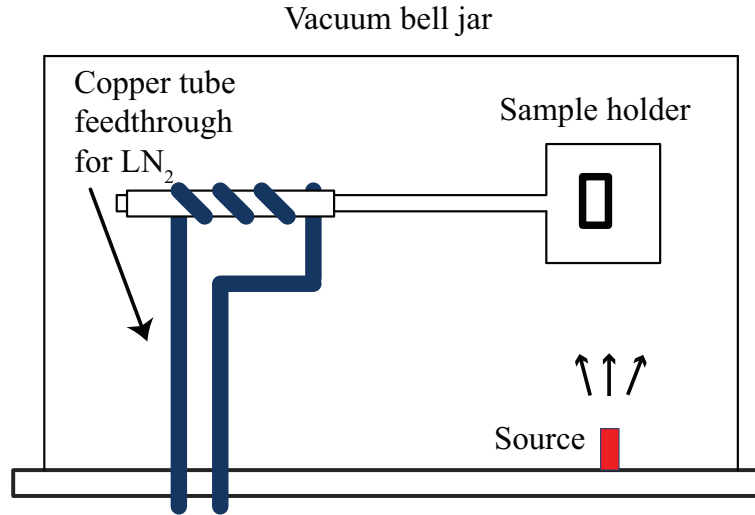
Figure 5.6. Liquid nitrogen cooled sample holder of a thermal evaporator.

of the S-SET. To do so, we tried both pure oxygen doping [72] and thin film evaporation using a liquid nitrogen cold stage. [74,75] For oxygen doping, the pressure required to increase the gap size noticeably was so high (10^{-5}mbar) that the resulting aluminum films had a high resistance. Even worse, the results were not very consistent. An alternative method is to add a liquid nitrogen cold stage to the thermal evaporator. We reduced the Al film thickness from 20nm to 7nm, which increased the gap size by 20% in a reproducible fashion. Fig. 5.6 shows the design of the liquid-nitrogen-cooled sample holder for the thermal evaporator. The copper liquid nitrogen feedline goes into the bell jar through a vacuum feedthrough. Part of the copper liquid nitrogen tube is twisted into a spiral and firmly soldered to the sample holder for a good thermal contact. Each time before evaporation, we turned on the liquid nitrogen flow and controlled its speed. After 20 minutes, the sample holder was cooled to a very low temperature. When the evaporation is finished, we vent the bell jar partially with N_2 and wait about 20 minutes to warm up the the cooled stage to avoid water vapor accumulating on the sample and the bell jar.

5.3 Cryogenic

The on-chip matching network measurements were implemented in an Oxford Heliox ACV pulse tube cooler and a ^{3}He fridge at around 300mK. The circuit QED measurements will be implemented in an Oxford Kelvinox 100 dilution refrigerator with base temperature around 20mK.
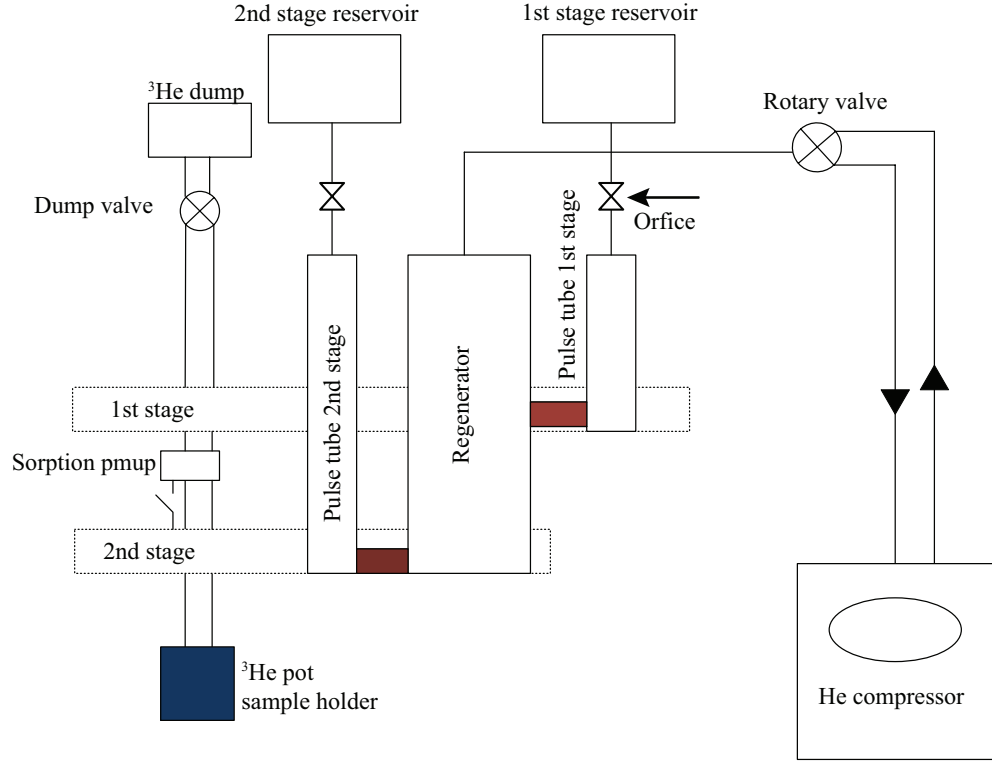
Figure 5.7. Simplified schematic diagram of Oxford Heliox-ACV refrigerator.

Heliox ACV refrigerator

The Heliox ACV refrigerator combines a two stage pulse tube cryocooler (PTC) with a ^{3}He insert. A base temperature at around 300mK makes it useful for many mesoscopic applications. Unlike the dilution refrigerator, the Heliox ACV does not consume any liquid helium and is also easy to operate and maintain. In our lab, we found this to be an useful tool to pre-screen LC resonators and QDs.

The PTC stages provide the main cooling power. With the two PTCs working together, the Heliox ACV can be cooled down to around 2.5K. At this temperature, pressurized ^{3}He in the closed system is liquified. By evaporating liquid ^{3}He with an absorption pump, base

temperature is reached. For more operational details of Heliox ACV refrigerator, please see Timothy Gilheart's thesis. [73]

The refrigerator will keep the base temperature for about 60 hours until all liquid ^{3}He is evaporated. The warmed system can be recovered by the ^{3}He gas in about 2 hours.

Oxford Kelvinox 100

Dilution refrigerators are widely used for ultra low temperature experiments. Its refrigeration process uses a mixture of two isotopes of He, ^{3}He and ^{4}He, to reach temperatures as low as 5mK.
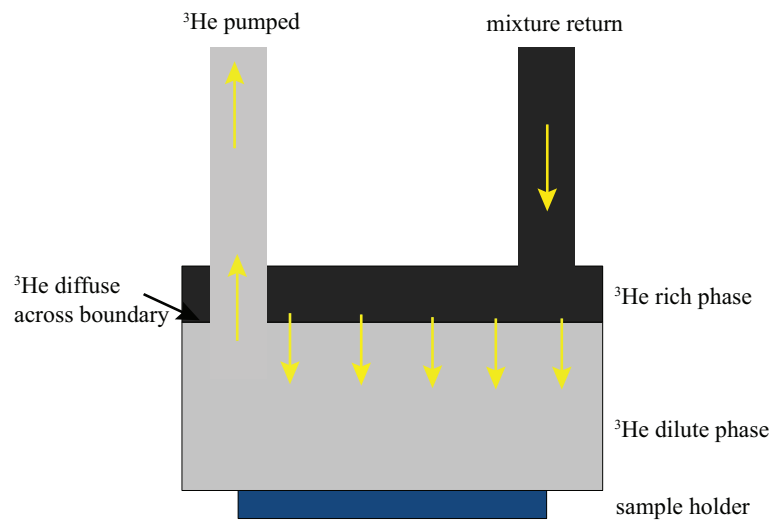
Figure 5.8. A ^{3}He/^{4}He mixture separates into two phases at low temperatures. Pumping on the ^{3}He dilute phase induces ^{3}He to diffuse across the phase boundary to cool the sample.

If we cool any ^{3}He/^{4}He mixture with more than 6% ^{3}He concentration to a very low temperature, the mixture will separate into two phases. The lighter phase is almost pure ^{3}He and is regarded as the concentrated phase. The heavier phase is rich in ^{4}He, and is regarded as the dilute phase, having 6% of ^{3}He even when approaching absolute zero temperature. Fig. 5.8 shows the separation of concentrated and dilute phase. When one pumps on the dilution phase, the ^{3}He is removed and the balance in the dilute phase is broken. This causes the ^{3}He in the concentrated phase to diffuse into the dilute phase. Latent heat is removed in this process and the sample holder attached to the phase mixture will be cooled

down. ^{3}He pumped from the dilute phase is returned to the dilution refrigerator via the condenser. The whole process can run continuously until the base temperature is reached around 15mK for our Kelvinox 100.
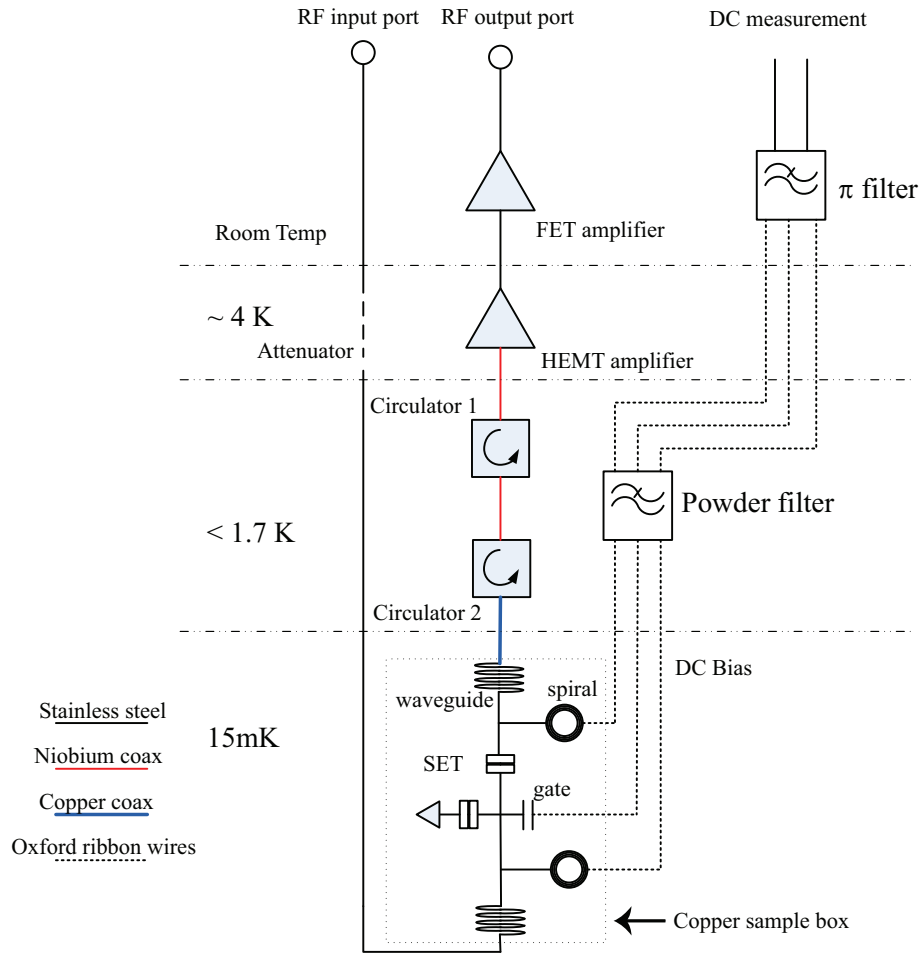
Figure 5.9. Cabling of Oxford Kelvinox 100 Dilution Refrigerator.

5.4   Cable setup

We modified our cable setup of Kelvinox 100 to implement the transmission measurement of the CPW. As shown in Fig. 5.9, the RF input line connects directly to one end of the CPW RF line. Attenuators are attached to the input line to adjust the amplitude of the input carrier wave and filter out noise. On the output line, we installed a high electron mobility transistor (HEMT) with a noise temperature about 7K at a very low temperature. Two circulators are installed between the HEMT amplifier and the CPW. These provide

protection for the HEMT and reduce noise injected from the HEMT into the CPW. The HEMT output is fed to a Lucix room temperature amplifier for further amplification. The Cu powder filter and π filter are installed in the DC lines to eliminate high frequency noise. The input RF transmission line is made by semi-rigid stainless steel coaxial cable which has the lowest thermal conductivity to cut the thermal link between different stages. The output RF line, specifically the lines from circulator to the HEMT are made by superconducting niobium cables. It has negligible loss and zero heat conductance below 9K and guarantees the minimum loss of the intrinsic noise from the S-SET and minimum thermal link. The cable from the CPW to the circulator is made by semi-rigid copper coax for the purpose of low-loss.
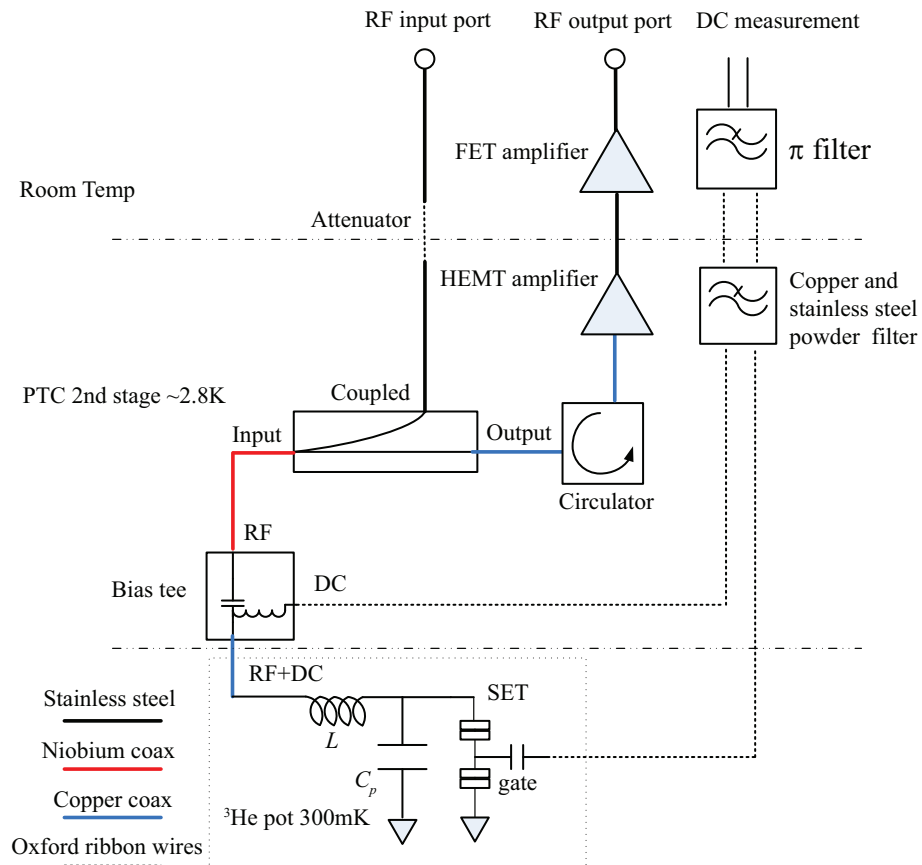
Figure 5.10. Cabling of Oxford Heliox ACV ^{3}He Refrigerator.

The reflection measurement setup on Heliox ACV is useful for measurements of on-chip superconducting matching networks as illustrated in Fig. 5.10. A directional coupler is

installed on the second PTC stage to change the direction of the RF signal and separate the input and output RF lines. A bias tee is added to isolate the DC and RF lines for the purpose of applying DC and RF signal to the LC resonator simultaneously. The HEMT, circulator and directional coupler are installed on the second stage PTC, which has a larger cooling power than ^{3}He pot. Since the ^{3}He pot has very limited cooling power, an ultra thin copper shield with a low thermal mass is made to eliminate microwave radiation to the sample.
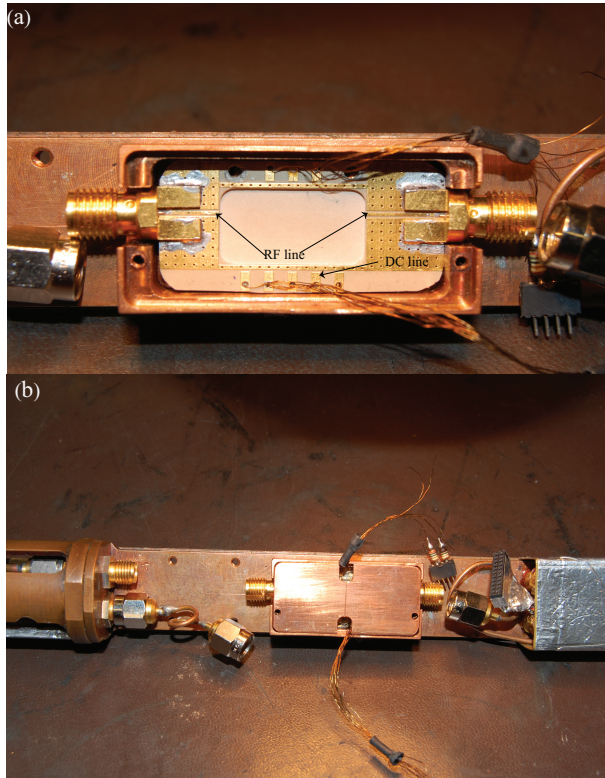
Figure 5.11. Copper box design for the coplanar waveguide.

5.5 CPW sample box design

In order to carry out the CPW measurements at 5GHz, we designed a copper box for reducing microwave radiation. As demonstrated in Fig. 5.11, the waveguide is mounted on a PCB board. The PCB board designed to have a well-defined ground plane and 7 DC, 2 RF lines. The DC lines are for the gate and source drain of the S-SET. We put 2K and 10K resistors on the DC gate line and source drain line respectively to protect the SET from
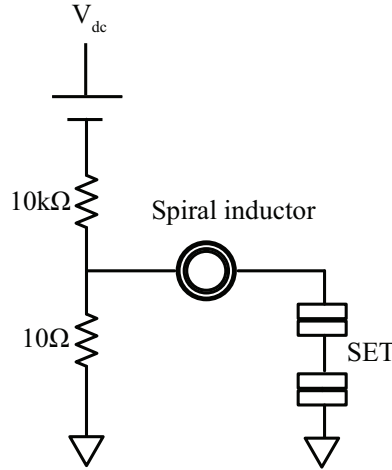
Figure 5.12. Schematic diagram of DC bias line.

electro static discharge. Fig. 5.12 shows the schematic diagram for the DC bias line. A
10Ω surface mount resistor is soldered on the PCB board and wire bonded to the DC line.
The two resistors serve as a voltage divider to easily allow application of small voltages to
the SET. The PCB board is mounted firmly in the copper box with screws to provide a
good thermal contact. The copper box is then attached firmly to the sample mount with
screws. The size of the box is designed to fit the sample mount. More importantly, the
self-resonance of the box, which depends on its size, is far from CPW's resonant frequency
of 5GHz. Two side holes are for the SMA connectors and small holes on the top cover are
the feedthroughs for DC lines. After wire bonding from the CPW to the PCB, we screw
the PCB to the box and cover the box with screws, shield the box with aluminum tape and
mount it to the dilution refrigerator.

5.6   SET characterization

In this section, both DC and RF measurements are briefly introduced. For the DC
component, we measured the SET current I and the differential conductance G_d versus
source drain bias V_{sd} and offset charge V_g. We also introduce a method for improving the
measurement of G_d. For RF measurement, we introduce a method of identifying f_0 for the

resonator and the charge sensitivity measurement of the RF-SET.

DC SET measurement
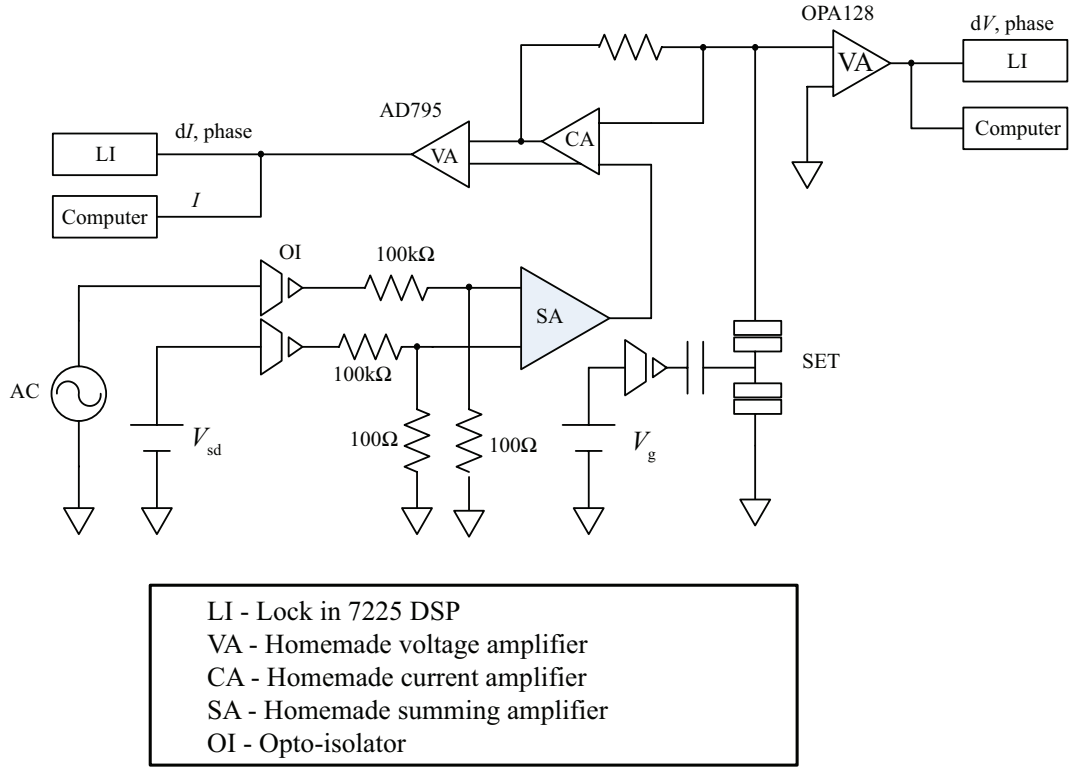
Figure 5.13. Schematic diagram of DC measurement of the SET.

The SET current in the sub-gap region is around several nA, which requires high precision measurement electronics. In our lab, we made our own high gain, low noise current and voltage amplifiers. The DC offset is provided by a homemade voltage reference. All the homemade electronics are battery powered to reduce the noise from AC power supply. For the differential conductance measurement, we use the Signal Recovery 7225DSP lock in amplifier to provide a low frequency (11Hz), small AC wiggle ($\approx 15\mu V$) and measure the current dI across the SET. The data acquisition are all computerized with the Labview program to control National Instruments DAQ (NI-DAQ).

For $I - V$ measurement, we use the homemade voltage sweep box for a rough scan first and NI-DAQ generated V_{sd} for data acquisition. Since the circuit diagram of $I - V$

measurement is the simplified version of G_d measurement, we only illustrate the latter. As shown in Fig. 5.13, a DC bias from the NI-DAQ and an AC wiggle from the Signal Recovery 7225DSP lock-in amplifier are connected to a homemade opto-isolator. Both the NI-DAQ and lock in amplifier are AC powered and regarded as "dirty ground", while our homemade electronics are battery powered and regarded as "clean ground". The opto-isolator is used to isolate the two different grounds. Based on the same idea, the gate voltage V_g, generated by NI-DAQ, is also applied to the gate of the SET through an opto-isolator. After a voltage divider, V_{sd} and dV are applied to the SET by a summing amplifier. The current amplifier is floated and buffered by a AD795 voltage amplifier which changes the floating current amp to a single end setup. V_g, the amplified I_{SET} and V_{sd}, are recorded by the computer. dI, dV and the phase are measured with the lock in amplifier for measuring G_d. The $I - V$ curve is obtained without applying an AC wiggle from the lock in amplifiers, and no summing amplifier is needed. V_g is applied to vary the S-SET offset charge.

G_d calibration

As we mentioned in chapter 3, a reliable measurement of G_d is essential in calibrating the matching network and analyzing the quantum noise. In our setup, we have extra resistance from the small microwave cables and 2K resistance in DC line. Also, there is some shunt

VA-Homemade voltage amplifier CA-Homemade current amplifier
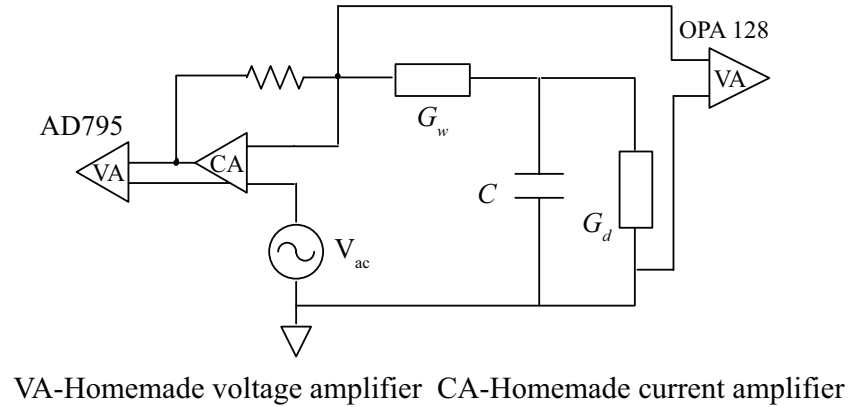
Figure 5.14. Schematic diagram of G_d calibration, including serial conductance G_w and parallel capacitance C.

capacitance from BNC cables and lock in amplifier, etc. The value of these capacitances

is derived from the phase measurement. Fig. 5.14 shows the simplified circuit diagram considering the extra wiring conductance G_w and shunt capacitance C. We have

$$G_{\text{meas}} = \frac{dI_{\text{meas}}}{dV_{\text{meas}}} = \frac{G_w(i\omega C + G_d)}{G_w + i\omega C + G_d} \tag{5.1}$$

in which G_{meas} is the measured differential conductance. Rewriting this we have

$$G_d = \frac{G_{\text{meas}}G_w - i\omega C(G_w - G_{\text{meas}})}{G_w - G_{\text{meas}}}. \tag{5.2}$$

From $|G_d|^2 = G_d G_d^*$, we have

$$|G_d|^2 = \frac{|G_{\text{meas}}|^2 G_w^2 - 2\omega C G_w^2 \text{Im} G_{\text{meas}} + \omega^2 C^2(G_w^2 + |G_{\text{meas}}|^2 - 2G_w \text{Re} G_{\text{meas}})}{G_w^2 + |G_{\text{meas}}|^2 - 2(\text{Re} G_{\text{meas}})G_w} \tag{5.3}$$

In order to determine G_w and C, we DC bias the SET in the center of the Coulomb Blockade region, where $G_d \approx 0$. We then have

$$G_w = \frac{\text{Im}^2 G_{\text{meas}}^0 + \text{Re}^2 G_{\text{meas}}^0}{\text{Re} G_{\text{meas}}^0}, \tag{5.4}$$

and

$$\omega C = \frac{\text{Im}^2 G_{\text{meas}}^0 + \text{Re}^2 G_{\text{meas}}^0}{\text{Im} G_{\text{meas}}^0}, \tag{5.5}$$

where G_{meas}^0 is the measured differential conductance of the SET at the center gap. From Eq 5.4 and Eq 5.5, we get $G_w \approx 4.2 \times 10^{-4}$S and $C \approx 1.6\mu$F experimentally. Since $G_w \gg G_{\text{meas}}$ in general, a good approximation to G_d is given by

$$|G_d|^2 \approx \frac{G_w(|G_{\text{meas}}|^2 - 2\omega C \text{Im} G_{\text{meas}})}{G_w - 2(\text{Re} G_{\text{meas}})} + \omega^2 C^2 \tag{5.6}$$

RF-SET characterization

In this section, we focus on the method of identifying the resonant frequency f_0 of the LC resonator and measuring the charge sensitivity of the RF-SET.

Resonant frequency f_0 of the RF-SET

In our simplified lossless model, the reflection power from the LC resonator changes most with G_d at f_0, which provides a direct way to identify f_0. The reflection power is measured with an Agilent 8753 transmission and reflection network analyzer. As shown in Fig. 5.10, the RF input port of the ^{3}He fridge is connected to the RF output of the network analyzer where it generates a scanning wave from 300KHz to 3GHz. Depending on the impedance matching, part of the signal will be reflected from the resonator, transferred through the bias tee, to the directional coupler, then amplified by the HEMT, the room temperature amplifier and finally measured with the network analyzer. We usually bias the SET at the center of the gap and in the above gap regime where the values of G_d are quite different. From the network analyzer, one can find the maximum difference of the reflected power in the frequency domain at certain frequency, which is f_0. Based on our LC design, we find a very sharp dip in the reflected power for SETs with 25kΩ at f_0, indicating that almost all the power is transmitted to the tank circuit. In contranst, at the center of the gap ($G_d \approx 0$), we find $\Gamma \approx 1$, indicating the power being totally reflected. For these measurements, we have to cool the sample below the critical temperature of aluminum. At high temperatures, our matching network is not superconducting and the lossless model is invalid. Also, the normal SET will act like a normal resistor at room temperature and there is no change in the reflection signal at different source drain bias. Usually, a dip in the reflection signal does not always indicate the f_0 of the resonator.

Charge sensitivity of RF-SET

As one of the most important parameters for a charge detector such as RF-SET, charge sensitivity (δq) describes the lowest required signal that can be discriminated from the noise floor with a signal to noise ratio (SNR) equal to 1. For example, a SET with $\delta q = 1 \times 10^{-5} e/\sqrt{\text{Hz}}$ means it can detect a charge of $1/100000e$ in one second.

In our experiment, δq is measured with a spectrum analyzer (Agilent E4408B) in the frequency domain. For the measurement, we apply: (1) a DC source drain bias to S-SET in the sub-gap region where is predicted to have a good δq; (2) a DC+AC wiggle to the gate through a bias tee; (the AC wiggle with frequency f_g is generated with a lock in amplifier or
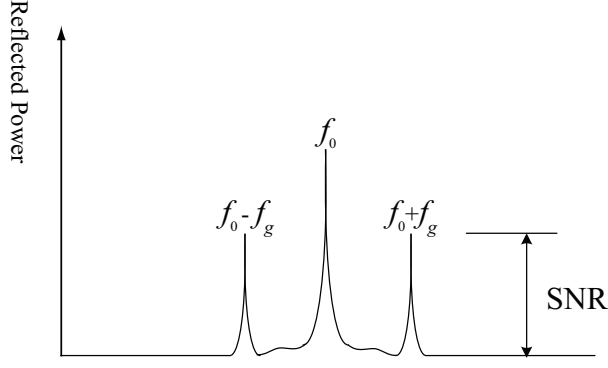
Figure 5.15. Illustration of charge sensitivity measurement.

Agilent 8648C signal generator) and (3) a carrier wave with the center resonant frequency the same as the LC resonator frequency to the S-SET through a bias tee shown in Fig. 5.10. The power in the reflected signal is monitored by the spectrum analyzer.

A small charge excitation results in two side peaks around the carrier wave, at frequencies $\pm f_g$ from f_0. For different V_{sd} and V_g, the S-SET will show different $\partial G_d / \partial n_g$, and the height of side peak will change accordingly. As illustrated in Fig. 5.15, from the height of the side peak, we can find the SNR, and calculate δq from:

$$\delta q = \frac{\Delta Q}{\sqrt{2\mathrm{BW}} \times 10^{\mathrm{SNR}/20}},\qquad(5.7)$$

where BW is the resolution bandwidth of the spectrum analyzer and ΔQ is the ratio of the wiggle's amplitude to the period of Coulomb oscillation and is in units of e. The Coulomb oscillations are measured by fixing a DC bias in the sub-gap region and scanning V_g. A $\sqrt{2}$ in the denominator accounts for the two side peaks while we only need one to extract the information.

Many theories focus on the improvement of δq for the normal SET, but few for the S-SET. Experimentally, δq is very sensitive to V_g, V_{sd}, the size of charge modulation, etc. We adjust these parameters to get the largest SNR with a fixed ΔQ and bandwidth. However, since δq is an intrinsic property of the S-SET, there should be some "particular" S-SET whose δq approaches the theoretical limit. Our research also involves a lot of fabrication work in finding these "particular" S-SETs including fabricating the asymmetry S-SET.

Eq.(3.43) gives us some hints. In general, a larger $\frac{\partial G_d}{\partial Q}$ will lead to a smaller δq. Intuitively, since G_d also affects the working conditions of the RF resonator, how well the SET responds to the offset charge on the SET island indicates how sensitive it is as a charge detector.

The S-SET quantum noise measurement setup is similar to that for measuring δq. Instead of adjusting the settings of the spectrum analyzer manually, we connect spectrum analyzer to the computer using GPIB. The computer carries out a band power measurement on the spectrum analyzer with a Labview program. All the scanning including V_{sd}, V_g and data acquisition are computerized as well to minimize interruption.

CHAPTER 6

EXPERIMENTAL RESULTS

This section presents some experimental results including the RF-SSET characterization, on-chip matching network calibration, intrinsic quantum noise measurement, electrical amplifier calibration for the S-SET, and CPW characterization.

6.1 The S-SET characterization

Experimentally, we increase the superconducting gap of the S-SET by evaporating ultra thin film of aluminum.
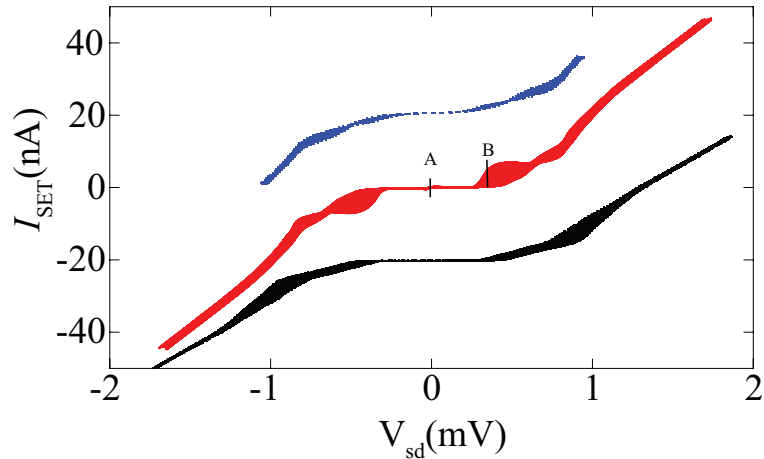
Figure 6.1. $I - V$ curves for S-SETs with different island thickness. Top to bottom: 25nm (blue), 7nm (red) and 5nm (black). Curves for 25nm and 5nm shifted vertically for illustration purposes. Points A and B are two different source drain bias for gate modulation as shown in Fig. 6.3.

Fig. 6.1 shows $I - V$ curves for three S-SETs with different island thickness. I_{SET} is measured by scanning V_{sd} for different V_g. From top to bottom, the thicknesses of the islands are 25nm, 7nm, 5nm and the measured values of Δ are 190μeV, 240μeV, 302μeV, which agree very well with other group's results. [75] Experimentally, a 7nm film is a good

choice since it satisfies: (1) a large Δ; and (2) $E_C > \frac{2\Delta}{3}$ for a significant DJQP and JQP feature. We also found that the $I-V$ curve for the 5nm S-SET shows asymmetry at positive and negative biases, indicating the asymmetry of the two tunnel junctions.
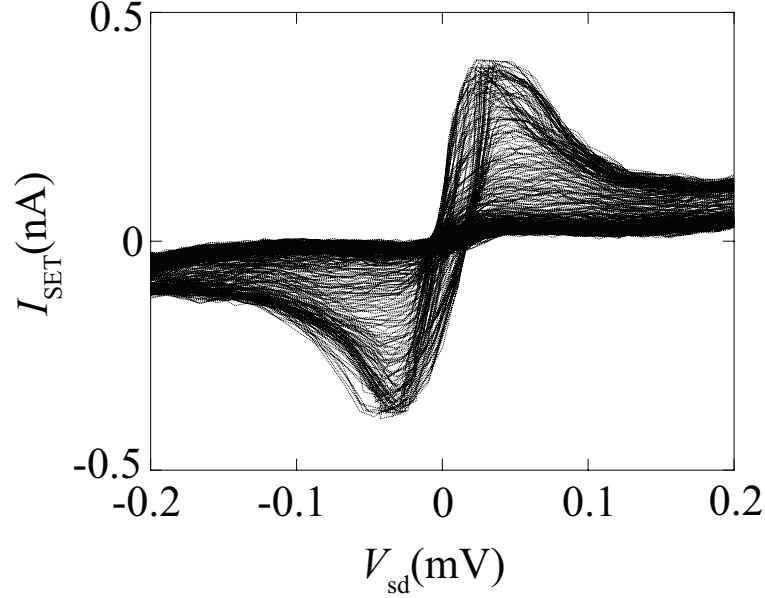
Figure 6.2. Supercurrent of S-SET near zero bias for different V_g.

All data shown below is from one of the 7nm S-SETs. It's normal state resistance was 27kΩ and its charging energy $E_c = 237\mu$eV as measured by the location of the DJQP peak at $eV_\mathrm{sd} = 2E_c$. The Josephson coupling energy E_J is given by

$$E_J = \frac{\Delta_i \Delta_l}{2(\Delta_i + \Delta_l)} \frac{h/e^2}{R_n} \approx 51\mu\mathrm{eV}, \tag{6.1}$$

Δ_i and Δ_l are the superconducting gap size for the island and lead and are determined by the film thickness. (In double angle shadow evaporation, we deposit 7nm for the island and 30nm for the lead.) The 7nm S-SET shows a clear supercurrent feature at zero bias, which is illustrated in Fig. 6.2. The maximum current is around 0.4nA and the differential conductance is around 1.4×10^{-5}S near zero bias. Theoretically, the maximum conductance at zero bias is given by [76]

$$G_d = R_K f^2(E_c/\Delta)/8M_\mathrm{eff}(R_{T_1}^2 + R_{T_2}^2) \tag{6.2}$$
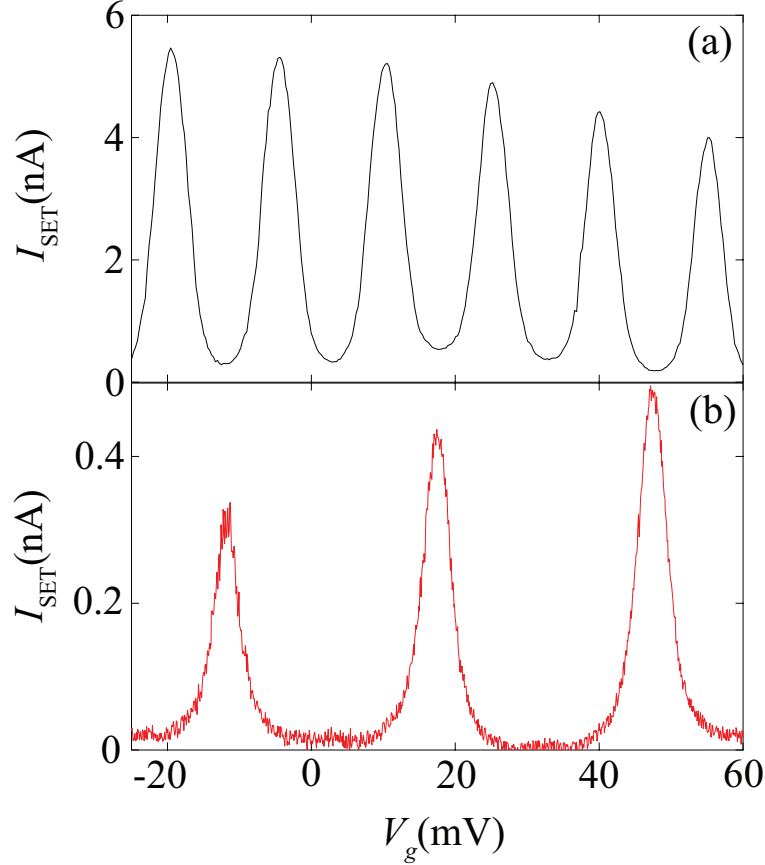
Figure 6.3. Coulomb oscillations of the S-SET at (a) DJQP, (b) Supercurrent region.

where $f(x) = \frac{2\arccos(-x)}{\pi(1-x^2)^{1/2}}$ and M_{eff} is a material parameter which refers to the number of effective conduction channels through the junctions. R_{T_1} and R_{T_2} are two junction resistance. The $I-V$ curve in Fig. 6.1 and the differential conductance in Fig. 6.4 indicate a very good symmetry and each junction resistance is approximately 13.5kΩ. The differential conductance G_d we measured at zero bias indicates $M_{\text{eff}} = 93$, a reasonable value considering the granularity of the films.

At zero bias as shown in Fig. 6.3, when the S-SET is biased at point A in Fig. 6.1, the supercurrent has an oscillation of $2e$ period. The tunneling process only involves the Cooper pairs and does not require extra source drain bias. The $2e$ period is due to electron's even-odd parity effect on the SET island. The periodicity disappears as we raise temperature from 300mK to 800mK and the supercurrent is washed out by thermal fluctuation. When we bias the S-SET at the DJQP, such as point B in Fig. 6.1, it shows the e-periodic Coulomb
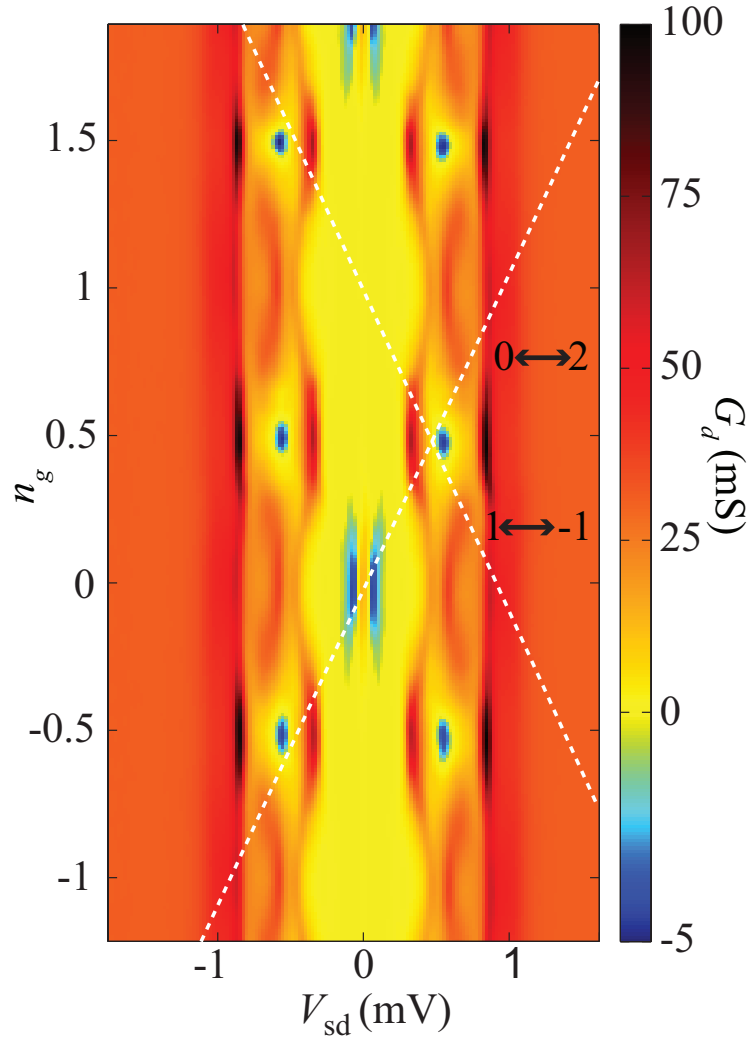
Figure 6.4. G_d for the S-SET versus V_{sd} and n_g. NDC is visible for V_{sd} and n_g in the vicinity of the supercurrent and the DJQP cycle. Cooper-pair resonance $0 \leftrightarrow 2$ and $1 \leftrightarrow -1$ are shown as the dashed lines; the DJQP cycle occurs at their intersection.

oscillation as shown in Fig.6.3(a). At this spot, both Cooper pairs and quasiparticles are involved in the transport process.

We use standard lock-in techniques to measure G_d versus dc source-drain bias V_{sd} and island charge number induced by the gate, $n_g = V_g C_g / e$ by applying a small ac voltage V_{ac} (15μV at 11Hz) in addition to V_{sd}. As shown in Fig. 6.4 [4], G_d is 2e periodic in n_g, showing a supercurrent at $n_g = 0, 2, \dots$ The two dotted lines refer to the Cooper pair resonances $0 \Leftrightarrow 2$ and $1 \Leftrightarrow -1$. The resonance condition for J1 (junction one) is given by the line
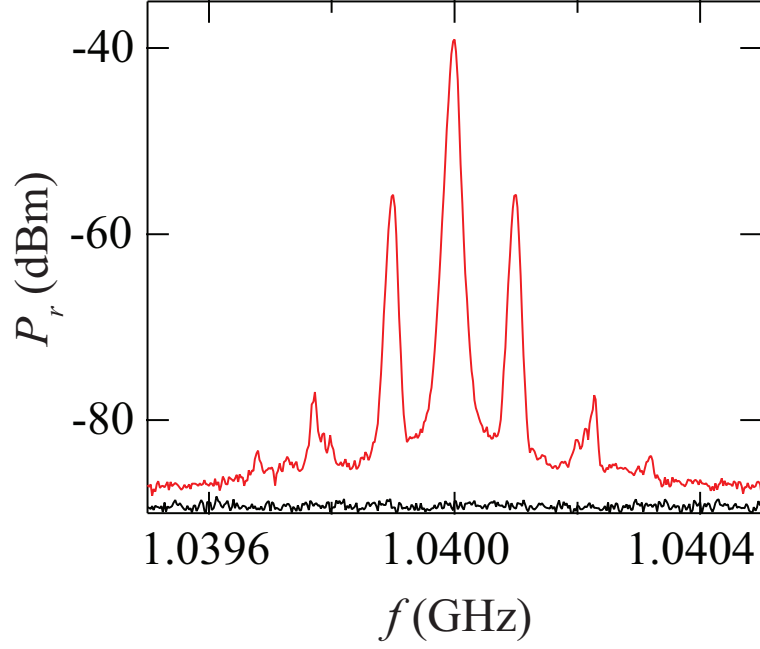
Figure 6.5. Amplitude-modulated reflected power for a charge modulation of 0.01e at 100kHz. The lower curve is the noise floor of the amplifier chain for $I = 0$.

$$(C_2 + C_g)V_{\text{sd}} = e(n_g - n + 1) \tag{6.3}$$

and for J2 (junction two) by the line

$$C_1 V_{\text{sd}} = e(n - n_g). \tag{6.4}$$

The intersection of these lines gives the location of the DJQP resonance peak. Fitting the Cooper-pair resonance lines to the data in Fig. 6.4 allow us to determine $C_{1(2)} =$174 (160) aF and $C_g = 11$ aF. Interestingly, there are several places in the $V_{\text{sd}} - n_{\text{g}}$ plane at which $G_d < 0$, as shown in the blue part in Fig. 6.4. At these points, the S-SET exhibits negative differential conductivity (NDC). NDC is also clearly visible in Fig. 6.1, as decreasing current with increasing bias just past the DJQP current maximum. The NDC regions are associated with Cooper-pair resonances, occurring on the high-bias side of both the supercurrent and the DJQP features.

Fig. 6.5 shows a charge sensitivity measurement for the RF-SSET. We measured the amplitude-modulated reflected power for a charge modulation of $0.01e$ at 100kHz. The lower

black curve is the noise floor of the amplifier chain for $I = 0$. We find $\delta q \approx 1.7 \times 10^{-6} e \sqrt{\text{Hz}}$. If the noise contribution of the HEMT amplifier is excluded, we find an intrinsic charge sensitivity $\delta q \approx 0.76 \times 10^{-6} e \sqrt{\text{Hz}}$.

6.2 On-chip superconducting resonator for noise calibration
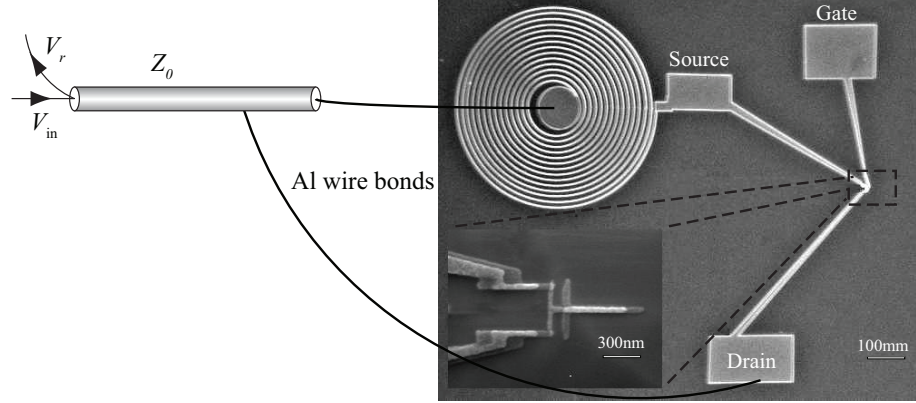
Figure 6.6. Scanning electron micrograph of an on-chip matching network prior to wire bonding, with wire bonding to the coaxial feedline shown schematically. The inset shows an electron micrograph of the SET.

One of the on-chip superconducting matching network designs is shown in Fig. 6.6. The network is fabricated at the same time as the SET using e-beam lithography and double angle Al evaporation. The number and spacing of the turns of the spiral inductor (linewidth 3μm, line spacing 20μm) determine its inductance L. The inset of Fig. 6.6 shows a scanning electron micrograph of the SET with junction area about 40×60nm^2. The center of the spiral inductor is wire bounded with an Al wire to the central pin of a coaxial cable and the ground lead of the SET is similarly bonded to the cable shield. Techniques for extracting L and C_p from the reflected power measurement for different G_d were discussed in Sec.3.2. We find $L \approx 169$nH and $C_p \approx 0.14$pF for an optimized 14 turn spiral inductor.

The calibration of the LC resonator is implemented at 300mK since f_0 shifts at higher ambient temperatures, as illustrated in Fig. 6.7. At temperatures above 1.2K, there is no resonance since the inductor is not superconducting. When we vary the ambient temperature from 1.1K to 0.5K, f_0 shifts from 1.01GHz to 1.04GHz. This is due to the kinetic inductance which depends strongly on the London penetration depth λ_L, describing the
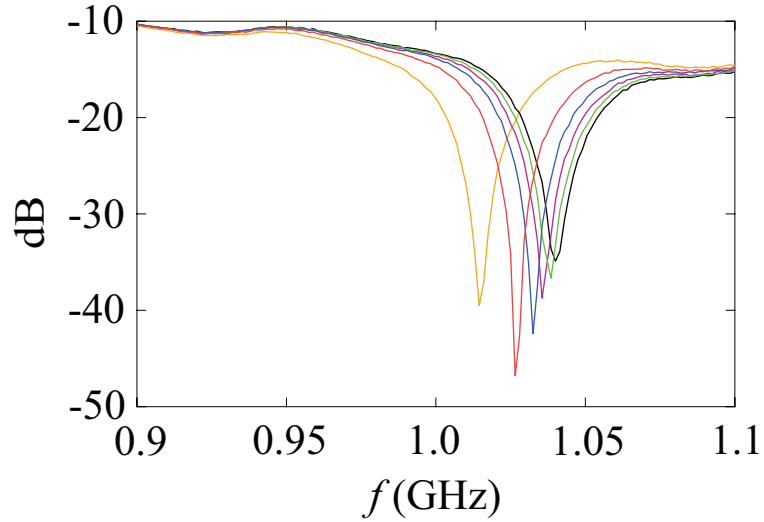
Figure 6.7. Resonance of the *LC* matching network for different ambient temperature. From left to right, 1.1K (orange), 1.0K (red), 0.9K (blue), 0.8K (purple), 0.7K (green) and 0.5K (black).

depth at which supercurrents flow. As the ambient temperature decreases, λ_L decreases and the kinetic inductance also decreases accordingly, which results in an increase of f_0. For temperatures below 500mK, λ_L is roughly constant and there is no further shift in f_0.
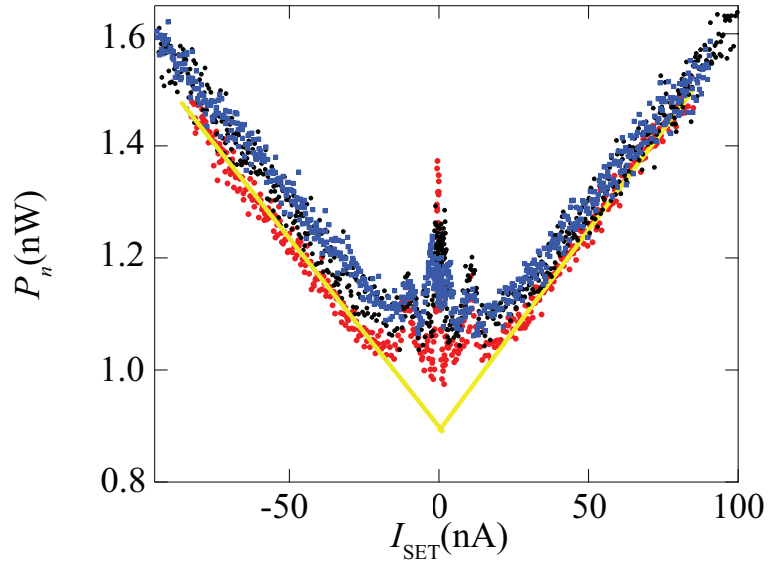
Figure 6.8. Noise power $\mathcal{P}_n$ at the output of the amplifier chain versus SET current I at 300mK (red), 0.9K (black) and 1.1K (blue). The yellow line is a curve fit to P_n for 300mK.

In order to implement the quantum noise measurements on S-SET/resonator system, we have to differentiate between the noise from the cryogenic amplifiers and the S-SET by using the on-chip superconducting resonator. Fig. 6.8 shows the integrated noise power $\mathcal{P}_n$ at the output of the amplifier chain versus DC current through the S-SET I_{SET}. The red, black and blue curves show $\mathcal{P}_n$ measured at 0.3K, 0.9K, and 1.1K. As can be seen from Fig. 3.8, the total noise $\mathcal{P}_n$ which includes contributions from the S-SET, the HEMT amplifier, and the circulator is given by: $\mathcal{P}_n = A(k_B T_{\text{HEMT}} + |\Gamma_{\text{in}}|^2 k_B T_{\text{circ}} + P_{\text{SET}}(I))\Delta f$. This expression is different from Eq. 3.44 since $\mathcal{P}_n$ is measured at the output of the amplifier chain and the gain is considered. $P_{\text{SET}}(I)$ is the noise per unit frequency emitted by the S-SET. This expression for $\mathcal{P}_n$ is significantly simplified over similar results in the literature due to the presence of the circulator, which prevents noise emitted from the input of the HEMT amplifier from reaching the sample, reflecting off it, and contributing to the total output noise. Analysis of the contribution of this noise wave is complex, since it is usually partially correlated with noise at the output of the HEMT amplifier. [77] $A = 61$dB is the gain of the amplifier chain and is determined from the slope of the linear part of $\mathcal{P}_n$ versus I_{SET}, since in this regime $P_{\text{SET}}(I)$ is given by the expression

$$P_{\text{SET}}(I) = 4(\omega_0/\gamma_T)^2 Z_0 e I_{\text{SET}}. \tag{6.5}$$

The measured gain agrees very well with that specified from the amplifier data sheet. $T_{\text{HEMT}} = 9.5$K (which dominates the amplifier noise) was determined from the intersection of the high-current linear asymptotes of $\mathcal{P}_n$ extrapolated back to $I = 0$. The circulator's contribution to this measurement was negligible, since $|\Gamma_{\text{in}}|^2 \ll 1$ for large I. Finally, $T_{\text{circ}} \approx 2.9$K was found by measuring $\mathcal{P}_n$ at V_{sd} and n_g in the subgap region such that $I = 0$ and subtracting the HEMT contribution to $\mathcal{P}_n$. The derived noise temperature agrees very well with the HEMT's data sheet and circulator's ambient temperature. To measure Γ_{in}, we applied a very small carrier wave (-149dBm) and measured the reflected power. For most bias voltages, the noise from the circulator is negligible given $|\Gamma_{\text{in}}|^2 \ll 1$. We also found two noise peaks appearing near $I_{\text{SET}} \approx 10$nA, which are caused by the DJQP and JQP tunneling cycles.

6.3 Intrinsic quantum noise measurement

The regions of NDC have special significance for the quantum noise properties of the S-SET. When the S-SET is biased above the DJQP resonance (blue detuning), Cooper pairs must emit energy to tunnel. Similarly, when the S-SET is biased below the resonance (red detuning), Cooper pairs must absorb energy as illustrated in Fig. 6.9. Furthermore, in terms of the picture of resonator damping given above, if $G_d < 0$ we expect both $\gamma_{\mathrm{SET}} < 0$ and $|\Gamma_{\mathrm{in}}| > 1$. Physically, this negative damping corresponds to net emission of energy into the resonator by the S-SET.
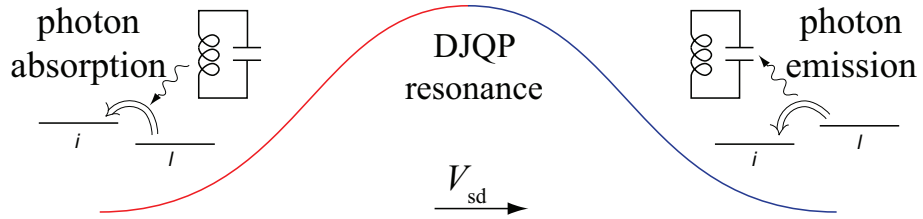
Figure 6.9. DJQP cycle. When the S-SET is biased in n_g and V_{sd} so that Cooper pairs do not have enough energy to tunnel on or off the island (that is, the S-SET is biased to the left of both Cooper-pair resonance lines in Fig.6.4), a photon must be absorbed from the resonator for tunneling to occur. Similarly, when the S-SET is biased so that Cooper pairs have excess energy (to the right of both resonances in Fig.6.4), a photon must be emitted during tunneling.

A quantum noise description of the S-SET is appropriate given the asymmetry of emission and absorption. We use an effective temperature description discussed in Sec.3.4 in which the quantum noise is given by

$$S_I(\omega_0) + S_I(-\omega_0) = 4k_B T_{\mathrm{SET}} C_{\mathrm{p}} \gamma_{\mathrm{SET}} \tag{6.6}$$

$$S_I(\omega_0) - S_I(-\omega_0) = 2\hbar\omega_0 C_{\mathrm{p}} \gamma_{\mathrm{SET}} \tag{6.7}$$

for $\hbar\omega_0$ sufficiently small compared with $k_B T_{\mathrm{SET}}$.

Fig. 6.10(a) and (c) show the measured intrinsic noise $\mathcal{P}_{\mathrm{SET}}$ versus V_{sd} and n_g at 300mK and 900mK in the vicinity of the DJQP resonance on a logarithmic scale. The noise is minimum for red detuning with respect to DJQP, and maximum for blue detuning. Here we focus on the DJQP region for several reasons. First and foremost, an S-SET operated
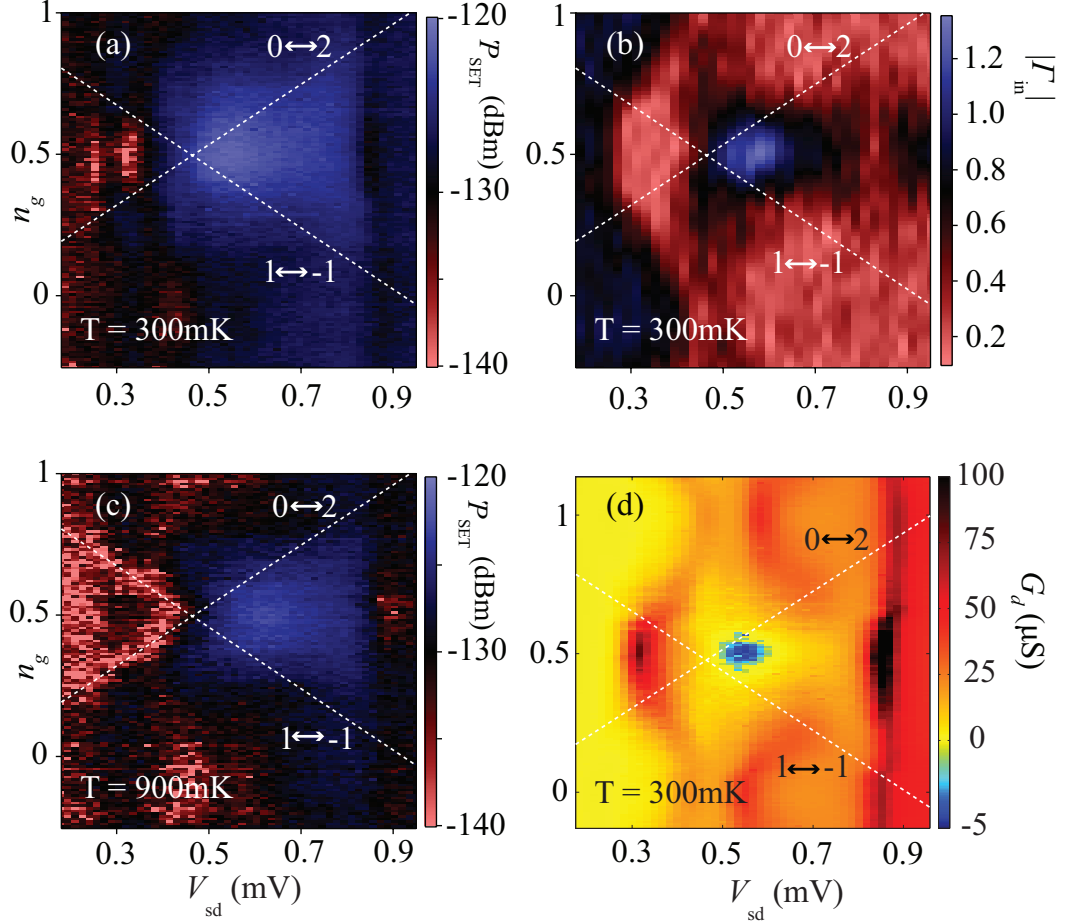
Figure 6.10. Noise and reflected power measurements. (a) $\mathcal{P}_{\text{SET}}(V_{\text{sd}}, n_g)$ at 300mK. Cooper-pair resonances are shown by the dashed lines, and the center of the DJQP cycle occurs at their intersection. Noise is maximal for blue detuning and minimal for red detuning. (b) $|\Gamma_{\text{in}}|(V_{\text{sd}}, n_g)$ at 300mK. A small region for which $|\Gamma_{\text{in}}| > 1$ exists for blue detuning. (c) At 900mK, $\mathcal{P}_{\text{SET}}(V_{\text{sd}}, n_g)$ is smaller in the blue-detuned region (in agreement with a lessening of NDC there for high temperature). The reduction of $\mathcal{P}_{\text{SET}}$ in the red-detuned region is more pronounced, and tracks exactly the Cooper-pair resonance lines. (d) $G_d(V_{\text{sd}}, n_g)$ at 300mK. The region of NDC corresponds nearly exactly to that for which $|\Gamma_{\text{in}}| > 1$ in (b).

near the DJQP resonance has been predicted to have the ideal balance of sensitivity and backaction needed to approach the quantum limit. Second, near this cycle, the S-SET's quantum noise properties are expected to depend strongly on the SET bias V_{sd} and n_g with respect to this intersection. Last, δq of the S-SET is typically excellent here. Empirically, we find the best δq for V_{sd} lying between DJQP and JQP.

Our measurements of the S-SET noise characteristic show excellent correspondence with photon emission and absorption by the S-SET. We show this correspondence by measuring
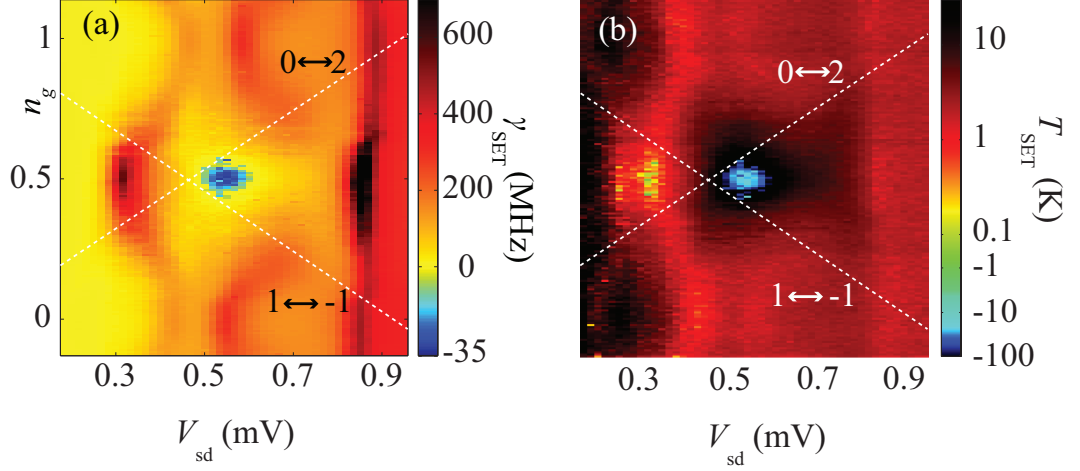
Figure 6.11. Quantum noise of the S-SET. (a) S-SET damping rate γ_{SET}. (b) S-SET effective temperature T_{SET} at f_0. Together, these give a complete and quantitative description of the S-SET quantum noise.

$|\Gamma_{\mathrm{in}}|$ of the tank circuit over the same range of V_{sd} and n_g, as shown in Fig. 6.10(b). For most values of V_{sd} and n_g, we found $|\Gamma_{\mathrm{in}}| < 1$, indicating net absorption by the S-SET. However, when the S-SET is blue detuned, there is a region for which $|\Gamma_{\mathrm{in}}| > 1$, indicating emission. Here the S-SET provides negative damping, returning more power to the resonator than is delivered by the radio frequency excitation. Remarkably, therefore, as we measure $|\Gamma_{\mathrm{in}}| > 1$, we are directly measuring photon emission by Cooper pairs as they tunnel. Comparing this to the S-SET conductance in the same region as shown in Fig. 6.10(d), we again see excellent correspondence. The region of negative damping corresponds exactly to the region of NDC. This is in accord with our expectation based both on the forms of γ_{SET} (Eq. 3.54) and Γ_{in} (Eq. 3.29), and with the more sophisticated quantum noise view of Eq. 6.6 and Eq. 6.7.

The effective temperature T_{SET} can be derived from measurements of $\mathcal{P}_{\mathrm{SET}}$ (see Eq. 3.46), where γ_{SET} is determined from measurement of G_d. Results are shown in Fig. 6.11(a) and (b) at 300mK. We found the tendency of the S-SET to either emit or absorb which is measured by γ_{SET} and its degree of asymmetry which is measured by S-SET's effective temperature ($T_{\mathrm{SET}} \propto (S_I(\omega_0) + S_I(-\omega_0))/(S_I(\omega_0) - S_I(-\omega_0))$ vary strongly with V_{sd} and n_g. For blue detuning where Cooper pairs must give off energy, we observe both negative damping and a negative effective temperature. As illustrated in the figure, although T_{SET} is large in some areas, for most bias points we have $T_{\mathrm{SET}} \lesssim 1$K, make it smaller than

eV_{sd}/k_B but large enough that our assumption $k_B T_{SET} \gg \hbar\omega_0$ in Eq. 6.6 and Eq. 6.7 is still valid. For red detuning, where the S-SET is strongly absorbing, T_{SET} can be as low as 100 ± 40mK, less than the ambient temperature and indicating that the S-SET is capable of refrigeration. Although there are theoretical expressions for γ_{SET} and T_{SET} near the DJQP, they assume capacitive coupling of the S-SET to a resonator rather than our direct electrical connection [40,61], and also ignore high-order tunneling processes [78,79] known to be important for our relatively low-resistance S-SET. Nonetheless, theory predicts a minimum $T_{SET} \approx 250$mK for an S-SET with our parameters, in reasonable agreement with our results.

Here, we prefer T_{SET} and γ_{SET} as a description of the S-SET quantum noise over the Fano factor because the latter is only caused by the fluctuations of the number of tunneling electrons. [80] In our experiment, variations in $\mathcal{P}_{meas}$ arising from electron number fluctuations are indistinguishable from those due to emission/absorption of photons.

As an ultra sensitive charge detector, we now can estimate the measurement capability of our S-SET relative to the quantum limit. We imagine coupling the S-SET to some external device such as quantum dot (QD). Proximity to the quantum limit can be represented by the parameter χ, which is given by $\chi \approx \sqrt{6E_c^2 e(\delta q)^2/I\hbar^2}$. For a typical currents of $I \approx 5$nA near the DJQP and neglecting the noise of the HEMT, we estimate an intrinsic value of $\chi \approx 3.6$. When amplifier noise is included, we obtain $\chi \approx 8$. The nearest comparable results quote a value of $\chi \approx 15$ [78] when neglecting the noise of secondary amplifiers. When the noise of the secondary amplifiers is included, the resulting value for χ is about 48. For the normal SET, χ is given approximately by $\chi = \sqrt{8eE_c^2(\delta q)^2 R_\Sigma/V_{sd}\hbar^2}$. Using $R_\Sigma \approx 25$kΩ, $E_c = 1.55$meV, and $V_{sd} = 100\mu$V as for recent highly optimized results [3], we estimate $\chi \approx 42$ including amplifier noise. Assuming a roughly two-fold improvement in δq when amplifier noise is neglected (as is the case for our measurements) we estimate an intrinsic $\chi \approx 20$ for the normal SET, similar to the results reported from other group, but with clear means of further improvement.

However, there are limitations on the way we estimate χ. As we note, all these estimates are based on the results from orthodox model, which specifically neglects higher order process such as cotunneling of electrons or quasiparticles. In the case of a normal state

SET operated in the region where cotunneling dominates over the sequential tunneling, near quantum limited performance is expected to be possible. [81] Essentially, cotunneling allows transport of current through the SET without charge fluctuations on its island, reducing its backaction on the measured system. Due to the importance of higher-order processes most samples we made and measured, we expect that our estimates of χ are generally conservative. Further theoretical investigation is required for a better estimation to be made.

It is natural to think that one should reduce the noise added by the secondary amplifier such as the HEMT. While the best HEMT-based amplifiers typically have noise temperature T_n around 6K, there are other RF amplifiers that have demonstrated significantly lower noise. SQUID-based amplifiers, [82] for instance, have been operated at frequencies of several hundred MHz with T_n on the order of 50mK, and have been suggested as a replacement amplifier for the HEMT in attempts to produce a near quantum limited charge detector. In our experiment, the HEMT has noise temperature around 9.5K, which is equivalent to -122dBm in a 5MHz band power measurement. It is comparable to the intrinsic noise we measured at blue detuned region where the best χ is reported as illustrated in Fig. 6.10(a). Therefore, with a good matching superconducting resonator, it is unnecessary to replace the HEMT amplifier with a lower noise substitute for the derivation of the S-SET quantum noise.

6.4   S-SET as a charge-sensitive electrical amplifier

Generally, an amplifier is any device that changes, usually increases, the amplitude of a signal. The relationship of the input to the output of an amplifier usually expressed as a function of the input frequency is called the transfer function of the amplifier, and the magnitude of the transfer function is termed the gain. For an linear electrical amplifier, the input "signal" is usually a voltage or a current and the output signal is linearly proportional to the input signal. In other words, the gain of the amplifier is independent of the amplitude of the input signal. Ideally, an amplifier would be a totally linear device, but real amplifiers are only linear within limits. When the signal drive to the amplifier is increased, the output also increases until a point is reached where some part of the amplifier becomes saturated

and cannot produce any more output, resulting in distortion. In our experiment, the linear response of our RF-SSET is shown by the measurement of SNR versus input amplitude q_0 for the optimized charge sensitivity, in which q_0 is an ac component of amplitude that modulates the reflected signal from the tank circuit. We find good linearity occurs in the subgap region for an RF-SSET with a low junction resistance. [79] For such RF-SSETs, co-tunneling processes are important and the tunneling strength is characterized by the parameter α, which is given by $8E_J/E_c$, where E_J and E_c are the Josephson and charging energies. For samples with small α, the electron on the SET island is well defined, the transport is well described by the sequential tunneling picture: $I - V$ characteristic are sharp and vary strongly with DC offset charge Q_0. Although, we can achieve good charge sensitivities here, the same sharpness, however, prevents good linearity, since a large q_0 may move the S-SET away from optimal operation. For samples with $\alpha > 1$, such as the S-SET we discussed in this thesis ($\alpha = 1.72$), the quantum fluctuations of quasiparticles are substantial due to the co-tunneling process. This quantum fluctuations will smooth and broaden the subgap features thereby improving linearity: e.g., there are many places instead of one particular spot between the DJQP and JQP features for which the S-SET current is roughly independent of Q_0. This finding is of particular importance given interest in the RF-SSET with $\alpha > 1$ as a potentially quantum-limited linear amplifier.

For comparison of different linear electrical amplifiers, the most common parameters to use are the noise temperature T_n, which characterizes the noise the amplifier adds, and its power gain A_{SET}. A good amplifier will have low noise and high gain. Although in reality all amplifiers have $T_n > 0$, there is no classical lower bound on how little noise an amplifier can add. A noise temperature of zero is in principle possible. This is the consequence of the fact that classical measurements are passive. Quantum mechanically, however, as we mentioned earlier, backaction influences the measured system and results in added noise. Thus, there is a firm physical limit on how good an electrical amplifier can be. Linear response theory can be used to show that χ is directly related to the noise temperature T_n of the SET through the expression

$$\chi = \frac{k_B T_n}{\hbar \omega_0 / 2} \tag{6.8}$$

where ω_0 is the operating frequency of the S-SET. This expression simply states that the minimum noise an amplifier can add is equal to one half of a photon per unit bandwidth. For our operating frequency of $\omega_0/2\pi = 1\text{GHz}$ the quantum limit $\chi = 1$ corresponds to a noise temperature of $T_n = 25\text{mK}$. The power gain of the SET is simply defined as the ratio of the noise power per unit bandwidth $\mathcal{P}_{\text{SET}}/\Delta f$ it delivers to a subsequent classical amplifier to the noise power $k_B T_n$ at its input:

$$A_{\text{SET}} = \frac{\mathcal{P}_{\text{SET}}}{\Delta f k_B T_n} \tag{6.9}$$

This definition differs slightly from that used elsewhere in that it accounts for the efficiency of the tank circuit in delivering power from the SET to subsequent devices. It provides a more realistic estimate of the SET power gain, and also avoids difficulties that would otherwise arise at bias points where the S-SET has NDC. Combining Eq. 3.46, 3.56, 3.57, 3.58, 3.59, 3.60, and 3.61, we can derive a new expression for χ,

$$\chi = \sqrt{\frac{6}{\hbar^2} \frac{\mathcal{P}_{\text{SET}}}{\Delta f} E_c^2 \frac{\gamma_T^2 e}{I} \frac{1}{Z_0 (\partial I/\partial n_g)^2}}, \tag{6.10}$$

for which all terms can be determined directly from the measurements. From Fig. 6.12(a), there is a peak in the S-SET current I near the DJQP resonance, while the integrated noise $\mathcal{P}_{\text{SET}}$ is maximal for $V_{\text{sd}} > 2E_c/e$ and minimal for $V_{\text{sd}} < 2E_c/e$. In order to calculate χ we first find the S-SET differential conductance $G_d = \partial I/\partial n_g$ and the response of the S-SET current to changes in gate charge $\partial I/\partial n_g$ from the measured current $I(V_{\text{sd}}, n_g)$. In this case, we have done so by numerical differential of the data shown in Fig. 6.12(a). The resulting values of G_d, shown in Fig. 6.12(b), are in good agreement with values obtained by lock-in amplification as shown in Fig. 6.10(d).

The parameter $\partial I/\partial n_g$ is shown in Fig. 6.12(c). As is clear from the plot, $|\partial I/\partial n_g|$ is largest for $V_{\text{sd}} \approx 2E_c/e$ and gate charge n_g that places the S-SET on either side of the DJQP resonance. The charge sensitivity of the S-SET as well as its power gain A_{SET} can be expected to be largest in these regions, which are usually used for charge sensing. In addition, we expect that χ will be minimal in these same locations.
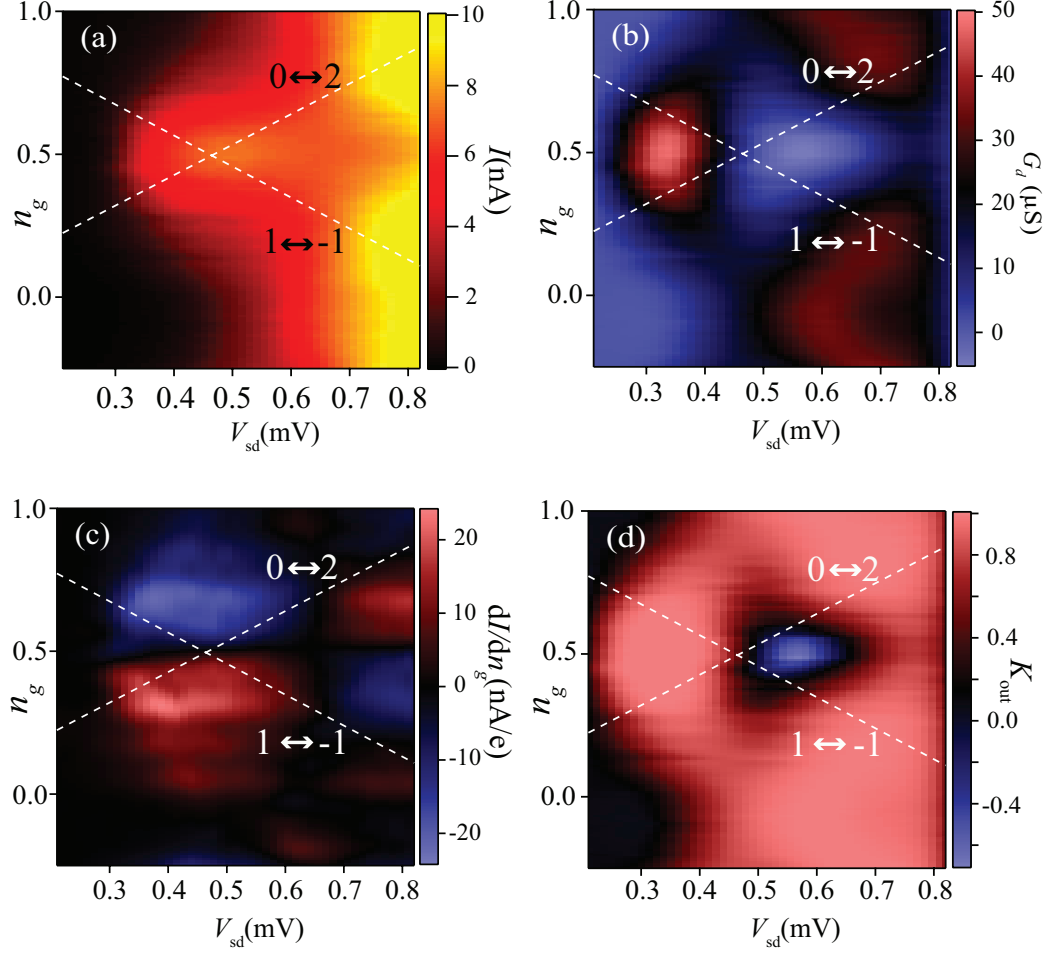
Figure 6.12. (a) S-SET current (b) differential conductance G_d derived from (a), (c) $\partial I/\partial n_g$ and (d) K_{out} versus gate charge n_g and S-SET source-drain bias V_{sd}.

Finally, in Fig. 6.12(d) we show the power transfer efficiency K_{out} of the tank circuit, which is derived from Eq. 3.39. As is clear from the plot, K_{out} is close to unity in the regions for which $|\partial I/\partial n_g|$ is large, indicating good matching between the S-SET and the coaxial feedline for these critical bias points. Furthermore, the fact that K_{out} is close to unity means that our definition of the S-SET power gain differs very little from one that does not account for the tank circuit for those bias points at which the S-SET will most likely be used. Finally, as we expected, K_{out} is negative at NDC from energy conservation since $|\Gamma_{\text{in}}|$ is greater than one here. Our use of definition from Eq. 6.9 for the S-SET power gain, as for the calculation of χ, avoids the difficulties posed by the presence of NDC.

The results presented in Fig. 6.12 put us in a position to calculate χ from Eq. 6.10 and subsequently A_{SET} from Eq. 6.9. To find χ, we use G_d as shown in Fig. 6.12(b) to find Γ_{SET}, use $\partial I/\partial n_g$ as in Fig. 6.12(c), and use our known E_c. The results of this calculation are shown in Fig. 6.13(a); note the logarithmic scale used to represent the magnitude of χ. To find A_{SET}, we simply calculate T_n from χ using Eq. 6.8, and then use T_n and $\mathcal{P}_{\mathrm{SET}}$ to determine the power gain through Eq. 6.9. These results are shown in Fig. 6.13(b), with the magnitude of A_{SET} again presented on a logarithmic scale.
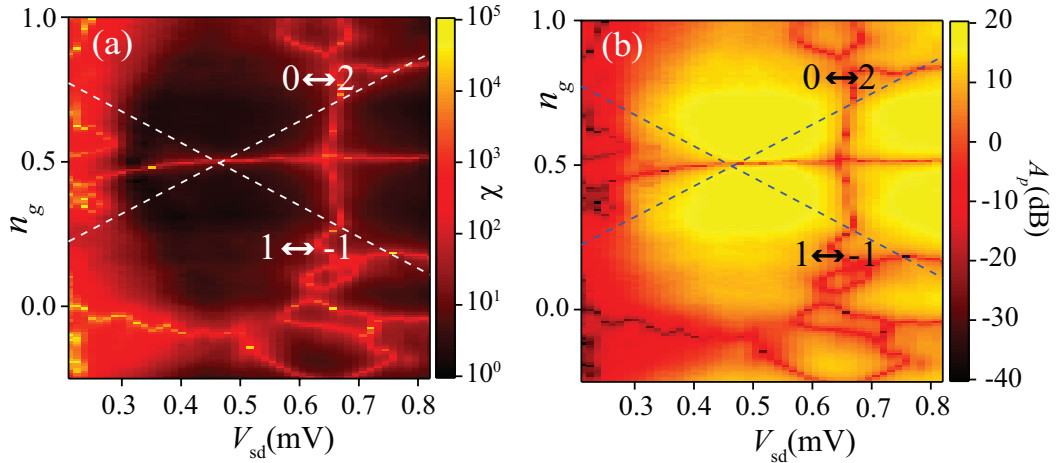

Figure 6.13. (a) χ (b) power gain A_p(dB) versus gate charge n_g and S-SET source-drain bias V_{sd}.

As is clear from Fig. 6.13(a), χ varies over several orders of magnitude in the vicinity of the DJQP resonance. In regions for which $\partial I/\partial n_g$ is large and charge sensitivity is good we find χ is minimal. In terms of noise temperature, we note that at $f_0 = 1\mathrm{GHz}$ the quantum limit $\chi = 1$ corresponds to a noise temperature $T_n = 25\mathrm{mK}$. Based on Fig. 6.13(a), the minimum noise temperature of our S-SET is therefore $T_n \approx 50\mathrm{mK}$, with $\chi \approx 2$. These results are in good agreement with our earlier estimate of $\chi \approx 3.6$, which was arrived using an entirely different estimate for the measurement time τ_{meas}, and an estimate of τ_φ based on a single value of I. It is important to note that for all values of V_{sd} and n_g considered, the physical limit $\chi > 1$ is always obeyed, giving us further confidence in our procedure. As shown in Fig. 6.13(b), the power gain A_{SET} also varies strongly near the DJQP resonance, reaching a maximum of $A_{\mathrm{SET}} \approx 20\mathrm{dB}$ in the same regions for which χ and T_n are minimal.

As such bias points, the S-SET operates as a high-gain, low noise amplifier with a noise temperature that approaches the minimum allowed by the laws of quantum mechanics. As a comparison, our GaAs-based HEMT amplifier has $T_{\text{HEMT}} \approx 9K$ with a power gain $A_{\text{HMET}} \approx 30dB$, placing it a factor over 300 from the quantum limit.

6.5 CPW characterization

To verify the idea that the introduction of a DC bias to a microwave cavity does not significantly disturb the cavity modes, we fabricated the coplanar waveguide cavity without the S-SET first.
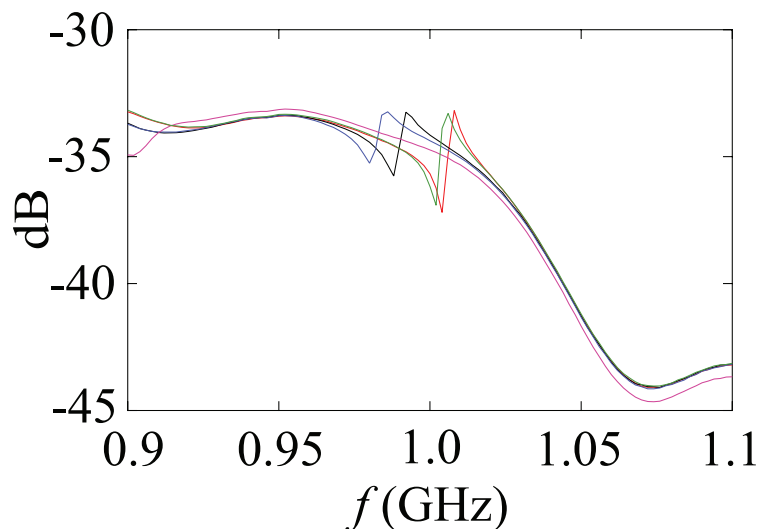
Figure 6.14. Reflected power versus frequency at 1.2K (pink), 1.0K (green), 0.8K (black), 0.5K (blue) and 0.3K (red).

The substrate for CPW is a $4''$ 500μm thick p-doped Si wafer with resistivity $\rho >$ 1000Ωcm and a 550nm thick layer of SiO_2. We designed a 1GHz CPW resonator to satisfy the RF setup in our ^{3}He refrigerator. The measured reflected power of the CPW is shown in Fig. 6.14. At 300mK, we saw a dip in the reflected power, indicating f_0 around 1.004GHz as expected. To confirm this, we measured the CPW from 0.3K to 1.2K and observed the resulting shift in f_0. Fig. 6.14 indicates that although the dip is not as deep as that of the on-chip matching network, it is still the resonance. The reasons for the shallow dip are complex: (1) The 1GHz waveguide is physically large (18mm by 8mm) and the Al bonding

wires are very long and crossing with each other. The wire bond will add extra parasitic capacitance and also introduce interference with rf lines. (2) Due to CPW's physical size, we did not make a shield copper box for it. The CPW is exposed to microwave radiation.

After confirming the resonant frequency, we introduced a 1V DC voltage bias and an 1mA DC current bias via the inductors to the CPW at 300mK individually. The resulting reflected power was essentially identical to the one without any DC bias. Therefore, our idea of introducing a DC bias to the microwave cavity works and the cavity modes are not disturbed.

CHAPTER 7

FUTURE WORK

In this thesis, we focused on the on-chip matching network design for the S-SET. With the superconducting resonator and cold trap evaporation technique we routinely fabricated SETs with δq about twenty times better than our early results. [79] Up to now, we have fabricated one of the world's most sensitive RF-SSET with $\delta q \approx 1.7 \times 10^{-6} e\sqrt{\text{Hz}}$. One of
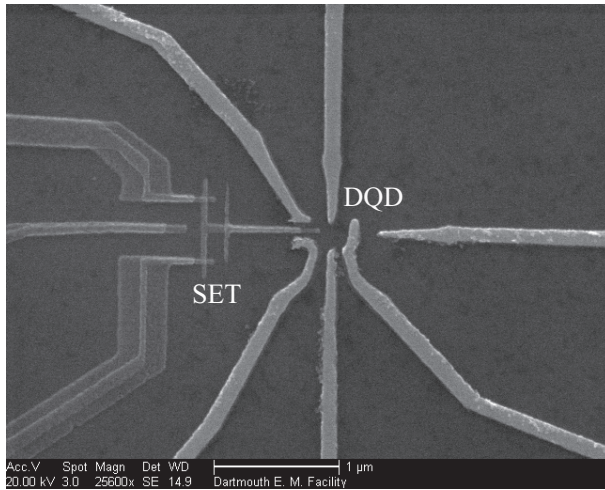
Figure 7.1. Scanning electron micrograph of S-SET/DQD on SiGe wafer.

our goals is to use this ultra sensitive electrometer for the real-time detection of electron tunneling through a double quantum dot (DQD), as shown in Fig. 7.1. The RF-SSET is a promising candidate for the readout of spin-based qubits in such DQDs.

Using a simplified LC model, we implemented a quantum noise measurement of the RF-SSET near the DJQP resonance. Using an effective thermal bath description, we found that the S-SET provides damping of the resonator modes proportional to G_d. A closer view of Fig. 6.4 indicates that the NDC, which corresponds to the negative damping, not only appears at the higher bias of the DJQP resonance, but also in the supercurrent region.

This measurement is very similar to those proposed for measurement of zero-point fluctuations. [83,84] Such measurements, if performed at lower temperatures and possibly higher frequencies, could be an interesting area for future investigation, as could be the possibility of producing laser-like instabilities [85,86] if the total quality factor Q_T is negative. In the LC model, this requires

$$|G_d| > \frac{C_p Z_0}{L}. \tag{7.1}$$

With the current resonator design, the NDC needs to be greater than 4×10^{-5}S, approximately three times what we can now achieve. In the future, we will improve the network design and reduce C_p further to lower the required G_d in Eq. 7.1.

We are currently working on a CPW resonator with $f_0 = 5$GHz. Its energy scale corresponds to $T \sim 250$mK and is significantly larger than the ambient temperature of the dilution fridge (15mK). Therefore, the superconducting circuit should be well quantized and we should be able to observe quantum effects in our system. A lasing effect observed with an S-SET embedded in the CPW resonator was recently demonstrated in the JQP regime. [87] In that case, the S-SET is treated as a qubit and the population inversion of it is created in the JQP cycle, thus producing the lasing action between a single artificial atom and the cavity. We expect to observe similar instabilities in the supercurrent regime of our system. By applying a small DC voltage bias or low frequency AC wiggle, the S-SET is set in the supercurrent regime. If the resonance of the CPW resonator ω_0 matches the energy difference ΔE of the charge states of the S-SET differing by one Cooper pair on the island, $\Delta E \approx \hbar\omega_0$, Cooper pair tunneling through the junctions is accomplished with simultaneous photon emission to the cavity. With laser-like instabilities, the Cavity-SSET system is fully quantum coherent and qualitatively different behavior may result.

BIBLIOGRAPHY

[1] A. Aassime, G. Johansson, Wendin, R. J. Schoelkopf, and P. Delsing, Phys. Rev. Lett. **86**, 3376 (2001).

[2] A. Aassime, D. Gunnarsson, K. Bladh, P. Delsing, and R. J. Schoelkopf, Appl. Phys. Lett. **79**, 4031 (2001).

[3] H. Brenning, S. Kafanov, T. Duty, S. Kubatkin, and P. Delsing, J. Appl. Phys. **100**, 114321 (2006).

[4] W. W. Xue, Z. Ji, F. Pan, Joel Stettenheim, M. P. Blencowe, and A. J. Rimberg, Nat. Phys. **5**, 660-664 (2009).

[5] A. J. Rimberg, *Introduction of a DC bias into a high-Q microwave cavity.* Notes, (2008).

[6] M. A. Nielsen, and I. L. Chuang, *Quantum Computation and Quantum Information*, (Cambridge University Press, UK, 2000).

[7] A. N. Korotkov, Phys. Rev. B **60**, 5737-5742 (1999).

[8] M. H. Devoret, and R. J. Schoelkopf, Nature **406**, 1039-1046 (2000).

[9] Y. Makhlin, G. Schön and Shnirman, Rev. Mod. Phys. **73**, 357-400 (2001).

[10] A. A. Cleark, S. M. Girvin, and A. D. Stone, Phys. Rev. B **67**, 165324 (2003).

[11] C. M. Caves, Phys. Rev. D **26**, 1817-1839 (1982).

[12] C. W. Gardiner and P. Zoller *Quantum Noise* (Springer,2000).

[13] A. A. Clerk, S. M. Girvin, A. K. Nguyen, and A. D. Stone, Phys. Rev. Lett. **89**, 176804 (2002).

[14] T. A. Fulton and G. J. Dolan, Phys. Rev. Lett. **59**, 109 (1987).

[15] K. K. Likharev, IBM J. Res. Dev. **32**, 144 (1988).

[16] D. V. Averin and K. K. Likharev, *Mesoscopic Phenomena in Solids* pp. 173-271, (Elsevier Science Publishers B. V., 1991).

[17] G. Johansson, P. Delsing, K.Bladh, D. Gunnarsson, T. Duty. A. Käck, G. Wendin, A. Aassime, *Quantum Noise in Mesoscopic Physics* pp. 337-355 (Kluwer Academic Publisher, 2003).

[18] M. P. Blencowe and M. N. Wybourne, Appl. Phys. Lett. **77**, 3845 (2000).

[19] M. Amman, R. Wilkins, E. Ben Jacob, P. D. Maker and R. C. Jaklevic, Phys. Rev. B **43**, 1146 (1991).

[20] Christoph Wasshuber. *Computational Single Electronics.* Springer-Verlag, New York, 2001.

[21] S. L. Pohlen. *Computational Single Electronics.* Ph.D. Thesis, Harvard University, 2000.

[22] D. V. Averin et al. JETP Lett., **50**, 367, (1989).

[23] J. M. Hergenrother, M. T. Tuominen, T. S. Tighe and M. Tinkham, IEEE Trans. Appl. Supercond. **3**, 1980 (1993).

[24] E. N. Visscher, S. M. Verbrugh, J. Lindeman, P. Hadley and J. E. Mooij, Appl. Phys. Lett. **66**, 305 (1995).

[25] P. Hadley, E. Delvigne, E. H. Visscher, S.Lähteenmäki, and J. E. Mooij, Phys. Rev. B **58** 15317 (1998).

[26] A. Massen van den Brink, G.Schön, and L. J. Geerligs, Phys. Rev. Lett. **67**, 3030 (1991).

[27] T. A. Fulton, P. L. Gammel, D. J. Bishiop and L. N. Dunkleberger, Phys. Rev. Lett, **63**, 1307 (1989).

[28] B. D. Josephson. Phys. Lett., **1**, 251, (1962).

[29] V. Ambegaokar and A. Baratoff. Phys. Rev. Lett., **10**, 486, (1963).

[30] R. J. Schoelkopf, P. Wahlgren, A. Kozhevnikov, P. Delsing and D. Prober, Science, **280**, 1238 (1998).

[31] P. W. Shor, *in Proceedings of the 35th Annual Symposium on the Foundations of Computer Science,* edited by S. Goldwasser (IEEE Computer Society, Los Alamitos, CA, 1994), pp. 124-134.

[32] L. K. Grover, Phys. Rev. Lett. **79**, 325, (1997).

[33] J. M. Elzerman, R. Hanson, L. H. Willems van Beveren, B. Witkamp, L. M. K. Vandersypen and L. P. Kouwenhoven, Nature (London) **430**, 431 (2004).

[34] J. R. Petta, A. C. Johnson, J. M. Taylor, E. A. Laird, A. Yacoby, M. D. Lukin, C. M. Marcus, M. P. Hanson and A. C. Gossard, Science **309**, 2180 (2005).

[35] R. G. Knobel and A. N. Cleland, Nature (London) **424**, 291 (2003).

[36] M. D. Lahaye, O. Buu, B. Camarota and K. C. Schwab, Science **304**, 74 (2004).

[37] V. B. Braginsky and F. Ya. Khalili, *Quantum Measurement* (Cambridge University Press, Cambridge, 1992).

[38] D. M. Pozer, *Microwave Engineering* (Hohn Wiley and Sons, 1998).

[39] W. W. Xue, B. Davis, F. Pan, J. Stettenheim, T. J. Gilheart, Z. Ji and A. J. Rimberg, Appl. Phys. Lett, **91**, 093511, (2007).

[40] A. A. Clerk and S. Bennett, New J. Phys, **7** 238, (2005).

[41] Brain C. Wadell, *Transmission Line Design Handbook* (Artech House, INC, 1991).

[42] P. L. D. Abrie, *Design of RF and Microwave Amplifiers and Oscillators* (Artech House, Boston, 2000).

[43] Y. Nakamura, C. D. Chen, and J. S. Tsai, Phys. Rev. Lett., **79**, 2328, (1997).

[44] T. Hayashi, T. Fujisawa, H. D. Cheong, Y. H. Jeong, and Y. Hirayama, Phys. Rev. Lett., **91**, 226804, (2003).

[45] J. R. Petta, A. C. Johnson, C. M. Marcus, M. P. Hanson, and A. C. Gossard, Phys. Rev. Lett., **93**, 186802, (2004).

[46] F. H. L. Koppens, C. Buizert, K. J. Tierlrooij, I. T. Vink, K. C. Nowack, T. Meunier, L. P. Kouwenhoven and L. M. K. Vandersypen, Nature, **442**, 766, (2006).

[47] D. Vion, A. Aassime, A. Cottet, P. Joyez, H. Pothier, C. Urbina, D. Esteve and M. H. Devoret, Science, **296**, 886-889, (2002).

[48] A. N. Korotkov, Phys. Rev. B **63**, 085312, (2001).

[49] S. A. Gurvitz, L. Fedichkin, D. Mozyrsky and G. P. Berman, Phys. Rev. Lett. **91**, 066801, (2003).

[50] R. Ruskov, A. N. Korotkov and A. Mizel, Phys. Rev. Lett., **96**, 200404, (2006).

[51] R. Ruskov, A. N. Korotkov and A. Mizel, Phys. Rev. B **73** 085317, (2006).

[52] S. Pilgram and M. Büttiker, Phys. Rev. Lett. **89**, 200401, (2002).

[53] A. A. Clerk and A. D. Stone, Phys. Rev. B **69**, 245303, (2004).

[54] D. V. Averin and E. V. Sukhorukov Phys. Rev. Lett. **95** 126803, (2005).

[55] A. A. Clerk, Phys. Rev. Lett. **96** 056801, (2006).

[56] N. P. Oxtoby, J. Gambetta and H.M.Wiseman, Phys. Rev. B **77** 125304, (2008).

[57] A. N. Korotkov, Phys. Rev. B **67**, 235408, (2003).

[58] A. Shnirman and G.Schön, Phys. Rev. B, **57**, 15400, (1998).

[59] R. J. Schoelkopf, A. A. Clerk, S. M. Girvin, K. W. Lehnert, and M. H. Devoret *Quantum Noise in Mesoscopic Physics* (ed. Nazarov, Yu. V.) 175-203 (Kluwer, 2003).

[60] D. Mozyrsky and I. Martin, Phys. Rev. Lett., **89**, 018301 (2002).

[61] M. P. Blencowe, J. Imbers, and A. D. Armour, New J. Phys.,**7**, 236 (2005).

[62] R. Deblock, E. Onac, L. Gurevich, and L. P. Kouwenhoven, Science **301**, 203-206 (2003).

[63] P. M. Billangeon, F. Pierre, H. Bouchiat, and R. Deblock, Phys. Rev. Lett **96**, 136804 (2006).

[64] S. Gustavsson, M. Studer, R. Leturcq, T. Ihn, K. Ensslin, D. C. Driscoll and A. C. Gossard Phys. Rev. Lett **99**, 206804 (2007).

[65] W. Lu, K. D. Maranowski, and A. J. Rimberg, Phys. Rev. B **65**, 060501 (2002).

[66] A. N. Korotkov, and M. A. Paalanen, Appl. Phys. Lett. **74**, 4052 (1999).

[67] A. Wallraff, D. I. Schuster, A. Blais, L. Frunzio, R. S. Huang, J. Majer, S. Kumar, S. M. Girvin and R. J. Schoelkopf. Nature, **431**, 162-167, (2004).

[68] L. Frunzio, A. Wallraff, D. I. Schuster, J. Majer and R. J. Schoelkopf. *IEEE Transactions on Applied Superconductivity,* **2**, 15, (2005).

[69] M. Göppl, A. Fragner, M. Baur, R. Bianchetti, S. Filipp, J. M. Fink, P. J. Leek, G. Puebla, L. Steen and A. Wallra J. Appl. Phys, **104** 113904, (2008).

[70] D. I. Schuster. *Circuit Quantum Electrodynamics.* Ph.D.thesis, Yale University, (2007).

[71] M. P. Blencowe's notes. *Model of cavity-JJ and cavity-SET system,* (2009).

[72] J. Aumentado, M. W. Keller, J. M. Martinis and M. H. Devoret, Phys. Rev. Lett., **92**, 066802 (2004).

[73] T. J. Gilheart, *Developing robust fabrication of Si/SiGe quantum dots with integrated RF-SET charge detectors.* Ph.D. Thesis, Dartmouth College, 2008.

[74] A. J. Ferguson, S. E. Andresen, R. Brenner and R. G. Clark, Phys. Rev. Lett., **97**, 086602 (2006).

[75] N. A. Court, A. J. Ferguson and R. G. Clark, Supercond. Sci. Technol. **21**, 015013 (2008).

[76] T. M. Eiles, J. M. Martinis, and M. H. Devoret, Phys. Rev. Lett., **70**, 1862 (1993).

[77] L. Roschier, P. Hakonen, K. Bladh, P. Delsing, K. W. Lehnert, L. Spietz and R. J. Schoelkopf, J. Appl. Phys. **95**, 1274-1286 (2004).

[78] A. Naik, O. Buu, M. D. Lahaye, A. D. Armour, A. A. Clerk, M. P. Blencowe and K. C. Schwab, Nature **443**, 193-196 (2006).

[79] M. Thalakulam, Ji. Z, and A. J. Rimberg, Phys. Rev. Lett., **93**, 066804 (2004).

[80] M. S. Choi, F. Plastina, and R. Fazio, Phys. Rev. Lett., **87**, 116601 (2001).

[81] A. Masssen van den Brink, Europhys. Lett., **58**, 562-568 (2002).

[82] M. Mück, J. B. Kycia, and J. Clarke, Appl. Phys. Lett., **78** 967-969 (2001).

[83] G. B. Lesovik and R. Loosen, JETP Lett. **65**, 295 (1997).

[84] U. Gavish, Y. Levinson, and Y. Imry, Phys. Rev. B **62**, R10637 (2000).

[85] S. D. Bennett and A. A. Clerk, Phys. Rev. B **74**, 201301(R) (2006).

[86] D. A. Rodrigues, J. Imbers, and A. D. Armour, Phys. Rev. Lett. **98**, 067204 (2007).

[87] O. Astafiev, K. Inomata, A. O. Niskanen, T. Yamamoto, Yu. A. Pashkin, Y. Nakamura and J. S. Tsai, Nature **449**, 588-590 (2007).